INAUGURAL - DISSERTATION

zur Erlangung der Doktorwürde der

Naturwissenschaftlich-Mathematischen

Gesamtfakultät der Ruprecht-Karls-Universität

Heidelberg

vorgelegt von:

Susanne Veronika Ott, M.Sc.

geboren in Erlangen

Tag der mündlichen Prüfung: 11.02.2019

Sintering properties of platinum nanoparticles on different oxide-based substrates

Gutachter:

Prof. Dr. Joachim P. Spatz

Physikalisch-Chemisches Institut
Ruprecht-Karls-Universität Heidelberg
Max-Planck-Institut für medizinische
Forschung, Stuttgart

Prof. Dr. Reiner Dahint

Physikalisch-Chemisches Institut
Ruprecht-Karls-Universität Heidelberg

Abstract

Metal nanoparticles play a significant role in exhaust combustion. They oxidize harmful products like carbon monoxide and hydrocarbons in order to prevent major environmental and health issues. In a converter, platinum nanoparticles (Pt NPs) are impregnated in a thin coating of a porous ceramic oxide. Due to their high surface-to-volume ratio, Pt NPs can provide high catalytic activities; however, elevated temperatures in the exhaust gas flow lead to thermal deactivation of the catalyst via sintering, thereby resulting in large losses in efficiency over the catalyst's lifetime.

In this thesis, the sintering behavior of 5-6 nm sized Pt NPs synthesized via block copolymer micellar nanolithography on various planar oxide-based substrates is investigated. First, their coarsening on both crystalline and amorphous silica (SiO_2) and alumina (Al_2O_3) is evaluated in regard to the mechanisms of Ostwald ripening and particle migration and coalescence. Sinter studies at 750°C in air reveal an enhanced thermal stability on the amorphous alumina-support Al_2O_3(a). Second, key influencing parameters on the sinter resistivity of the Pt NPs are identified. An increased NP adhesion on the amorphous substrates, a higher roughness and surface potential, as well as a larger contact angle of water on Al_2O_3(a) are all found to significantly contribute to enhanced sinter stability.

Furthermore, the thermal behavior of Pt NPs on dual-structured surfaces is examined at the interface between Al_2O_3(a) and SiO_2 to study the impact of compositional surface heterogeneities. The particles favor the high metal interaction Al_2O_3(a)-side over the low metal interaction SiO_2-side as shown by their diffusion away from the silica. Additionally, structural heterogeneities on sapphire wafers with varying tilt angles, and thus step edges of different height and size, contribute to a smaller increase in Pt NP diameter over time on the more tilted substrates when exposed to 1200°C under vacuum compared to NPs on less tilted substrates. Hereby, larger sintered particles are observed to preferably align along the step edges. This is due to a locally increased surface potential at the edges and because these edges function as Ehrlich-Schwoebel barriers. Thereby they hinder the diffusion of particles on the substrate. Lastly, the sinter stability of Pt NPs is successfully enhanced via the deposition of an isolating silica or alumina layer by sol-gel techniques. These films are shown not to cover the Pt NPs and also prevent the migration of platinum clusters toward each other during sinter studies at 750°C under atmospheric conditions.

Taken together, this data contributes to a better understanding of the thermal stability of Pt NPs catalysts with respect to the underlying support. The information gained from these sinter studies can be harnessed in the design of more thermally stable Pt NP catalysts, which can ultimately contribute to more environmentally sustainable technologies.

Kurzfassung

Metallische Nanopartikel spielen eine entscheidende Rolle in der Abgasnachbehandlung. Sie oxidieren für die Umwelt und die Gesundheit schädliche Substanzen, wie Kohlenstoffmonoxide und Kohlenwasserstoffe. In einem Fahrzeugkatalysator sind Platinnanopartikel (Pt NP) in eine dünne poröse Oxidkeramik imprägniert. Aufgrund ihres großen Oberfläche-zu-Volumen-Verhältnisses zeigen Pt NP eine hohe katalytische Aktivität. Allerdings verursachen hohe Temperaturen des Abgasstroms eine thermische Deaktivierung des Katalysators durch Sinterprozesse. Dieses führt mit der Zeit zu großen Effizienzverlusten.

In dieser Arbeit wird das Sinterverhalten von 5-6 nm großen Pt NP, die mit der Block-Copolymer Nanolithographie synthetisiert werden, auf verschiedenen planaren, oxid-basierten Substraten untersucht. Zuerst wird die Vergröberung der Partikel auf kristallinem und amorphem Siliziumdioxid (SiO_2) und Aluminiumoxid (Al_2O_3) in Bezug auf die Sintermodelle Ostwald-Reifung und Partikelmigration und Koaleszenz evaluiert. Sinterstudien an der Luft zeigen bei einer Temperatur von 750°C eine erhöhte thermische Stabilität der Nanopartikel auf amorphem Aluminiumoxid Al_2O_3(a). Anschließend werden maßgebliche Einflussfaktoren auf die Widerstandsfähigkeit der NP gegenüber dem Sintern ermittelt. Eine erhöhte Pt NP-Adhäsion auf den amorphen Substraten, eine ausgeprägtere Rauhigkeit, ein höheres Oberflächenpotential und ein vergrößerter Kontaktwinkel von Wasser auf Al_2O_3(a) tragen erheblich zur Sinterstabilität bei.

Darüber hinaus wird das thermische Verhalten der Pt NP auf strukturierten Oberflächen an der Grenzfläche von Al_2O_3(a) und amorphen SiO_2 untersucht, um den Einfluss der chemischen Oberflächenzusammensetzung zu erörtern. Dabei hat sich Al_2O_3(a) aufgrund einer höheren Wechselwirkung mit Metallen gegenüber dem SiO_2 durch die bevorzugte Diffusion der Pt NP von SiO_2 zu Al_2O_3(a) als überlegen gezeigt. Zusätzlich wird die Auswirkung struktureller Oberflächenheterogenität auf die NP-Stabilität anhand verkippter Saphir-Wafer aufgezeigt. Bei 1200°C im Vakuum ist die Größenzunahme der Partikel auf stärker gekippten Oberflächen kleiner, wobei die gesinterten Pt NP sich bevorzugt an den Stufenkanten anlagern. Dieses lässt sich auf ein lokal höheres Oberflächenpotential und auf eine Funktionsweise der Kanten als Ehrlich-Schwöbel Barrieren zurückführen, die eine Partikeldiffusion auf dem Substrat verlangsamen. Zuletzt wird die Sinterstabilität der Pt NP erfolgreich durch die Abscheidung einer isolierenden SiO_2- oder Al_2O_3-Schicht zwischen den Partikeln über das Sol-Gel-Verfahren erhöht. Diese Schichten bedecken die NP dabei nicht, verhindern aber gleichzeitig in Sinterexperimenten bei 750°C an der Luft die Migration von Platin-Clustern.

Anhand der Ergebnisse der durchgeführten Sinterstudien wird ein besseres Verständnis für die Erzeugung thermisch stabiler und hocheffizienter Pt NP-Katalysatoren bezüglich des darunter liegenden Substrats gewonnen. Somit leistet diese Arbeit einen wichtigen Beitrag zur Entwicklung umweltverträglicher Technologien.

Danksagung

Am Ende meiner Promotion möchte ich die Gelegenheit nutzen und den Menschen einen besonderen Dank aussprechen, die mich während dieser Zeit begleitet und zum Gelingen dieser Doktorarbeit beigetragen haben.

In erster Linie gilt mein Dank Prof. Joachim P. Spatz für die fachliche und persönliche Betreuung meiner Arbeit, sowie für die entgegengebrachte Offenheit und Unterstützung bei der Auswahl eines geeigneten Themas. Das von ihm entgegengebrachte Vertrauen schätze ich sehr. Darüber hinaus möchte ich mich herzlich für die Freiheit bei der Ausgestaltung des Forschungsthemas und die dabei zur Verfügung stehenden Möglichkeiten bedanken.

Ebenso möchte ich Herrn Prof. Reiner Dahint für die Zusage als Zweitgutachter und der damit verbundenen Arbeit und Mühe danken.

Außerdem danke ich Dr. Gunther Richter als Leiter der ZWE Materialien am MPI IS für die stets offene Tür bei fachlichen Diskussionen und die große Hilfsbereitschaft bei den Dünnschichtherstellungen, durchgeführt von Reinhart Völker und Frank Thiele. Für alle weitere technische Unterstützung möchte ich mich bei folgenden Personen bedanken: Maria Sycha für die sorgfältige Präparation der TEM-Querschnittsproben, Ioanis Grigoridis für die Hilfe am SEM, Marion Kelsch vom StEM unter der Leitung von Prof. Peter A. van Aken für die Betreuung am TEM, Michaela Wieland aus der Forschungsgruppe von Prof. Eric J. Mittemeijer für das Engagement bei meinen XPS-Proben, wie auch Arnold Weible und Thomas Meisner für Rat und Tat bei den Ofenexperimenten.

Darüber hinaus bedanke ich mich sehr herzlich bei meinen Kollegen des IMW3-Lehrstuhls unter der Gruppenleitung von Prof. Joachim Bill, die mich bei fachlichen Fragestellungen bezüglich des AFM und bei der nasschemischen Siliziumdioxid- und Aluminiumoxidschichtsynthese ausdauernd und geduldig unterstützt haben: Stefan Kilper, M.Sc. und Dipl.-Ing. Mirjam Eisele.

Großer Dank gilt auch meiner Vorgängerin und ehemaligen Kollegin Dr. Sarah Jahn für die gute Einarbeitung in das Thema und für die immerwährende Bereitschaft, auch darüber hinaus experimentelle Probleme zu besprechen. Weiterhin danke ich meiner Masterpraktikantin Sarah Young und meinem Masterarbeitsstudenten Tingyu Zhang, die mir engagiert bei den experimentellen Arbeiten geholfen haben.

Ferner möchte ich mich bei unseren Partnern der BASF SE bedanken, die durch das gemeinsame Kooperationsprojekt den Grundstein für diese Arbeit legten. Bei Dr. Michael Bender, Dr. Michael Rieger, Dr. Wolfgang Rüttinger und Dr. Ansgar Schäfer bedanke ich mich für die vertrauensvolle und motivierende Zusammenarbeit und für viele fachliche Diskussionen.

Einen herzlichen Dank schulde ich ebenfalls allen Kollegen für Anregungen, Korrekturen und für gute Gespräche fernab des Arbeitsalltags: Stefan, Cora, Mirjam, Rahel, Achim, Tim, Lucia,

Heidi, Johannes, Jennifer, Andrew, Barbara, Sebastian, Kerstin und die weiteren Mitarbeiter der Arbeitsgruppe Spatz.

Außerdem möchte ich mich bei meiner Mutter Annette, meinen Brüdern Matthias und Johannes, allen Verwandten und Freunden außerhalb des Institutes bedanken, die mir einen starken Rückhalt gegeben haben und immer für mich da waren. Zum Schluss danke ich von ganzem Herzen meinem Ehemann Markus, der mich stets ermutigt und in erfolgreichen, sowie stressigen Zeiten treu begleitet hat.

Contents

1 Introduction

Over the past 40 years, metal nanoparticles (NPs) with lateral dimension of less than 100 nm have been utilized in a wide variety of scientific applications [58, 94, 69, 167]. Due to their small sizes and high number of surface atoms, the surface area-to-volume ratio is large and thus, their physical-chemical properties can differ significantly from their bulk material [58, 114]. One such property is the reduction of the melting points, first studied and reported for tin by Takagi and Wronski in 1954 and 1967 [140, 160]. Other affected characteristics include changes in electrical conductivity, magnetic permeability and fluorescence, partly caused by quantum effects occuring at the nanometer-scale [10]. Additionally, a high chemical reactivity due to the large surface area, and therefore numerous catalytically active sites, makes NPs great candidates for catalytic applications [58]. Ever since the degradation of hydrogen peroxide via platinum nanoparticles (Pt NP) in the 19th century [7], NPs have gained tremendous importance in heterogenous catalysis and are now utilized in 90 % of all chemical processes worldwide [41, 123]. Noble metal nanoparticle catalysts are able to transform harmful products into less toxic ones. Thereby they ensure to meet stricter environmental regulations, while also lowering health risks despite an increasing world population [41, 96]. Pt NPs can make chemical conversion highly selective in many hydrogenation and dehydrogenation reactions, as well as in alkylation and selective oxidation reactions [123, 2]. These include, for example, the hydrogenolysis of ethane [113], ethylene [112] and propene [166]. Pt NPs specifically oxidize carbon monoxide (CO) and hydrocarbons (HC) during exhaust combustion, thus playing a major role in the reduction of emissions [27]. For applications in car converters, they are impregnated into substrates consisting of a thin coating ("washcoat") of a porous ceramic oxide, commonly alumina (Al_2O_3) or silica (SiO_2) on a ceramic monolith [20, 56, 28], see Figure 1.1. Supplementary noble metal NPs, e. g. rhodium, help to reduce nitrogen oxide (NO_x) [20].

Enhanced catalytic activities and selectivities depend on size, shape and composition of the metal NPs [75]. Based on the efficiency with which adsorbates and intermediate reactants bind to the NPs, their size can have different effects on the reaction rates. For some processes, smaller NPs show higher reaction rates, while the opposite is true in other cases. Additionally, some NPs reveal a specific size range in which they facilitate the best activity for catalytic processes [42]. While more research has been conducted on the size-dependency than on the shape-dependency of the catalytic activity [96], one study by Narayanan *et al.* shows that tetrahedral Pt NPs with a larger amount of surface atoms at corners and edges are significantly more active compared to cubic ones [99]. Lastly, the role of the support on the catalytic performance of NPs has been investigated. "Strong metal-support interactions" (SMSI) between the noble metal NPs and the substrate can improve their catalytic reactivity [171]. First reported on titania [142, 141], Pt NPs also exhibit advantageously altered properties on other oxides, such as magnetite [109] and

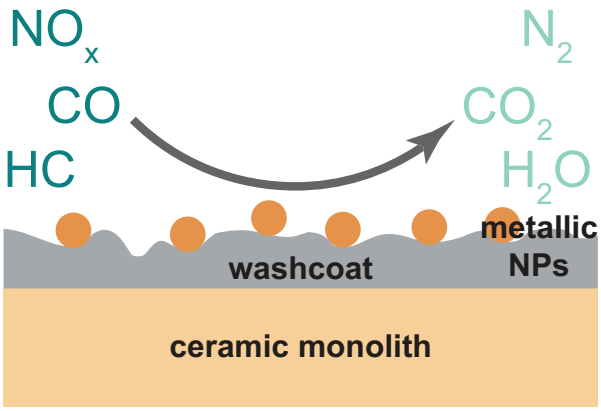

Figure 1.1: Schematic illustration of impregnated metallic NPs (e.g. Pt and Rh) on a porous ceramic oxide washcoat for the catalyzation of harmful emission gases (CO, HC, and NOx).

ceria [30]. Here, the support can transfer charges to or from the particles and provide additional reaction sites. This was demonstrated by Fukuoka *et al.* on Pt NPs in mesoporous silica during the oxidation of CO [54]. Additionally, the support can stabilize NPs, but it can also encapsulate NPs at higher temperatures or cause structural and/ or shape-related changes, as summarized in a review by Cuenya *et al.*. Hence, the influence of the underlying support cannot be ignored [41].

While aiming for a high catalytic activity and selectivity, long-term stability is one of the most important criteria for an effective and functional catalyst [2, 97]. Catalyst deactivation, defined as the loss of catalytic activity and selectivity over time, is a major and very costly industrial challenge [16]. Different mechanisms can lead to catalyst failure. Reactants or impurities can be strongly adsorbed on the surface of the catalyst and thus block the active sites. Sulphur, as one example, can poison Pt-based catalysts. During fouling, the surface of the catalyst is physically covered by deposited species, which again hinders the catalytic reaction at the barred active sites. Also, other chemical reactions occuring with the molecules in the gas phase or the substrate can diminish the desired activity. Furthermore, mechanical failure originates from crushing when the catalyst or its support experience thermal expansion and compression or it can be caused by attrition processes. During this process, the catalytic material is lost and the substrate onto which the catalyst is impregnated is destroyed [16, 97]. Lastly, elevated temperatures exceeding 1000°C can lead to thermal deactivation of the catalyst, which is especially a problem within car exhaust systems [28, 65]. Approximately 10 % of the initial Pt NPs are emitted from a car converter, either thermally or mechanically induced, which can then lead to toxicologial problems [143, 41].

Sintering as a thermal degradation process is defined as the decline of the catalytically active surface area due to the thermodynamically favorable growth of the NPs [97, 16, 33]. Two models have been proposed to describe the coarsening of NPs through an increase in average particle size and a broadening of the particle size distribution (PSD): (1) larger NPs grow at the expense of smaller ones through the diffusion of small adatoms towards the larger particles triggered by a chemical potential difference, a process referred to as Ostwald Ripening (OR); (2) NPs migrate on the surface and coalesce upon meeting, a phenomenon termed particle migration and coalescence (PMC) [65, 44].

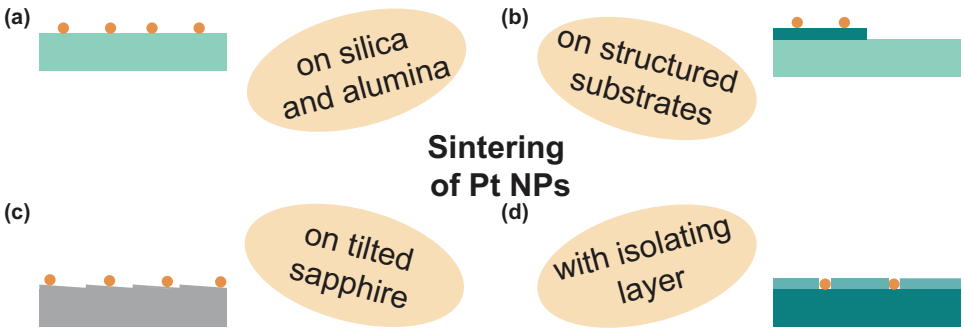

Figure 1.2: In this PhD thesis, the sintering behavior of Pt NPs was studied (a) on crystalline and amorphous silica and alumina with the evaluation of its contributing surface properties, (b) on dual-structured silica and alumina substrates, (c) on tilted sapphire wafers, and (d) with an isolating silica or alumina layer.

Pt NP sintering has been studied on various substrates under diverse conditions. Model systems with lower complexity help to analyze and characterize the influence of individual parameters including the particle size or elemental composition on the thermal stability of the Pt NPs. Also, their coarsening behavior on individual substrates has been studied. Although the commonly used oxide materials alumina and silica have been compared with each other regarding their suitability as Pt NP catalyst substrates [169], neither their physical or chemical parameters nor the impact of these on the sintering behavior of Pt NPs have been examined experimentally. Thus, the focus of this PhD thesis is to explore crystalline and amorphous silica and alumina as possible supports during sinter studies at 750°C under atmospheric conditions (Figure 1.2a). Additionally, the contribution of NP adhesion, substrate roughness, surface potential and energy are analyzed as key influencing parameters on NP sintering. Furthermore, the Pt NPs are tested on structured surfaces composed of two materials, amorphous alumina and silica (Figure 1.2b), as well as on tilted crystalline sapphire wafers with step edges of varying height and size (Figure 1.2c). During sinter studies in air at 750°C or under vacuum at 1200°C, the influence of compositional and structural heterogeneities on the coarsening behavior of Pt NPs is revealed. Lastly, an increased sinter stability of Pt NPs is successfully achieved through the deposition of an isolating silica or alumina layer between the particles by simple sol-gel techniques in order to prevent the particles from migrating towards each other (Figure 1.2d).

Identifying key factors of the common industrially used silica and alumina substrates on metal NP sinter resistivity, these sinter studies lay the foundation for an improved design of highly efficient and stable catalysts. Thus, the amount of costly and harmful Pt NPs in exhaust combustion systems can be reduced while maintaining a high activity to fulfil upcoming strict regulations on exhaust standards.

2 Fundamentals of techniques

In this chapter, first the theoretical background for the synthesis of Pt NPs via block copolymer micellar lithography will be introduced. Following, the principles of the used characterization methods including scanning electron microscopy, transmission electron microscopy, atomic force microscopy, lateral force microscopy and Kelvin probe force microscopy, as well as contact angle measurements, ellipsometry, and dynamic light scattering are presented. In the last part, the materials and methods for the experiments are listed.

2.1 Synthesis of platinum nanoparticles

Monodispersed NPs of uniform sizes can be synthesized via block copolymer micellar nanolithography (BCML) as a "bottom-up" technique. Generally, "bottom-up" procedures involve molecular or atomic components that assemble and form more complex and larger-sized structures [23]. In contrast, methods like lithography are used for "top-down" approaches, in which nanostructures are fabricated by starting from materials with large dimensions and breaking them down to the sub-µm-level [23]. BCML offers strict control of NP size and interparticle distance, and is based on the utilization of diblock copolymers [132, 131]. Block copolymers contain different polymer blocks that are commonly immiscible followed by microphase separation [59]. Dominated by long-ranging repulsive and short-ranging attractive forces, the copolymers self-assemble to ordered structures. Depending on the type and length of the polymer segments in the block copolymer, spheres, cylinders, lamellae and other complicated structures are formed. The Flory-Huggins interaction parameter and the degree of polymerization determine the most stable structural confirmation with the lowest energy [52]. For the BCML-synthesis of Pt NPs, diblock copolymers consisting of one hydrophobic segment of polystyrene (PS) (Figure 2.1a) and one hydrophilic segment of poly-2-vinylpyridine (P2VP) (Figure 2.1b) were chosen.

Balancing repulsive forces due to incompatibility in hydrophilicity and short-ranging attractive covalent bonds between the two polymer parts, micelles are formed in the presence of a selective

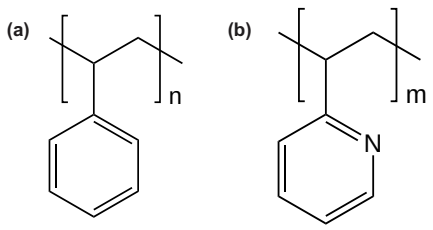

Figure 2.1: Chemical structures of block copolymer segments used for BCML of Pt NPs: (a) polystyrene (PS) and (b) poly-2-vinylpyrridine (P2VP).

solvent [52, 57]. The more soluble segment then forms a corona around the insoluble inner block [59]. Controlled by the molecular weight of the block copolymers and the interactions of the polymer blocks among each other, as well as with the solvent, the diameter of the micelles can be adjusted [57]. Yet, a certain critical micelle concentration (CMC) has to be reached in order for the first micelles to assemble, while the concentration of single chains in solution remains constant [84, 59, 133]. As illustrated in Figure 2.2a, micelles with a core of the less soluble P2VP polymer segment and an outer shell of soluble PS are formed while being stirred in toluene [84]. In these nanoreactors, metal precursor salt is selectively dissolved into each micelle. This then changes the thermodynamic properties of the solution and the kinetic stability of the micelles. Newly formed ionic bonds between the metal precursor and the P2VP segment lower the CMC and stabilize the micellar aggregates [84, 93]. By varying the concentration of metal salt and thus the loading of the micelles, the size of the nanoparticles can be controlled [57, 84]. The resulting micellar solution can either be dip or spin coated onto the substrates [84]. During the spin coating process a thin film is deposited onto a flat, rigid surface by centrifugal draining and evaporation of the solvent [134, 121]. In the first step the micelle solution is added onto the substrate, which is then accelerated until a desired rotational velocity is reached. Due to centrifugal forces, the solution spreads on the substrate and surplus is lost at the edge. Simultaneously thinning of the micellar film occurs until an equilibrium thickness is achieved. This is either caused by pressure effects or by an increased viscosity due to evaporation of the solvent in a following step [62, 121]. Since spin coating is a very easy, fast and versatile technique, it was the method of choice in this work (Figure 2.2b). A dense film of micelles can be achieved with long-range van der Waals interactions acting on the micelles during solvent evaporation [128]. This leads to a quasi-hexagonal pattern of micelles as a result of attractive capillary forces and opposite repulsive steric and electrostatic interactions [84]. Through choosing different polymer weights of the diblock copolymers, the spacing between the NPs can be regulated [57]. By applying a hydrogen / argon-plasma the polymer is removed and the metal salt is reduced, resulting in quasi-hexagonally arranged platinum nanoparticles (Figure 2.2b and c).

Besides platinum nanoparticles, gold, silver, and palladium NPs have been reported to be synthesized via BCML with diameters ranging from 1 to 15 nm and an interparticle spacing of 25 to 250 nm [85]. Additionally, bimetallic NPs can be formed by this technique through the separate addition of two metal precursor salts [129]. Many different flat materials can serve as substrates upon resistance to the solvent and the plasma exposure. This includes silicon, gold, glass, sapphire, titania, mica, and gallium arsenide [130, 57, 84]. Recently, 3D-substrates, like µm-sized glass spheres, have been immobilized with BCML-synthesized NPs [55]. One of the novel aspects of the BCML technique is the regular arrangement of the NPs on the substrates. Furthermore, the particles are free to contribute to chemical and physical interactions and are very stable without organic coatings supporting or stabilizing them [130].

2.2 Characterization methods

Due to the Pt NPs' small size, characterization techniques of high magnification and superior sensitivity are needed to obtain high-quality information on their size, shape, morphology

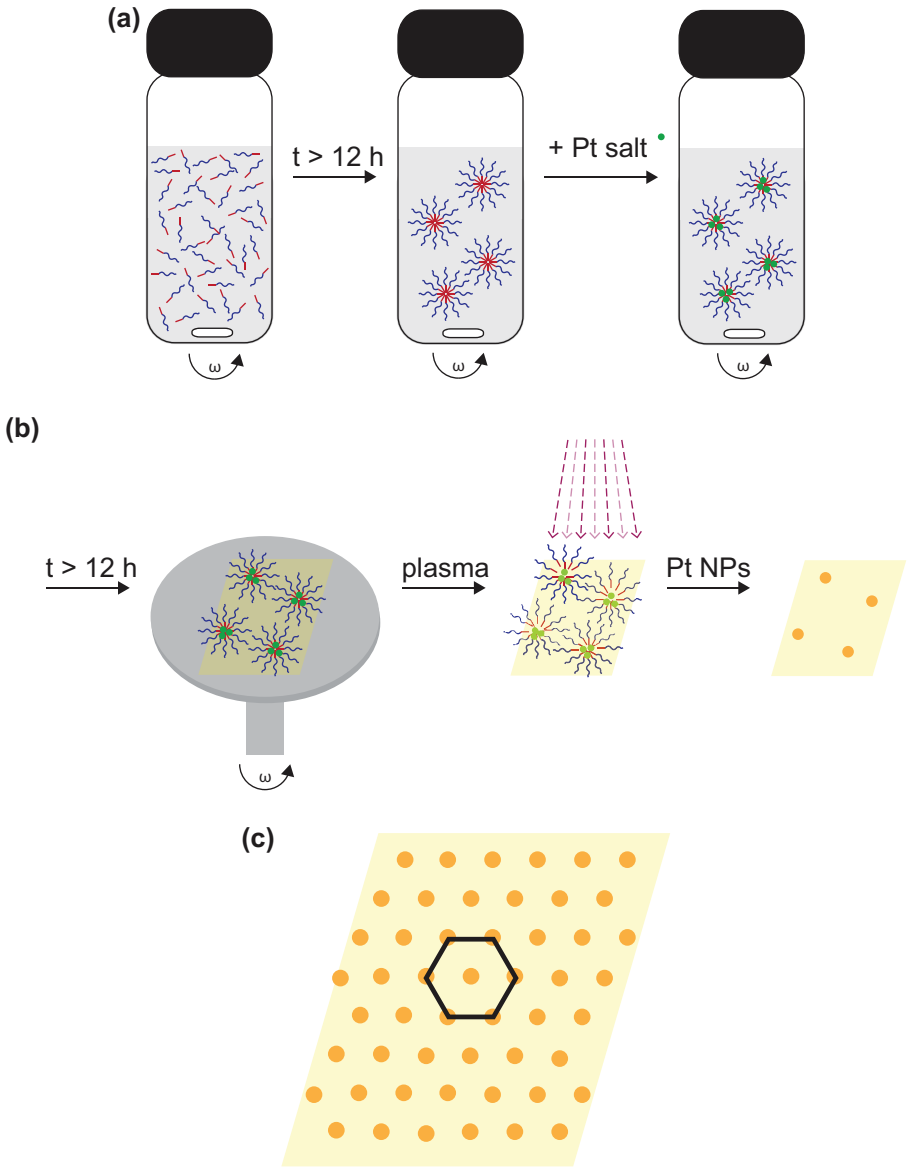

Figure 2.2: Scheme illustrating the synthesis of Pt NPs via BCML: (a) the block copolymer PS-b-P2VP is dissolved in toluene and forms micelles. Afterwards, platinum precursor salt is added to the polymer solution and exclusively dissolved in the micelles. (b) The loaded micelles are then spin coated unto the desired substrates. Finally, the polymer matrix is removed during an hydrogen / argon-plasma and the metal salt is reduced, yielding (c) quasi-hexagonally arranged Pt NPs.

and structure [110]. In this thesis, transmission electron microscopy and scanning electron microscopy (SEM) were used for imaging, while the height of the Pt NPs for particle size distributions (PSDs) during sinter studies was obtained by atomic force microscopy (AFM). Additionally, information regarding the roughness of the supports was gained by tapping mode-AFM. NP adhesion could be monitored with the lateral force microscopy mode at the AFM and Kelvin probe force microscopy using AFM was performed to determine the surface potentials of the substrates. Lastly, contact angle measurements revealed disclosure of the surface tension of water on the different supports. With the help of energy dispersive X-ray spectroscopy at the SEM and X-ray photoelectron spectroscopy the samples were analyzed with respect to their elemental and chemical composition. For the isolation of Pt NPs with different layers, the layer-solution was characterized with dynamic light scattering regarding its particle sizes and the layer thickness was determined by ellipsometry.

2.2.1 Transmission electron microscopy

In general, electron microscopes generate magnified pictures with atomic resolution by using an electron beam and focusing it via electrostatic or electromagnetic lenses under high vacuum conditions. The advantage of a beam consisting of electrons is their short de-Broglie-wavelength which is approximately more than 12 orders of magnitude smaller compared to light [156]. In a transmission electron microscope (TEM), a resolution of less than 1 nm can be reached and so images on the atomic scale are achievable [110, 155].

When exposing a sample to fast-moving electrons, a variety of interactions with the sample can occur and these different phenomena can be exploited to obtain information about it (Figure 2.3). In the case of TEM, a very thin and conductive sample is penetrated by an electron beam. This incident beam interacts with the sample and its electrons are scattered at the crystal lattices of the investigated material. These electrons are detected and an image is derived [1, 155]. Evaluating the contrast between the sample and the background, morphological and structural information about the sample are obtained [110]. Commonly, different lenses are necessary to create the picture. Condensor lenses direct the electron beam from the electron source in a parallel alignment before it is spread by the sample. Subsequently, objective lenses, intermediate lenses and projector lenses help to acquire the final image. The latter two lenses are responsible for achieving the desired magnification while also compensating each others' lense defects [156, 1]. Spherical aberrations are caused by defects in all of the above mentioned electron lenses which transform points to disks. Also chromatic aberrations can occur when the electron beam is not monoenergetic and thus, they induce a loss of image quality. Furthermore, astigmatism triggered by an electron beam, that is not in perfect symmetric alignment to the lense axis, and distortions often induced by operating lenses at non-ideal focal lengths can diminish the high-resolution in the picture [156]. Depending on the choice of either detecting the transmitted or diffracted beam, a bright or dark field image with a respective bright background and dark sample structure in the first case and vice versa in the dark field mode can be reconstructed [1].

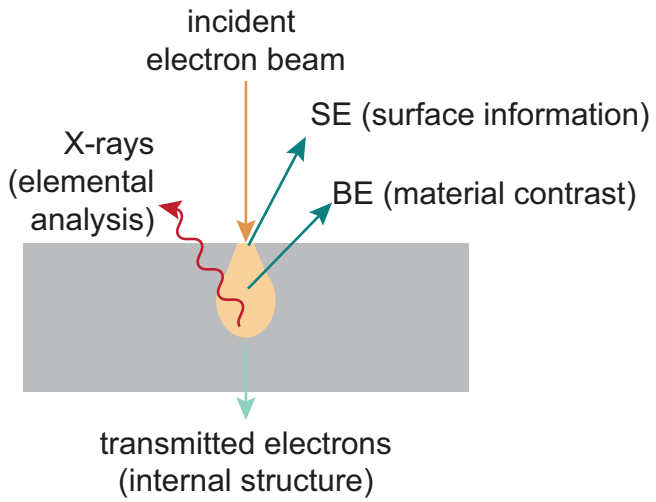

Figure 2.3: Schematic illustration of electron beam interactions with the sample. The incident electron beam causes X-rays, transmitted, secondary (SE) and / or backscattered (BE) electrons to be released from the sample, each of which provides different information.

2.2.2 Scanning electron microscopy

Unlike TEM, in a scanning electron microscope (SEM) the electrons do not penetrate the thick conductive sample, but interact with the surface and are scattered back. Here, the electron beam is scanned across the substrate and the differently scattered electrons are detected [110]. Since the spot size of the electron beam and hence the interaction volume of the electrons with the atoms in the substrate are bigger than atomic distances, the resolution of a SEM is in the lower nanometer range and thus not as good as with the TEM. However, larger areas and the surfaces of bulk materials can be scanned with less time needed and easier sample preparation [110]. Therefore, the SEM is the most widely used electron beam instrument [1].

A focused electron beam is scanned across the substrate and an image with very good spatial resolution, and thus a three-dimensional impression, is received. When the electrons hit the sample surface, depending on their energy, a variety of interactions can occur with the atoms of the substrate. These then cause the formation of secondary products (Figure 2.3). They can be utilized for different imaging modes and analytical techniques. The collisions of the electron beam with the atoms are either elastic when the electron is deflected without the hand-off of energy towards the specimen or inelastic when energy for another process is transferred from the electron to the atom and a different electron or X-rays are emitted. The most commonly used type of deflected electrons for imaging are the secondary and backscattered electrons (Figure 2.3) [156]. Secondary electrons (SE) with low kinetic energy are the result of inelastic scattering processes in which the outermost electrons are released from the substrate surface into the vacuum leaving an ionized atom behind. Yet, only secondary electrons very close to the spot where the incident electron beam hits the sample are obtained and used for surface reconstruction in the Inlens mode [156, 34]. On the contrary, backscattered electrons (BE) contain higher energies and are caused by elastic scattering deeper within the sample and so contain in-depth information. Since the backscatter coefficient correlates with the atomic number, conclusions about the type of the material can be drawn [34]. Recording both secondary and backscattered electrons yields images

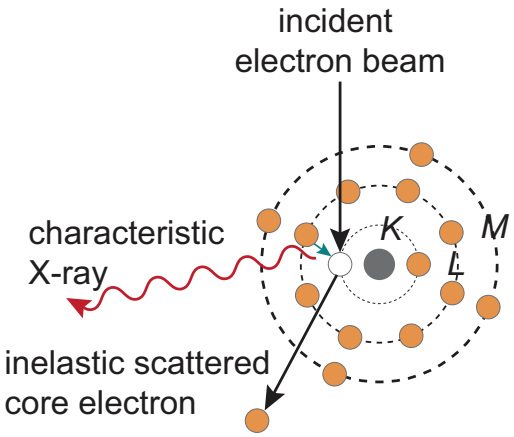

Figure 2.4: Scheme illustrating the principle of EDX: By inelastic scattering of the incident electron beam with an inner-shell electron, the latter one is released from the sample. Thus, an electron from an outer-shell fills the vacancy triggering a characteristic X-ray which can be analyzed qualitatively and quantitatively.

in the SE2-mode and combines high topographical contrast with detailed surface structures. However, material contrast on the nanometer-scale can only be detected with the energy selective backscattered (ESB)-mode that exclusively uses backscattered electrons to create the image [34].

Similar to TEM, electromagnetic condensor and objective lenses focus the electron beam coming from a gun. Afterwards, scan coils guide the beam on the specimen in a scan pattern. If secondary or backscattered electrons are generated, they are amplified upon reaching the specific detector and translated to a final picture [1].

Additionally, energy dispersive X-ray spectroscopy (EDX) at the SEM can be used for analytical characterization of the sample surface. As shown in Figure 2.3 incident electrons can also induce the emission of X-rays. Through inelastic scattering with an inner-shell electron, energy is transferred and this electron leaves its orbital. The generated hole is then filled by another electron from an outer energy level shell triggering a characteristic X-ray with the energy between the outer and the inner orbital (Figure 2.4). Depending on if the electron leaves the L or M shell and falls down onto the core one K, the emitted radiation is termed K_α in the first and K_β in the second case [124, 156]. Since the specific energy of the characteristic X-ray wavelength correlates with each individual element, qualitative identification and quantitative analysis through the peak energy and the integrated peak intensity respectively can be achieved. Yet, EDX is more sensitive to heavy elements due to an increased emission probability [124].

2.2.3 Atomic force microscopy

Atomic force microscopy (AFM) is a versatile technique that provides information of the surface structure with high resolution and good accuracy on the sub-nanometer scale, as well as on microstructural properties. Unlike in electron microscopes, all samples, independent of their conductivity, can be measured and imaged under atmospheric conditions, in vacuum or in liquid. In an AFM a sharp and solid probe is applied onto these samples and scanned over its surface, resulting in a map of its height information [47, 25]. When the tip is brought in close contact

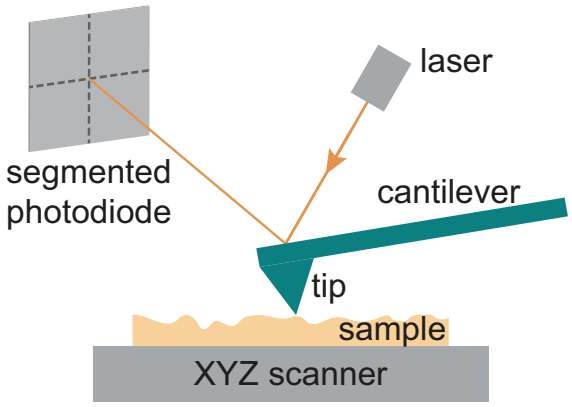

Figure 2.5: Scheme illustrating the principle of AFM. A tip mounted on a cantilever is deflected by forces acting between the sample's surface and the tip when scanned over the sample. This is monitored by a laser pointed to the cantilever and its reflection is detected by a four-segmented photodiode.

with the sample, interactions between these two materials take place. On one hand long-range attractive forces including Coulombic electrostatic forces or van der Waals interactions, compete with short-range repulsive forces when atomic inner electron shells overlap [25]. These interactions then lead to the deflection of the tip mounted on a cantilever, which is monitored through a laser pointed to the head of the cantilever and its reflection is detected by a four-segmented photodiode (Figure 2.5).

Piezoelectric scanners move the tip or sample in the x- and y-axes to map the scanning area by translating an electrical potential into a mechanical movement of the tip or sample. The probe can then detect forces on the piconewton-scale, which are amplified and projected as an image [47]. At the AFM, images of a combination of the sample topography and the tip geometry can be received in three different main modes. These can be divided into ones which obtain the static deflection of the cantilever or ones which analyze its dynamic oscillation. For contact mode, the tip is scanned across the sample while being permanently in contact with it. In this mode, strong short-range repulsive forces act on the cantilever and this leads to a high resolution of these images. Meanwhile, a feedback control evaluates the measured deflection of the cantilever to maintain either a constant total force on the sample or a constant distance between the tip and the sample. When the tip is removed from the surface during the measurement, the attractive forces gain importance and oscillating cantilevers are used for non-contact scan modes with the advantage of preventing sample damage. Changes in oscillation amplitude or frequency caused by the interacting forces between tip and sample lead to a difference in cantilever resonance frequency and can be detected. Lastly in tapping scan mode, the oscillating tip is scanned across the sample while touching it during each oscillation cycle. In this case, attractive and repulsive forces are measured and registered allowing the elimination of lateral forces while perceiving information about surface properties as well [47, 25].

Lateral force microscopy

In addition to topographical information, the AFM can be used to gain information regarding the surface friction characteristics of the sample or to study the adhesion of nanoparticles on the substrates. One of the scan modes is the lateral force microscopy (LFM) which measures the mechanical interaction of the tip in contact mode by detecting the lateral twisting of the cantilever. This torsion is caused by the friction occuring on the tip as it scans across the sample. By using a cantilever which is more resistant to lateral bending compared to bending in the normal direction, the signal can be split up in height or shape and friction information [47, 119]. Upon calibration of the sensitivity or stiffness and spring constant of each individual cantilever this technique allows the quantification of differences in sample properties. First, the deflection sensitivity α can be obtained by recording force-distance curves when engaging the cantilever towards the sample surface and then retracting it. Afterwards, the spring constant k_{LFM} can be determined by measuring the mechanical response of the cantilever to thermal noise [122]. With these values and the experimentally obtained deflection of the cantilever V, the force F between the tip and the sample can be calculated relying on Hooke's law [64]

$$F = k_{LFM} \cdot \alpha \cdot V. \tag{2.1}$$

In this thesis, NP adhesion on different substrates is measured by applying LFM-scans to determine the force F necessary in order to remove the NPs from the samples.

Kelvin probe force microscopy

With the help of AFM-based Kelvin probe force microscopy (KPFM) surface potential maps can be recorded. When calibrating the tip with reference samples of known work function, for example chromium or nickel, an absolute value of the work function for metals and semiconductors can be determined [47]. First introduced in 1991, KPFM is useful for measuring the contact potential difference (CPD) between a tip and a sample [102]. Used in dual-pass mode, the topography is recorded in a first scan and in a second non-contact scan the electric field changes are analyzed [78]. In this latter scan, the tip and sample with different Fermi levels form a capacitor (Figure 2.6a). Upon electrical contact between the tip and the sample, their Fermi levels align through the flow of electrons until an equilibrium is reached (Figure 2.6b). Thus, the tip and the sample are charged, which leads to the formation of the CPD and results in the creation of a surface dependent electric field. To sense this electric field, an AC bias is additionally applied to the cantilever. Triggered by electrostatic interactions with the existing electric field between the tip and the surface, the cantilever is deflected and oscillates. Changes in the oscillation amplitude or frequency are quantified directly via amplitude modulation KPFM (AM-KPFM) (Figure 2.7a) or frequency modulation KPFM (FM-KPFM) (Figure 2.7b). Using a feedback loop of the AFM-system, a DC bias voltage is applied to compensate the CPD so that the electric force does not act on the cantilever any longer, which returns to its original position (Figure 2.6c). As a result, the applied DC bias voltage directly corresponds to the CPD (V_{CPD}) [78, 170], which is defined as

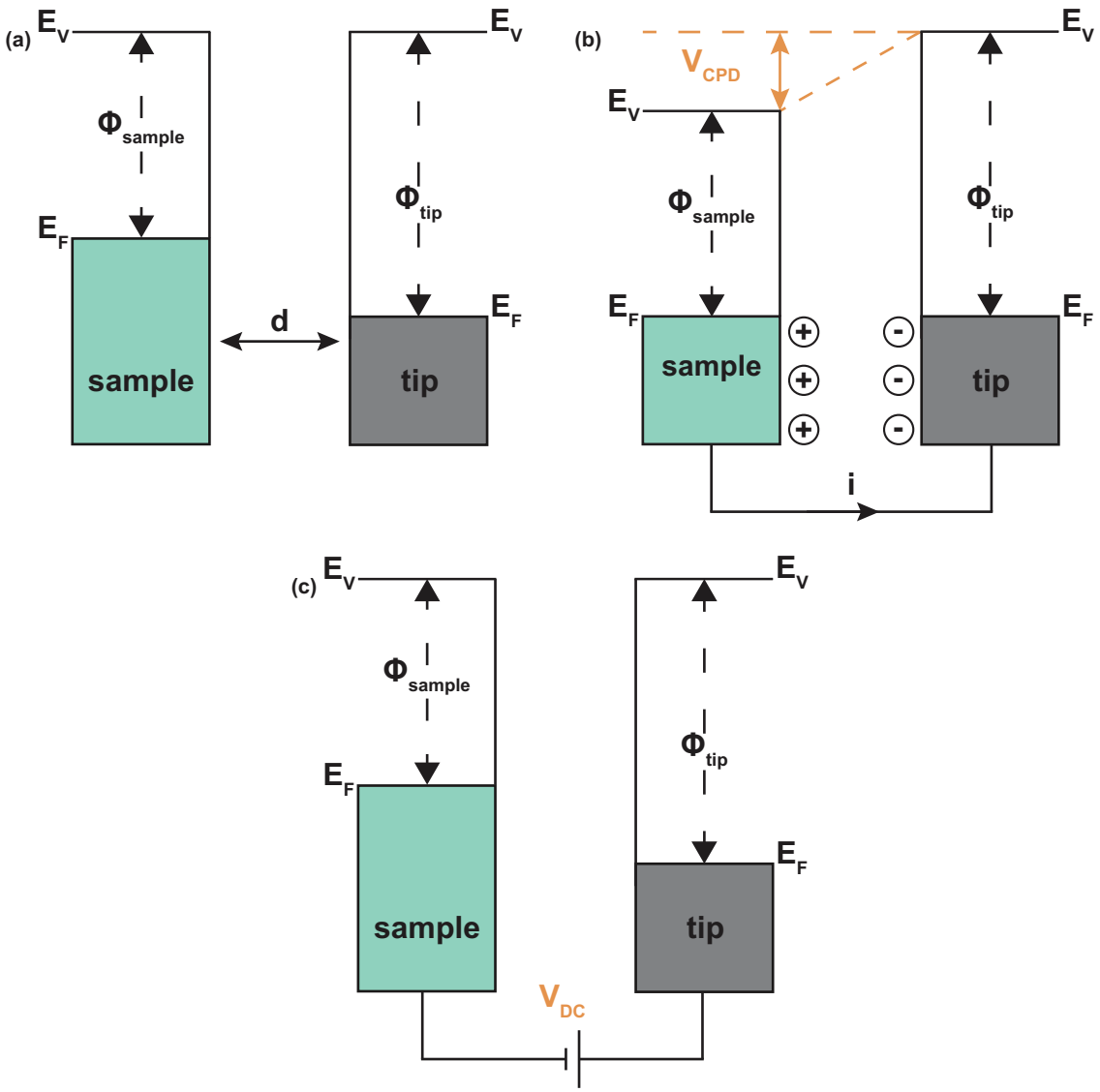

Figure 2.6: Energy and charge diagrams illustrating KPFM technique: (a) Tip and sample with different Fermi levels (E_F in regard to the vacuum level E_V) form a capacitor. (b) Upon electrical contact between the tip and the sample, their Fermi levels align through the flow of electrons until an equilibrium is reached, leaving the tip and the sample charged. (c) A DC bias voltage is then applied to compensate the occuring CPD (V_{DC}) [92].

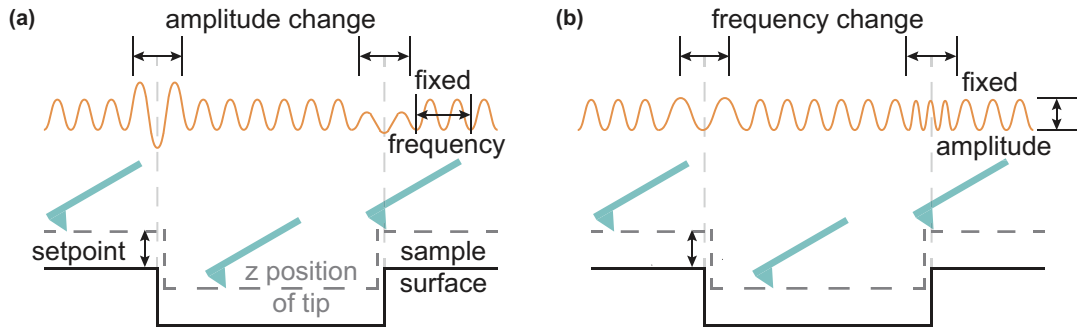

Figure 2.7: Schematic illustration of KPFM operation with (a) amplitude modulation (AM) versus (b) frequency modulation (FM) mode [92].

$$V_{CPD} = \frac{\Phi_{tip} - \Phi_{sample}}{-e} \tag{2.2}$$

with the work functions of tip Φ_{tip} or sample Φ_{sample} and the elementary charge e [92].

The electrostatic force F_{el} between the tip and the sample, which form the capacitor with distance z and capacitance C is

$$F_{el} = -\frac{1}{2}\frac{\delta C}{\delta z}(\Delta V)^2. \tag{2.3}$$

ΔV as the potential difference includes the intrinsic CPD (V_{CPD}), the externally applied DC voltage (V_{DC}) and an AC voltage (V_{AC})

$$\Delta V = V_{DC} \pm V_{CPD} + V_{AC} \cdot \sin(\omega t). \tag{2.4}$$

In AM-KPFM the electric force is measured due to the modulation of the AC bias at the frequencies ω in the second term and 2ω in the third term, which can be seen when substituting equation 2.4 in 2.3

$$F_{el} = \frac{\delta C}{\delta z}((V_{DC} \pm V_{CPD})^2 + \frac{1}{2}V_{AC}^2) + \frac{\delta C}{\delta z}(V_{DC} \pm V_{CPD})V_{AC} \cdot \sin(wt) + \frac{1}{4}\frac{\delta C}{\delta z}V_{AC}^2 \cdot \cos(2wt). \tag{2.5}$$

Then, the oscillation amplitude at ω is nullified when $V_{DC} = V_{CPD}$ [92, 39].

However, in FM-KPFM the electric force gradient is detected

$$F_{el}^{'} = \frac{\delta F_{el}}{\delta z}. \tag{2.6}$$

Thus, when $V_{DC} = V_{CPD}$ applies, the electric force gradient is nullified and the surface potential is obtained

$$F_{el}^{'} = \frac{\delta^2 C}{\delta z^2}((V_{DC} \pm V_{CPD})^2 + \frac{1}{2}V_{AC}^2) + \frac{\delta^2 C}{\delta z^2}(V_{DC} \pm V_{CPD})V_{AC} \cdot \sin(wt) + \frac{1}{4}\frac{\delta^2 C}{\delta z^2}V_{AC}^2 \cdot \cos(2wt). \tag{2.7}$$

Here, the electric force gradient is detected by monitoring the change in effective spring constant of the cantilever, which correlates to its resonance frequency [92, 39]. The latter method is more complex, yet has the advantage of higher lateral resolution because the force gradient is more sensitively measured by the small tip than by the whole cantilever as with AM-KPFM [170].

2.2.4 Contact angle measurements

Contact angle measurements can reveal information about surface properties of solid substrates. In the case of the simple and most commonly used sessile drop method, a liquid drop is placed

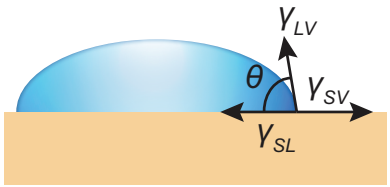

Figure 2.8: Scheme illustrating principle of sessile-drop contact angle measurement: The contact angle θ is obtained by manually placing a tangent to the side of the drop. The surface tension between liquid and vapor γ_{LV}, the interfacial tension between drop and solid γ_{SL}, as well as the surface energy of the solid sample in air (vapor) γ_{SV} can be correlated to each other via the Young's equation (2.8).

on the sample and a tangent is manually drawn to the drop via a goniometer-technique [79, 101]. The contact angle ϑ is formed due to the interaction of attractive cohesive forces at the molecules within the liquid and attractive adhesive forces between the molecules inside the drop and the surface. Upon reaching an equilibrium, the liquid-vapor surface tension γ_{LV} of the drop, the interfacial tension γ_{SL} between the drop and the solid substrate underneath and the surface energy γ_{SV} of the solid substrate in air (vapor) are related by the Young's equation from 1805 and illustrated in Figure 2.8 [111, 79, 168]

$$\gamma_{LV} \cdot \cos\theta = \gamma_{SV} - \gamma_{SL}. \tag{2.8}$$

Yet, due to the two unknown parameters γ_{SL} and γ_{SV}, this method can only give a starting point for determining the surface energy of the underlying substrate [79].

2.2.5 X-ray photoelectron spectroscopy

Using X-ray photoelectron spectroscopy (XPS), along with EDX, a sample can be analyzed with respect to its chemical composition and electronic structure. Unlike EDX, an incident beam of X-rays is used in this technique provoking photoemission. Thus, an electron from an inner-shell receives the energy from the X-rays and is therefore emitted from the sample (Figure 2.9). Its kinetic energy E_k can then be measured by an electron spectrometer and an X-ray induced photoelectron spectrum for the sample is gained. Since the obtained energy depends on the photon energy of the initial X-ray beam $h\nu$, the binding energy of the electron E_b as an intrinsic material parameter is calculated according to the following formula with Φ as the work function of the spectrometer [157, 26]

$$E_b = h\nu - E_k - \Phi. \tag{2.9}$$

The received photoelectron spectrum shows all electrons with a binding energy less than the incident $h\nu$ and thus, the electronic structure of the material is given. The peaks in the spectrum correspond to the emitted electrons which are elastically scattered without any energy loss, while the inelastic scattered electrons form the background of the spectrum [157].

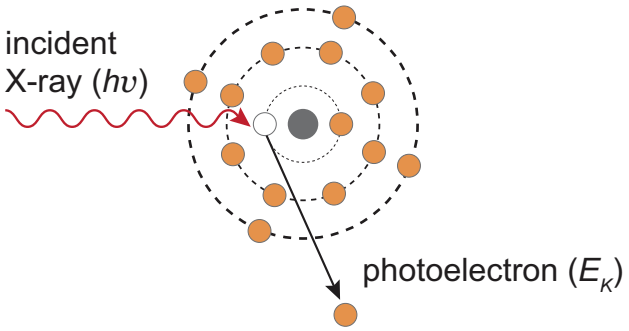

Figure 2.9: Scheme illustrating principle of XPS: An incident X-ray beam provokes the emission of an electron from an inner-shell, whose kinetic energy can be measured by an electron spectrometer and the intrinsic binding energy of the material can be calculated.

2.2.6 Dynamic light scattering

With the help of dynamic light scattering (DLS) the size of spherical particles in the nanometer-range can be measured by detecting their Brownian motion which is caused by collisions of the particles with the molecules in the solvent. Hereby, an increased speed of motion is observed for smaller particles compared to larger ones. During the measurement the temperature has to be controlled for evaluation due to its effect on solvent viscosity [73, 38, 60]. Then, the size of the particles with the hydrodynamic radius r_H can be calculated using the Stokes-Einstein equation

$$r_H = \frac{kT}{6\pi\eta D}. \tag{2.10}$$

with the Boltzmann constant k, the temperature T, the viscosity of the solvent η, and the translational diffusion coefficient D [73, 106]. Importantly, the hydrodynamic radius refers to the radius of a particle in the liquid with the same translational diffusion coefficient as the measured particle. Thus, the hydrodynamic radius can vary from the radius of the "real" particle due to adsorption of solvent molecules to it [106]. Additionally, the translational diffusion coefficient also depends on different parameters besides the size of the particle which cause changes to the measured radii. Surface structure, solvent and particle concentration, as well as the shape of the particles directly affect r_H [73].

For the DLS measurement, a vertically polarized laser is directed at the particles in a cuvette (Figure 2.10). Afterwards, the fluctuations in intensity of the scattered laser light are detected as a function of time. Hereby, the intensity I is correlated to the diameter of the particle d by $I \propto d^6$. Thus, bigger particles contribute significantly more to the observed laser intensity compared to smaller ones while at the same time smaller particles yield a much higher fluctuating intensity than bigger ones. These effects are analyzed by autocorrelating the obtained data from the detector in the time domain. This results in a particle size distribution of the measured spherical particles [73]. Yet, sedimentation and additional collisions between particles can falsify the analysis.

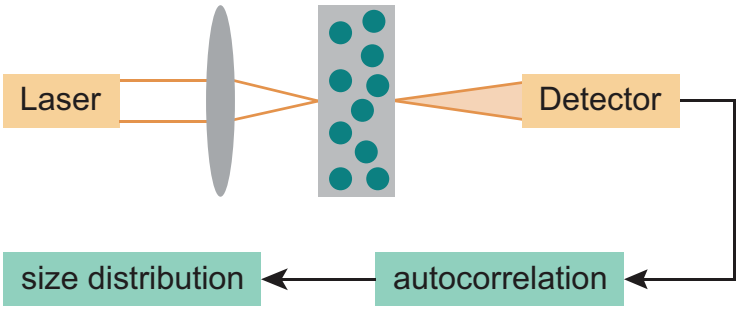

Figure 2.10: Scheme illustrating the principle of DLS: A vertically polarized laser is directed at the spherical particles. Its scattered light intensity is detected and compared to an autocorrelation yielding a size distribution of the measured particles.

2.2.7 Ellipsometry

Properties of thin films can be precisely measured using spectroscopic ellipsometry. Parameters such as layer thickness, surface roughness, interfacial layer formation and optical constants can be derived [144, 159, 95]. Ellipsometry detects noninvasively the change in polarization state of a light beam which is reflected on a solid flat sample. It yields the ellipsometric parameters Psi (Ψ) and Delta (Δ), correlated to each other according to the following formula

$$\tan(\Psi) \cdot e^{i\Delta} = \rho = \frac{r_p}{r_s} \tag{2.11}$$

with the Fresnel reflection coefficients of the sample r_p and r_s for p- and s-polarized light. p-polarized light is oriented in the plane of incidence while s-polarized light is oriented perpendicular to it [95, 159]. During the measurement, the complex ratio ρ is obtained as a function of wavelength which can then be converted to the optical constant index n and extinction coefficient k_{ext} of the sample material describing the way light behaves in the given material. This leads to the index and thickness of the layer. Hereby, the relative phase difference parameter Δ is especially sensitive for very thin films [95, 159]. Light is an electromagnetic wave and depending on orientation and phase, it is differently polarized, ranging from linearly to circularly to elliptically. In a spectroscopic ellipsometry analysis, a monochromatic light of known linear polarization reflects at the surface of the sample (Figure 2.11) and is then detected and analyzed as now elliptically polarized light [144, 159].

Since Ψ and Δ are obtained by ellipsometry, the film thickness and optical constants have to be extracted from the data. For analysis, a model of the different sample layers is created and its parameters are compared and adjusted with the measured experimental data. Thus, the difference quantified as the mean square error between the data has to be minimized in order to obtain good and valuable data [159, 95, 144]. One of the most common model functions to describe the dispersion behavior of transparent materials like alumina are the Cauchy equations, which will be used in this thesis

$$n(\lambda) = A_n + \frac{B_n}{\lambda^2} + \frac{C_n}{\lambda^4} + \dots \tag{2.12}$$

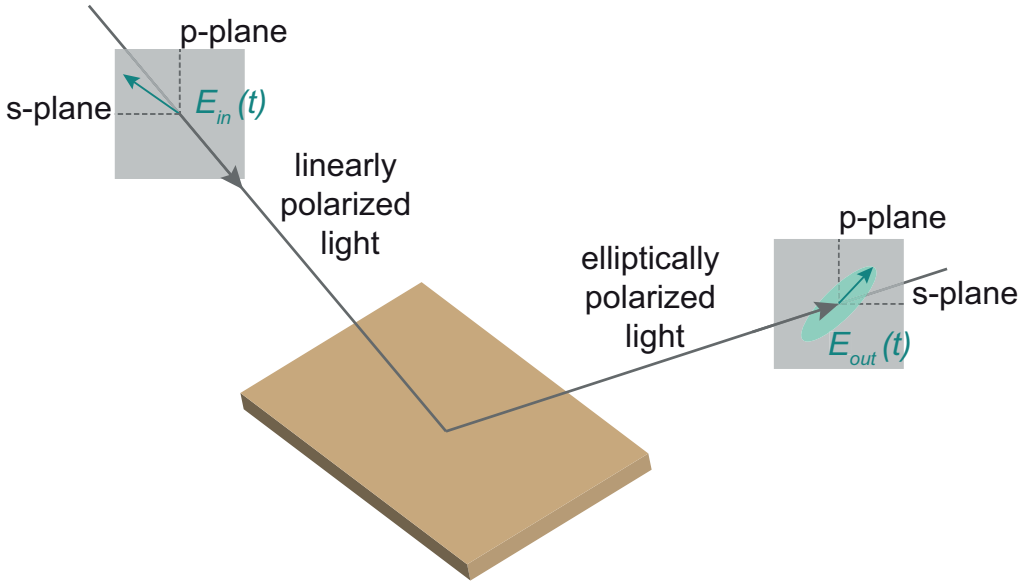

Figure 2.11: Scheme illustrating the principle of ellipsometry: A monochromatic light of known linear polarization (with its electromagnetic field $E_{in}(t)$) reflects at the sample surface and is then analyzed and detected as elliptically polarized light ($E_{out}(t)$) on the other side[159].

$$k_{ext}(\lambda) = A_k + \frac{B_k}{\lambda^2} + \frac{C_k}{\lambda^4} + \ldots \tag{2.13}$$

with the fitting parameters A_n, B_n, C_n, A_k, B_k and C_k, and the wavelength of light λ [45].

2.3 Materials and experimental methods

This section provides information about exact experimental procedures and the used chemicals for the different chapters. Furthermore, sample preparations and necessary details for the characterization of the specimens with the above mentioned techniques are given.

2.3.1 Synthesis of platinum nanoparticles on different substrates and their characterization in sinter studies

BCML-synthesis of Pt NPs

For all of the following experiments, Pt NPs were synthesized via the BCML-technique, as described in chapter 2.1. All glassware was cleaned in peroxymonosulfuric acid (mixture of concentrated 95-98 % sulfuric acid (Carl Roth) and 30 % hydrogen peroxide (Merck) at a ratio of 3:1) prior further handling. To produce the micelles for BCML, the block copolymer PS(400)-*b*-P2VP(64), synthesized by the DWI Aachen with a number average molar mass M_n(PS) of 41,600 g/mol and M_n(P2VP) of 6,700 g/mol, was dissolved in > 99.5 % toluene (Carl Roth) at a concentration of 3 mg/ml and stirred for 24 h. Hexachloroplatinic (IV) acid hexahydrate

($H_2PtCl_6 \cdot 6\ H_2O$) (Merck) with a molecular weight of 517.94 g/mol was added to the micelle solution at a loading ratio L of 0.35, calculated by the following equation

$$L = \frac{m(metal\,salt) \cdot M(PS-b-P2VP)}{m(PS-b-P2VP) \cdot M(metal\,salt) \cdot [Units\,VP]}. \tag{2.14}$$

with mass m, molar mass M and average amount of vinylpyridine monomers *[Units VP]*. After dissolution of the metal salt, micelles were then immobilized on different substrates by spin coating at 8000 rpm for 1 min on a WS-400B-6NPP Lite spin processor (Laurell Technologies). Prior to it, the solution was filtered with 0.2 µm syringe filters (Rotailabo PTFE, Carl Roth). Afterwards, the spin coated samples were exposed to a 10 % hydrogen / 90 % argon plasma (W10) (PS210 microwave plasma, PVA TePla) at 350 W and 0.4 mbar gas pressure for 45 min in order to remove the polymer and to reduce the platinum salt. Following this procedure, 6 nm Pt NPs with narrow size distribution were obtained in a quasi-hexagonal pattern with interparticle distributions ranging between 80 and 120 nm.

Size characterization of Pt NPs via TEM

The size of the Pt NPs was measured using TEM (CM 200, Philips) with a LaB_6-cathode at 200 kV and a CCD-camera (GATAN). For this purpose, TEM copper or gold grids with silica membranes and 400 mesh size (Plano) were cleaned in an oxygen plasma (GIGAbatch 360M, PVA TePla) at 150 W and 0.4 mbar gas pressure for 15 min. Afterwards, the Pt NPs were immobilized on the TEM grids by the placement of a 10 µl micelle solution drop onto it and a plasma-treatment with W10 gas, as described above. The nanoparticle size was analyzed from bright-field TEM-images with the software ImageJ (NIH).

Substrates for sinter studies

Two crystalline substrates, quartz crystal SiO_2(0001) +/- 0.5° and sapphire Al_2O_3(1-102) +/- 0.5° were bought from CrysTec. Amorphous silica SiO_2(ox) was obtained by oxidizing Si(100)-wafers (Siegert Wafer) in air at 750°C for more than 10 h to create an oxide layer of about 100 nm. The Central Scientific Facility Materials, MPI for Intelligent Systems, Stuttgart, manufactured the amorphous alumina Al_2O_3(a) via physical vapor deposition (PVD). Here, a 100 nm thick alumina layer was added onto Si wafers using a self-constructed Pfeiffer Vacuum Classic 500 FKM-sputtering machine. A sputter rate of 2 Å/sec, a process pressure of $7 \cdot 10^{-6}$ mbar, and a 99.99 % Al_2O_3-target (Target Materials) were used. All substrates were cleaned in peroxymonosulfuric acid prior the experiments.

To record the sintering of Pt NPs at the interface between SiO_2(ox) and Al_2O_3(a), dual-structured substrates were fabricated. As illustrated in Figure 2.12, negative photoresist (AR-N 7500.078, Allresist) was applied onto one half of the supporting silica or alumina substrate. A 50 nm-layer of the other respective material, alumina or silica, was deposited onto this layer via PVD by the Central Scientific Facility Materials, MPI for Intelligent Systems, Suttgart. Afterwards, Pt NPs were immobilized onto the substrates through spin coating at 8000 rpm for 1 min and treated in

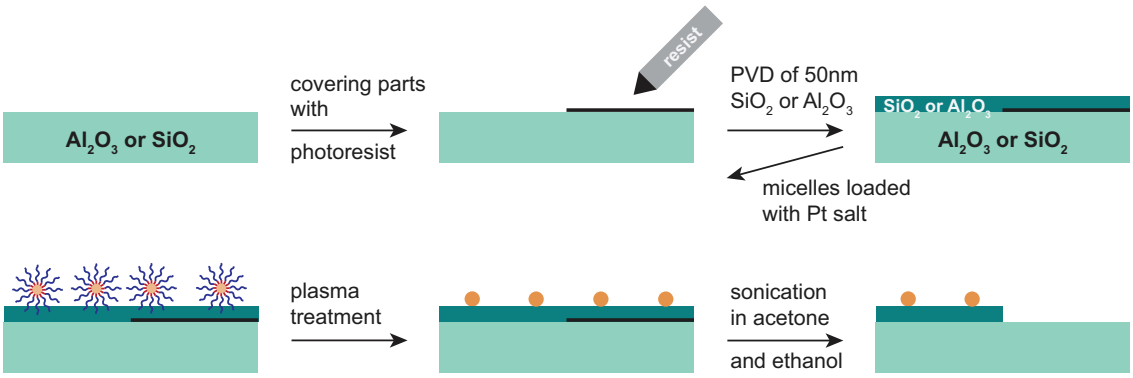

Figure 2.12: Preparation of dual-structured samples with Pt NPs: The supporting substrate (either silica or alumina) is partly covered with a photoresist. The superimposed material (either alumina or silica) is deposited onto the substrate and micelles loaded with platinum salt are spin coated onto it. After plasma treatment with W10-gas, the polymer is removed and the metal salt is reduced to Pt NPs. The photoresist and its superincumbent layers are removed in a final sonication step using an acetone-ethanol mixture.

a W10-plasma at 150 W and 0.4 mbar gas pressure for 45 min (100 Plasma System, PVA TePla). Finally, sonication in acetone (Carl Roth) and > 99.8 % ethanol (Carl Roth) at a 1:1-ratio for 1-3 min removed the resist and its superincumbent layer.

Annealing for sinter studies

The supported Pt NPs on the individual amorphous and crystalline silica and alumina wafers were annealed under atmospheric conditions at 750°C for up to 60 min in a chamber furnace (Nabertherm). However, for the sinter study on the dual-structured surfaces the NPs were placed in the oven for longer time durations ranging up to 6 h.

Characterization of Pt NPs for sinter studies

The analysis of Pt NPs on different substrates before and after annealing at 750°C was performed with SEM at 5 kV (Zeiss Ultra 55). Prior to the SEM-measurements, the samples were coated with a carbon layer of around 7 nm in an EM ACE200 carbon coating device (Leica Microsystems). The Inlens- and ESB-detector were used for imaging. Pt was confirmed to be present in the NPs on the dual-surface substrates by EDX in the SEM at 5 kV as well. Additionally, Pt NP height measurements on these substrates for particle size distribution calculations were conducted in tapping mode with PPP-NCHR tips (Nanosensors) on a MultiMode 8 AFM equipped with a NanoScope V controller (Digital Instruments, Bruker).

Characterization of substrate properties that influence Pt NP sintering

Adhesion of the Pt NPs onto the four different substrates, crystalline and amorphous silica and alumina, was studied in lateral force microscopy-mode at the AFM. The spring constant

of each DNP-S10 cantilever (Bruker) was determined for the individual substrates in a thermal tune process, yielding a value of approximately 0.2 N/m. The substrate roughness was studied with a PPP-NCHR tip (Nanosensors) in tapping mode and a scan rate of 0.6 Hz. The surface potential was measured with a Pt-Ir SCM-Pit tip (Bruker) and a lift scan of 45.6 nm by amplitude modulation Kelvin probe force microscopy at the AFM. For calibration-purposes, freshly polished nickel- and chromium-samples were used as references. The samples were prepared by affixing them on small metal plates with the help of Leit-Silver (Sigma-Aldrich). Lastly, the contact angles of ten 1 µl-water drops on the 10 mm x 10 mm-substrates were obtained at the contact angle measurement device OCAH 200 (DataPhysics Instruments). With the help of the SCA 20 software (DataPhysics Instruments) images of the drops were taken and tangents were manually placed at the perimeter of the drops, from which the contact angles could be calculated.

2.3.2 Sintering of platinum nanoparticles on tilted sapphire wafers

Cleaning and annealing of tilted Al_2O_3-wafers

Crystalline sapphire substrates with a (0001)-direction, $Al_2O_3(0001) < 0.1°$ were bought from CrysTec. Four different tilting angles of 0.1°, 4°, 9° and 15° towards the (1-102)-plane crystal orientation were tested in further experiments. In order to remove the amorphous layer at the surface generated during the polishing process by the company and to reveal the lattice planes, the sapphire wafers first had to be cleaned and annealed. For this procedure, they were rubbed with acetone and treated in an oxygen-plasma at 350 W, 0.4 mbar gas pressure for 45 min (GIGAbatch 360M, PVA TePla). In a second step, the wafers were annealed at 1400°C for 24 h with a heating and cooling rate of 10°C/min in a high temperature Supertherm HT oven (Nabertherm). Afterwards, the cleaning procedure with acetone and oxygen-plasma was repeated and the wafers were finally cleansed in peroxymonosulfuric acid prior the experiments.

Characterization of tilted Al_2O_3-wafers

The obtained topography of the tilted-substrates was studied with a PPP-NCHR tip (Nanosensors) in tapping mode and a scan rate of 0.6 Hz at the AFM. Further analysis of the step heights and step sizes was performed with the NanoScope Analysis 1.5-program (Bruker). Additionally, the surface potential at the lattice planes of 0.1°- and 15°-tilted alumina was measured with Pt-Ir SCM-Pit tips (Bruker) and Pt-Si FM-SPL-tips (Nanosensors), by frequency modulation Kelvin probe force microscopy at a Dimension Icon AFM (Bruker) equipped with a NanoScope V controller (Digital Instruments, Bruker). The samples were prepared by affixing them on small metal plates with the help of Leit-Silver (Sigma-Aldrich). For calibration-purposes, freshly polished nickel- and chromium-samples were used as references.

Sinter studies of Pt NPs on tilted Al_2O_3-wafers

For sinter studies, 6 nm Pt NPs, synthesized via the BCML-technique, were immobilized on the sapphire wafers via spin coating and plasma-treatment in W10-gas. Afterwards, the samples were

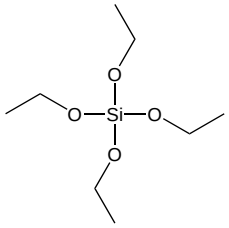

Figure 2.13: Chemical structure of tetraethyl orthosilicate (TEOS).

either directly placed into sample boats for sinter studies in air and annealed in a chamber oven at 750°C for up to 30 min or placed in glass-capillaries under vacuum and annealed in a tube furnace (Heraeus ROK F7, Heraeus). The latter sinter study was performed at 1200°C over a 48 h-time period. The characterization of Pt NPs on the sapphire substrates before and after annealing at the two different temperatures was performed with SEM. Prior to these measurements, the samples were coated with a carbon layer of approximately 7 nm to ensure conductivity. The Inlens-detector was used for imaging. For determining the NP size SEM-pictures with 2048 x 1536 pixels were taken at a magnification of 100 kx and their diameters were analyzed with the software ImageJ.

2.3.3 Silica and alumina layers for isolation of Pt NPs

Synthesis of silica layer

The SiO_2-film was formed through the preparation of a sol made from tetraethyl orthosilicate (TEOS) (Figure 2.13), according to the protocol of Rouse *et al.* [116].

A 0.01 M aqueous solution of TEOS was generated by adding > 99.9 % pure TEOS (Sigma-Aldrich) to Milli-Q-water and stirring it at approximately 400 rpm for 2 h. Then, a 0.1 M aqueous sodium hydroxide solution (NaOH), prepared with > 99.0 % pure 200 mg NaOH-platelets (Merck) in Milli-Q-water, was pipetted into the TEOS-water-solution to generate a TEOS:base-ratio of 35:1. This solution was stirred for 24 h before using it for experiments. 20 µl of it was spin coated onto amorphous alumina substrates immobilized with 6 nm Pt NPs at 3000 rpm for 1.5 min to form a film.

Characterization of silica layer and sinter study with platinum nanoparticles

First, the aging of the TEOS-solution was monitored by spin coating the sol onto amorphous-alumina substrates within a time period of 21 days. These samples were then characterized with tapping mode-AFM. Secondly, the chemical composition of the SiO_2-film was analyzed with a Thermo VG Theta Probe 300 XPS system (Thermo Fisher Scientific). A monochromatic Al K_α radiation was used as incident beam and spectral decomposition was performed by subtraction of a Shirley-type inelastic background. Also, the coverage of the Pt NPs with the silica layer was studied by TEM. Cross sections were prepared by glueing two identical samples together, cross-cutting with a tungsten-saw and grinding them with SiC sandpaper to a thickness of around

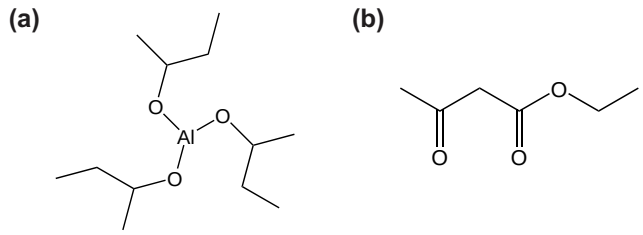

Figure 2.14: Chemical structure of (a) aluminum-tri-sec-butoxide (ASB) and (b) ethylacetoacetate (EAA).

300 µm. Afterwards, the samples were polished with diamond spray, thinned to approximately 30 µm through a dimple-process and lastly, thinned to its final thickness with the help of a precision ion polishing sytem mdel 691 (Gatan).

To study the sintering behavior of isolated Pt NPs with the SiO_2-film, the samples were annealed in a chamber furnace in air at 750°C for up to 4 h. Inlens- and SE2-images at the SEM allowed the optical characterization and evaluation of this phenomenon.

Synthesis of alumina layer

The Al_2O_3-layer was formed through the preparation of a sol made from alkoxide aluminum-tri-sec butoxide (ASB) (Sigma-Aldrich) with 97 % purity (Figure 2.14a), and a chelating agent ethylacetoacetate (EAA) (Sigma-Aldrich) with > 99 % purity (Figure 2.14b) , following the work of Nass *et al*. [100].

A 1.0 mol/l ASB-solution in anhydrous 99.9 % isopropanol (IPA) (Sigma-Aldrich) and a 1.0 mol/l EAA-solution in IPA were generated by individually stirring them for 1 h in a glovebox under nitrogen atmosphere to avoid ASB hydrolysis in the presence of water. Then, the two solutions were mixed at a molar ratio of 1:1 and allowed to stir for another 3 h. Simultaneously, a 0.33 mol/l aqueous solution of IPA (VWR International) was stirred for 1 h and afterwards, the ASB/EAA and aqueous IPA-solution were added to each other at a molar ratio of 1:1 with a peristaltic pump and a flow rate of 1.047 ml/min. The final solution was stirred for another 24 h and then allowed to age for a couple of weeks before using it for experiments. Prior to it, the solution was filtered with a 0.2 µm syringe filter (Rotailabo PTFE, Carl Roth) to remove agglomerates and dirt.

15 µl of the final solution was spin coated onto amorphous alumina substrates with 6 nm Pt NPs at 3000 rpm for 1 min to form a film. Afterwards, organic residues were removed from the samples through a heat treatment at 500°C for 1 h in a chamber oven.

Charcterization of alumina layer and sinter study with platinum nanoparticles

First, the particle sizes in the final sol were characterized by DLS at a Zetasizer 3000 HSA (Malvern Instruments). 1 ml of the solution was added to a cuvette and allowed to adjust to 25°C before starting the four measurements for 900 sec each. Additionally, the layer thickness of the spin coated alumina solution was determined with ellipsometry. The sol was spin coated onto

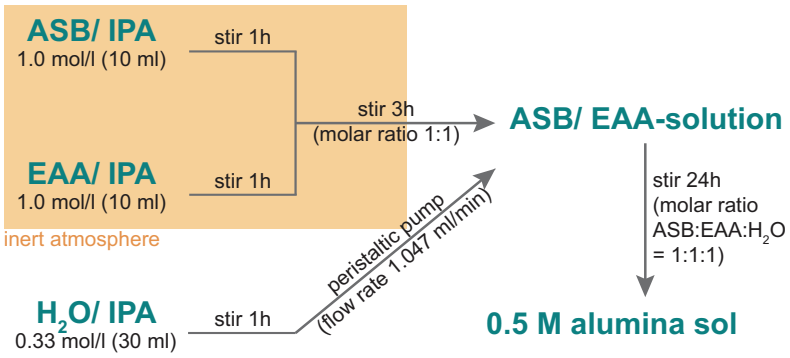

Figure 2.15: Scheme illustrating the synthesis of the ASB-EAA-stock solution for experiments to create an alumina-layer.

amorphous alumina substrates at different concentrations, ranging from 0.01 mol/l to 0.1 mol/l. The thickness of these samples was then measured at a M-2000 ellipsometer (J.A. Woollam). The obtained data was fitted to a model created with the Complete Software (J.A. Woollam) by using the Cauchy equations (Equations 2.12 and 2.13). The model consisted of a silicon wafer with a native silicon dioxide layer, an approximately 100 nm alumina layer and the thin spin coated Al_2O_3-layer deposited from the ASB-EAA-solution. Here, the mean square error was minimized to avoid fitting errors. Thirdly, the chemical composition of the Al_2O_3-film was analyzed with XPS, details listed above. At last, the coverage of the Pt NPs with the alumina layer was studied by TEM. Cross sections were prepared as described above with the silica layer.

To study the sintering behavior of isolated Pt NPs with this Al_2O_3-film, the samples were annealed in a chamber furnace in air at 750°C for up to 4 h. Inlens- and SE2-images at the SEM allowed the optical characterization and evaluation of this phenomenon.

3 Theoretical background for nanoparticle sintering

Metal nanoparticles supported on oxides, as described in the introduction (chapter 1), are used as catalysts for various chemical reactions. During these applications and especially at high temperatures, the NPs show highly dynamic behavior by moving across the surface, coalescing with other NPs, and changing their shapes under the reacting atmosphere [150, 149]. Sintering as a thermal degradation process of the NPs is a coarsening phenomenon mediated by mass transfer surface diffusion. Its successful control at the interface between metal and oxide are crucial for designing superior stable and active catalysts [32]. Two basic concepts have been proposed to describe NP sintering: Ostwald ripening (OR) and particle migration and coalescence (PMC). During OR, larger NPs grow at the expense of smaller ones through the diffusion of small adatoms towards larger particles, triggered by a chemical potential difference (Figure 3.1a). The driving force is the reduction in total free energy. Secondly, in the PMC-phenomenon NPs migrate on the surface and coalesce upon meeting (Figure 3.1b) [65, 44, 14].

Rate and diffusion equations help to model the observed NP behavior in kinetic experiments and are based on theories for nucleation- and growth-processes in thin films [150].

3.1 Atomic processes in crystal growth of thin films

Due to thermodynamic reasons, two-dimensional islands and three-dimensional clusters of atoms are usually more common compared to uniform coatings in thin film deposition processes. The

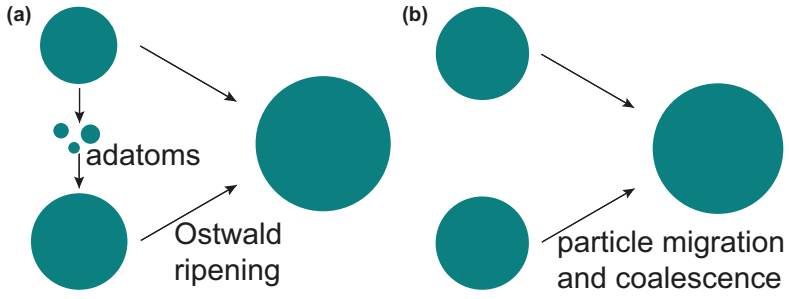

Figure 3.1: Scheme illustrating the basic concepts of (a) Ostwald ripening (OR) and (b) particle migration and coalescence (PMC). During OR, larger NPs grow at the expense of smaller ones through the diffusion of small adatoms towards the larger particles, triggered by a chemical potential difference. Yet, during PMC, NPs migrate on the substrate surface and coalesce upon meeting.

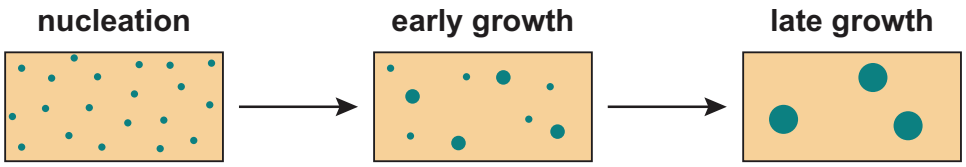

Figure 3.2: Scheme illustrating the different stages of cluster formation (nucleation) and growth [172].

formation and growth of clusters can be split up in three stages regarding their dynamics with its underlying fundamental surface processes. First, nucleation (Figure 3.2) of the clusters takes place when they reach a critical radius. Afterwards, an early and late growth stage follow, in which the nuclei develop a considerable size by capturing atoms from the supersaturated adatom gas phase first and then evolving by cluster-cluster interactions such as ripening and coalescencing [172]. Meanwhile, surface diffusion, adsorption and desorption processes are the determining factors for the clustering kinetics.

When trying to achieve a uniform film, three different growth modes can be distinguished depending on the relative surface energies of the materials. If material B is deposited onto the substrate, material A, and the corresponding surface energies γ_A and γ_B are related to each other with the effective interfacial energy $\gamma^*$of material B on material A by the following equation

$$\gamma_A + \gamma^{*>} \gamma_B \tag{3.1}$$

then, the growth of islands instead of a uniform thin layer will occur. This first growth mode is named Volmer-Weber system. Here, the atoms of material B are more attracted to themselves than they are to material A. On the other hand, if this condition does not apply, a uniform film can be produced as a Frank-van der Merwe-system. In this case, the atoms of the deposited material show higher bonding onto the substrate than they do towards themselves. When a combination of the above mentioned phenomena occurs, an intermediate layer- and island-structure is the result, which is known as a Stranski-Krastanov growth [17, 150, 149, 172].

During nucleation and growth, various atomic processes are happening at the surface. As can be seen in Figure 3.3, atoms first arrive from the vapor phase with a rate R

$$R = \frac{p}{\sqrt{2\pi mkT}} \tag{3.2}$$

and the gas pressure p, the atomic mass m, the Boltzmann constant k and the absolute temperature T. Thus, single adatoms are created on the substrate and their areal density $n_1(t)$ rises with time t, according to

$$n_1(t) = R \cdot t. \tag{3.3}$$

Regulated by temperature, these small adatoms stay on the substrate for a short adsorption residence time τ_a and migrate with the diffusion coefficient D.

$$\tau_a^{-1} = \nu_a \cdot e^{\frac{-E_a}{kT}} \tag{3.4}$$

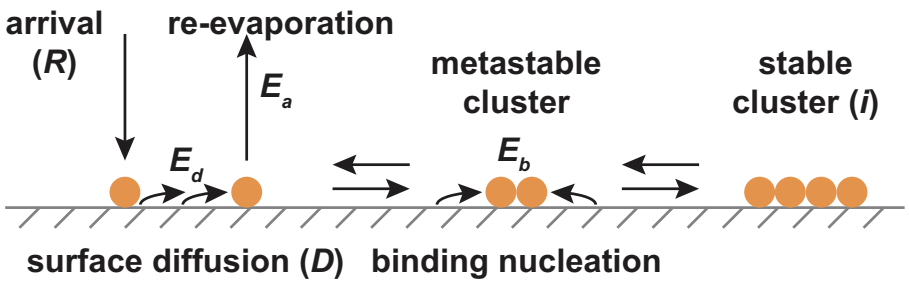

Figure 3.3: Atomic processes occuring on the surface during nucleation and growth of stable metal clusters or thin films [150, 148].

Hereby, the residence time is controlled by the atomic vibration frequency ν_a and the adsorption energy E_a. The diffusion coefficient can be described in a simple term with the diffusion frequency ν_d, which is usually smaller than ν_a, the diffusion energy E_d and the jump distance a

$$D = \frac{\nu_d a^2}{4} \cdot e^{\frac{-E_d}{kT}}. \tag{3.5}$$

Therefore, the following average migration length x of the adatom before it evaporates again can be calculated by

$$x = \sqrt{D\tau_a} = \frac{a}{2}\sqrt{\frac{\nu_d}{\nu_a}} \cdot e^{\frac{E_a - E_d}{2kT}}. \tag{3.6}$$

While the adatom diffuses across the substrate, it meets other adatoms and they can form small clusters depending on their binding energy E_b towards each other and their areal density. Later on, this process can continue forming larger, and larger clusters [150].

Different surface diffusion processes are reported for metal nanoparticles on substrates. Surface diffusion is defined as a stochastic process of mass transport due to the driving force of a local chemical potential. This transport is described according to Fick's second law by

$$\frac{\delta c}{\delta t} = \frac{\delta}{\delta x}\left(D \cdot \frac{\delta c}{\delta x}\right) \tag{3.7}$$

with the concentration c [145]. One of the observed diffusion mechanisms for single metal atoms on metal surfaces is a hopping phenomenon, in which an adatom randomly moves over the surface by thermal activation. If a driving force like a chemical potential gradient acts on the adatom, its random movement will preferentially occur along the maximum gradient direction of the decreasing chemical potential [147]. Other possible mechanisms are the tunneling of metal particles, which is often observed for light atoms such as hydrogen, and the atomic exchange as in interdiffusion, where an adatom changes sites with a nearest neighbor substrate atom [147, 149].

Generally, these nucleation and diffusion processes are altered in the presence of surface defects, which can change the diffusion coefficient and the binding energy of the adatom to the substrate [148]. Lattice steps can hinder the migration of adatoms and atom clusters on a surface as diffusion barrier, trap adatoms at its boundary or guide them along the step. When an atom reaches the lattice step from the upper side, it is either stopped there and reflected while remaining on the upper step side, or it can cross it [145]. Hereby, the atoms first encounter an energy barrier

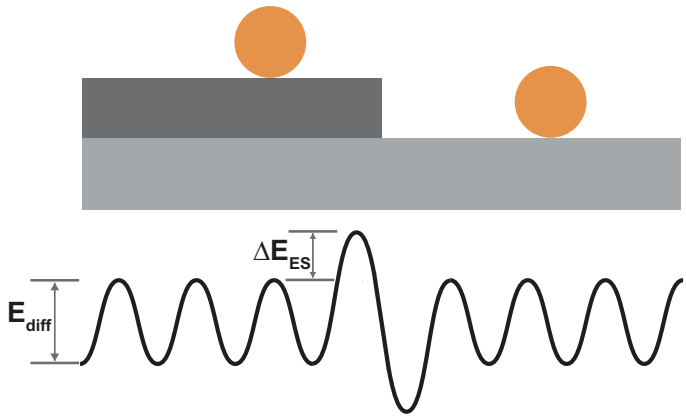

Figure 3.4: Scheme illustrating the Ehrlich-Schwoebel (ES) barrier with the diffusing energy E_{diff} of the particles on the substrate and the energy barrier ΔE_{ES}, which acts on the NPs encountering the lattice step.

ΔE_{ES} at the step edge, which is called the Ehrlich-Schwoebel (ES) barrier. This especially occurs at lower temperatures, where the particles are less able to surmount it (Figure 3.4) [149].

In later growth stages, not only do single atoms diffuse over the surface, but 2D islands or 3D clusters of atoms migrate as well. One possible mechanism is the temporary stretching of atom-bonds in the cluster. Movement results when the stretching happens in a whole chain. Otherwise, metallic clusters can migrate over a metal surface through a random diffusion of atoms at the periphery or at a step edge. Also, these last mentioned atoms can detach from a cluster, diffuse across the substrate surface and attach again to the same one or to a different cluster nearby, changing its size and shape [147]. Thus, a displacement of the NP's mass centre is obtained and it can be modelled either by a random walk problem for a single adatom close to this step edge or by a continuum equation with a noise term reflecting fluctuations of the cluster periphery [145]. And lastly, the whole cluster can diffuse and glide over the substrate by thermal activation [147].

In this late growth stage, the clusters then start to coalesce, when growing into each other and if the cluster density on the surface is sufficiently high enough. Otherwise, differently sized clusters interact with each other upon overlapping of the diffusion length of its individual adatoms. Due to a difference in concentation, smaller clusters will shrink and larger ones will grow in this OR-process [145, 172]. A first theoretical and analytical model for OR was reported by Lifshitz and Slyozov in 1961 and further improved by Wagner, known as LSW theory [82, 152, 83]. The Gibbs-Thomson effect is used as a driving force, which relates the droplet solubility $c(r)$ to its radius r of curvature according to

$$c(r) \propto e^{\frac{1}{r}}. \tag{3.8}$$

Therefore, larger clusters are favored and more stable compared to smaller ones [145].

To gain information about the relationship between Pt NPs and the underlying oxide substrate, as it is of interest for this PhD thesis, information of thermodynamically favored processes for the metal-oxide interface can be found in the literature. For example, when Pt is deposited onto an

oxide such as alumina or silica, one possible phenomenon then could be its oxidation to platinum oxide.

$$\text{Pt (s)} + \text{Al}_2\text{O}_3/\text{SiO}_2\text{ (s)} \rightarrow \text{PtO}_x\text{ (s)} + \text{Al/Si (s)}$$

This can only happen, if the reaction has a negative standard free energy change $\Delta H < 0$ [32]. Yet, the affinity of platinum as a late transition metal to oxygen is very low compared to other metals and to aluminum and silicon in Al_2O_3 and SiO_2. Thus, this reaction is very unlikely to occur. Otherwise, as a second phenomenon stable intermetallic compounds can be found for some metals A on oxide substrate BO.

$$2\text{ A (s)} + \text{BO (s)} \rightarrow \text{AO (s)} + \text{AB (s)}$$

This is especially reported with silica as the substrate BO. Hiraki *et al.* for example described the identification of a Pt_2Si and PtSi phase upon the annealing of a Pt-Si interface, when depositing platinum on silicon [70]. Also, other mixed oxides such as $NiAl_2O_4$ were detected when exposing a nickel catalyst onto an alumina substrate [115].

A last possible theory of prevailing interactions in a metal-oxide system is the wetting of the metal on the substrate. Following equation 3.1, the metal-oxide interfacial free energy has to be matched with the individual surface energies of the metal and the oxide. Although no explicit values of these energies are available for platinum on alumina or silica, the general reported trend is that mid-to-late transition metals, including platinum, do not wet oxides like alumina and silica according to this thermodynamic criterion [32].

3.2 Nanoparticle sintering models

Derived from models of atomic processes in thin films, it has been tried to describe NP sintering with theoretical equations aiming at forecasting the sintering kinetics and the development of the particle size distributions (PSDs) over time. Generally, a growth law according to

$$\bar{d}^q - \bar{d}_o^q = Kt \tag{3.9}$$

can be obtained with the average diameter $\bar{d}$ over time t, the initial mean diameter d_0, a temperature-dependent constant K and a varying integer q for the different sintering mechanisms [66]. Following, models for PMC and OR are presented.

3.2.1 Particle migration and coalescence

The mobilities of NPs at a certain temperature can be calculated using the particle diffusion coefficient D_p. Then, the probability of NP migration and coalescence can be evaluated. Following Fick's diffusion law, D_p for spherical particles can be expressed as a function of the

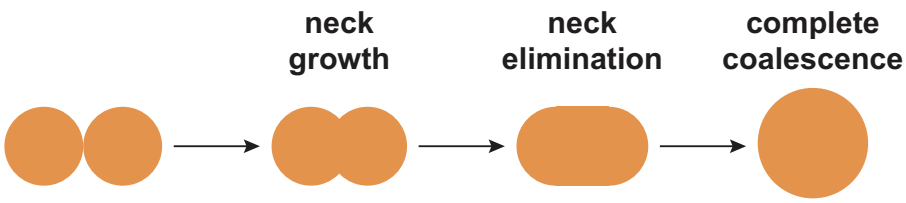

Figure 3.5: Scheme illustrating the PMC process of coalescing nanoparticles with the intermediate stages of neck growth and neck elimination [6, 164].

surface self-diffusion coefficient D_s, the atomic diameter d_a and the particle diameter d by the following equation [66]

$$D_p = \frac{24}{\pi} \cdot \left(\frac{d_a}{d}\right)^4 \cdot D_s. \tag{3.10}$$

Hereby, D_s is determined by the frequency factor D_{s0} and the activation energy E_{act}

$$D_s \approx D_{s0} \cdot e^{\frac{-E_{act}}{kT}}. \tag{3.11}$$

Inserting experimentally observed values for D_{s0} and E_{act} of platinum, reveals that migration distances x of spherical Pt NPs depend strongly on the diameter of the particles, as presented by Harris *et al.*

$$x = 2 \cdot \sqrt{D_p t}. \tag{3.12}$$

During a time interval t of 2 h, a NP migrating distance of more than 10 µm for NPs with a diameter of 1 nm is calculated. In contrast, NPs with a diameter of 5 nm only migrate 540 nm [66, 24]. Thus, if the interparticle distance is known, the probability of particles migrating towards each other and subsequently coalescing can be assumed.

To obtain the sintering kinetics of supported NPs, Ruckenstein and Pulvermacher reported a theoretical approach for the PMC-mechanism [117, 118]. Under the restriction of only binary collisions, they describe the evolution of the number of NPs per unit area on the support n_k over time by

$$\frac{dn_k}{dt} = \frac{1}{2} \sum_{i+j=k} K_{ij} n_i n_j - n_k \sum_{i=1}^{\infty} K_{ik} n_i. \tag{3.13}$$

Hereby, n_k increases when i NPs coalesce with j NPs while $i + j = k$. Otherwise, it decreases when k NPs coalesce with any other particle. The coefficients K_{ij} and K_{ik} represent rate constants for collisions between two particles and the factor $\frac{1}{2}$ in front of the first term excludes counting the occuring interactions twice. Depending on whether the NP sintering process is limited by the diffusion of the migrating particles towards each other or if it is restricted by the coalescence of the particles, different equations for these coefficients have been derived [66]. Ruckenstein and Pulvermacher were thus able to modify the simple growth law (equation 3.9) for PMC to express the change of surface area over time with the exponent $q = 7$ as following

$$\bar{d}^7 - \bar{d}_o^7 = Kt \tag{3.14}$$

while the coefficient K is dependent on K_{ij} [66].

Asoro *et al.* reported to observe the PMC mechanism of around 3 nm Pt NPs with a scanning-transmission electron microscope by tracking the neck growth stage, which is schematically illustrated in Figure 3.5. Afterwards, the neck is eliminated until complete coalescence is reached [164]. Through mass transport mechanisms including grain boundary, surface and volume diffusion, this stage is thermodynamically favored through the reduction in chemical potential at the contact points of the NPs [6].

3.2.2 Ostwald ripening

On the other hand, NP sintering can be governed by OR. Based on the work of Lifshitz and Slyozov [82] and lateron Wynblatt and Gjostein [165, 163, 164], theoretical models for OR can be established with the Gibbs-Thompson relation (equation 3.8). These theoretical equations describe the evolution of NPs' radii over time when metal adatoms detach from smaller particles, diffuse randomly on the substrate and preferentially attach to larger particles. The interparticle transport of adatoms is illustrated in the upper graph of Figure 3.6. The average metal adatom concentration on the oxide substrate is presented as $\bar{c_s}$ ($\underline{c_s}$), the adatom concentration right next to the particle as $c_s^{'}$ and the adatom concentration on the NP's surface as c_p [66, 105]. If $c_s^{'} < \bar{c_s}$, the adatoms will diffuse from the substrate towards the particle with a radius larger than the critical one. Against it for $c_s^{'} > \bar{c_s}$, the adatoms will preferentially detach from the particle and diffuse onto the oxide. The energy needed for the adatom to attach to or detach from the particle is shown in the lower graph of Figure 3.6 with $H_{ps} + H_{sm}$. H_{ps} represents the respective enthalpy difference between the bound state of the adatom onto the particle and its state on the substrate as freely diffusing adatom, while H_{sm} is the migration energy of the adatom on the substrate. $E_{ad,m}$ stands for the sublimation energy of the bulk maderial and $E_{ad,s}$ for the sublimation energy of the support.

On the basis of this plot (Figure 3.6) and subsequent considerations, kinetic equations for two different rate-limiting cases are obtained. In the first one, OR is restricted by the detachment and attachment of the adatoms at the NP's edge, termed interface controlled. Here, the radius of each NP develops over time as a function of the critical radius $r*$ by

$$\frac{dr}{dt} = \frac{\sin\theta \cdot s\beta\beta^{'} c_p^{eq} \gamma_m \Omega^2}{\alpha_1 kTr^2} \cdot \left(\frac{r}{r^*} - 1\right). \tag{3.15}$$

Yet, in the second case, OR can also be limited by the diffusion rate of adatoms between the nanoparticles, referred to as diffusion controlled. Thus, the following equation for $r(t)$ is derived

$$\frac{dr}{dt} = \frac{D_1 \beta c_p^{eq} \gamma_m \Omega^2}{\ln\left(\frac{l}{r\cdot\sin\theta}\right) \alpha_1 kTr^3} \cdot \left(\frac{r}{r^*} - 1\right). \tag{3.16}$$

For equations 3.15 and 3.16, the radius of the particle is presented by $r \cdot \sin\theta$, as sketched in Figure 3.6. s is the interatomic spacing, c_p^{eq} the adatom concentration of an indefinitely particle,

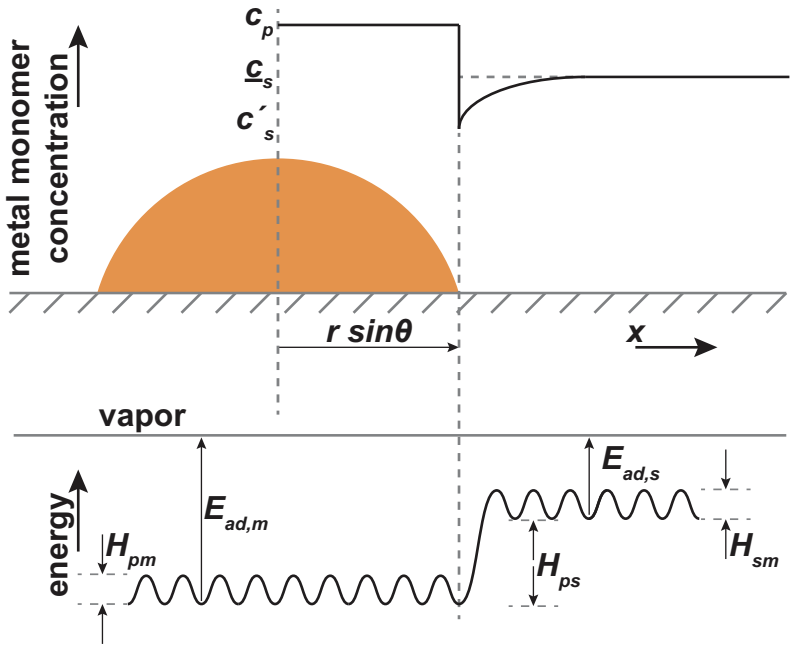

Figure 3.6: Scheme illustrating the concentration of metal adatoms on a substrate surface in the upper picture and the corresponding energetics in the lower picture [66, 105].

γ_m the surface energy and Ω the atomic volume of the metal particle. l represents the distance from the NP's center until the adatom concentration reaches $\bar{c_s}$, D_1 the diffusion coefficient of the monomer on the oxide, k the Boltzmann constant and T the temperature in Kelvin. Additionally, a geometry factor depending on the structure of the NP with $\alpha_1 = 0\ 25 \cdot (2-3\cdot\}\cos\theta + \cos^3\theta)$ is introduced. Furthermore, the jump frequency of the adatoms on the oxide is described by $\beta' = \nu_s \cdot e^{\left(\frac{-H_{sm}}{kT}\right)}$. Here, ν_s is the vibrational frequency of an adatom on the support. Additionally, $\beta = \frac{\nu_p}{\nu_s} \cdot e^{\left(\frac{-H_{ps}}{kT}\right)}$ is used with the vibrational frequency of an adatom on the particle ν_p to obtain the equations 3.15 and 3.16 [105, 66]. Wynblatt and Gjostein were then able to express the change of surface area over time for diffusing adatoms on the oxide substrate during OR by the simple growth law (equation 3.9) with the exponent $q = 4$ and a rate constant A_d depending on D_1 as following [66]

$$\bar{d}^4 - \bar{d}_o^4 = \frac{27}{32} A_d \cdot t. \tag{3.17}$$

Additionally to the migration of metal adatoms on the oxide substrate, the diffusion can also take place by metal oxide adatoms when under oxidizing conditions. As example, platinum oxide can form on alumina and silica in air by [71, 72]

$$2\ \mathrm{Pt\ (s)} + \mathrm{O_2\ (g)} \rightarrow \mathrm{PtO}_x\ \mathrm{(g)}.$$

The reported changes in enthalpy for the above shown reaction of platinum to platinum oxide are significantly smaller than the energy needed for platinum to evaporate or for adatoms to leave a particle and diffuse on the oxide substrate. So, in the presence of oxygen, the formation of platinum oxide appears to be thermodynamically more favorable. Thus, the platinum oxide can either diffuse on the substrate or migrate through the vapor phase towards larger particles. While

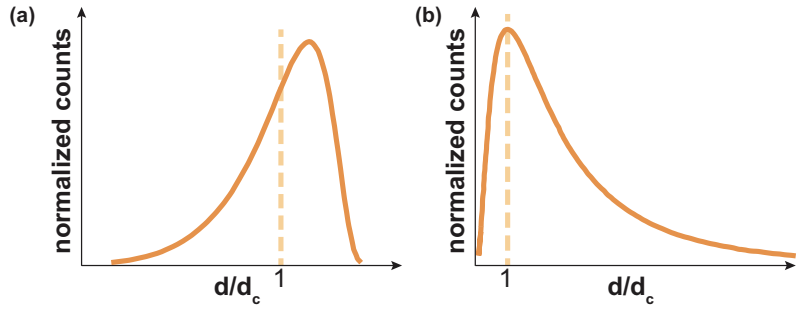

Figure 3.7: Calculated PSDs for the two sintering mechanisms: (a) OR and (b) PMC, according to [44].

the coefficient for the growth law continues to be $q = 4$ for the diffusion of platinum oxides on the substrate, for the vapor phase transport the equation 3.9 changes to

$$\bar{d}^2 - \bar{d}_o^2 = \frac{1}{2} \cdot A_v t \tag{3.18}$$

with the rate constant A_v [66]. Yet, the exponent q is reported to decrease with progressing time or with increasing temperature [66].

3.3 Characteristics and influencing factors of nanoparticle sintering

With the above described equations, graphs for the evolution of the particle size distribution (PSD) after sintering for a certain time can be evolved. Summarized by Datye *et al.*, two different PSDs are obtained for the sintering of metal nanoparticles on oxide supports for OR and PMC, as illustrated in Figure 3.7. Distinguishing features are the asymmetric shape which is skewed to the left for OR with the observation of very small particle and skewed to the right for PMC. In this case, tiny particles are absent due to the migration and coalescence of the particles without forming adatoms or without the shrinkage of these. Secondly, a cut off size with a diameter below twice the mean diameter is mentioned for OR, while the graph for PMC displays a tail towards large particles [44, 61, 164].

So far, the dominating mechanism for NP sintering was discovered either by applying these illustrated differences to the experimentally observed PSDs or by extracting the slope of the curve from the simple growth laws as discussed above with equations 3.14, 3.17 and 3.18 [65]. Hansen *et al.* distinguish three qualitative phases for the sintering of metal NP as heterogeneous catalysts [65]: The first one is characterized by a rapid decline in surface area due to the loss of small particles, as well as a slow increase in the size of bigger particles, obtained by Monte Carlo simulations. Thus, it can be concluded that OR is the governing sintering mechanism at the beginning with Brownian motion of larger particles only minorly contributing to the sintering if at all. Then in the second time interval, the rate of surface area decline slows down. TEM experiments of samples in phases two and three show stationary particles supplementary to larger ones which migrated and coalesced upon contact when they were in

close proximity towards each other. Yet, other phenomena such as the sintering of the support can take place in the third stage when the Tammann temperature $T_{Tammann}$ of the support has been exceeded with $T_{Tammann} = 0\ 52 \cdot T^{bulk}_{melting}$. At this temperature (in Kelvin) surface atoms start being mobile [65, 12]. However, in agreement with Moulijn *et al.*, Hansen *et al.* came to the conclusion that the dominating mechanism for NP sintering is the surface migration of adatoms rather than of whole particles [65, 97]. Also, Datye *et al.* negated that the sintering mechanism can be derived from PSDs. Their arguments include that all experimentally obtained PSDs for OR- and PMC-conditions could be fit to the same PSD shape, as well as that no evidence of a PSD skewed to the left was received for OR-governing experiments due to the lack of tiny particles. This could be caused by a PMC mechanism of the adatoms, their instability at high temperatures or by the limitation of analytical methods to detect them. Additionally, the cut-off reported for OR could not be seen in sinter studies and thus, a right-skewed PSD should not be exclusively appointed to a dominating PMC-mechanism [44].

Parameters influencing the sintering of metal nanoparticles

Sintering is strongly dependent on temperature, time, atmosphere, and support, as well as the metal used in the catalyst, its loading and its preparation [15]. As the most important variable, high temperatures significantly enhance the sintering. Also, it greatly varies in different atmospheres. Thereby, a water- or oxygen-containing atmosphere causes much more NP coarsening compared to an exclusive hydrogen- or nitrogen-environment [15, 74]. This can, for example, be caused by a favored formation of metal oxide adatoms in the presence of oxygen. The choice of material also influences the sintering behavior with its thermal stability correlating to the material's sublimation energy under reducing or inert atmospheres. Also a decreasing loading ratio of NP catalyst on the support slows down the coarsening due to an increased interparticle distance. Additionally, the support can have a strong impact on the NP's stability at elevated temperatures. The value of metal-support interactions dictates the wetting behavior of the metal, the mobility of the nanoparticles and the rate of adatom detachment and attachment on the particles [15, 19]. For example, rare earth oxides such as ceria stabilize the metal nanoparticles in the catalyst through their ability to act as an "oxygen storage". If it is used additionally to another oxide support, such as γ-alumina, ceria can hinder phase transformations of the alumina which would otherwise lead to a subsequent surface area decline. By the "strong metal-support interaction" effect, the metal particles are anchored onto the ceria through a Ce-O-Metal bond, as introduced in chapter 1 [33, 13, 11, 98, 36, 22]. Hereby, more metal-support interactions are directly proportional to a higher thermal stability. An increased support surface area as physical property of the underlying substrate also reduces the sintering speed of metal nanoparticles [15]. In addition, heterogeneities in the support surface change NP coarsening behavior. As demonstrated by Tabib Zadeh Adibi *et al.*, these heterogeneities cause bimodal or multimodal particle size distributions in experimental TEM-sinter studies with 3 nm Pt NPs on alumina and silica [139].

Learning from these parameters, some attempts were made to prevent NP sintering. Wettergreen *et al.* reported an increased thermal stability of Pt_{22} and Pt_{68} clusters through size selection and thus eliminated the main driving force of chemical potential difference in OR [158]. Other

improvements could be achieved by alloying the metal nanoparticles with a second metal material of higher melting point, such as Rh in Pt NPs, or by encapsulating the nanoparticles in a thermally stable and chemically inert oxide shell [33, 65].

4 Sintering of platinum nanoparticles on amorphous and crystalline silica and alumina

Pt NP sintering has been studied on different substrates under various conditions. Techniques comprising TEM, both *in* and *ex situ*, and AFM [125, 126], 2D- and 3D-indirect nanoplasmonic sensing (INPS) [80, 137], high-pressure XPS [108] and in situ high-energy grazing incidence X-ray diffraction at a synchroton [67] have all been used to examine the thermal deactivation of the NPs on γ- and amorphous alumina, as well as on silica. Yet, although these substrates have been compared with each other regarding their suitability as Pt NP catalyst substrates, neither their physical and chemical substrate parameters nor their influence on the sintering behavior of Pt NPs have been examined experimentally. Thus, in this chapter the sintering behavior of ~6 nm Pt NPs on both crystalline and amorphous SiO_2 and Al_2O_3 after thermal aging in air using a simplified model sytem was observed with scanning electron microscopy. Particle size distributions (PSDs) as a function of aging time were evaluated with AFM. The investigated parameters included Pt NP adhesion to the substrates measured with LFM, surface roughness analyzed using tapping mode-AFM, the surface potential of the substrates obtained by KPFM and surface energy received by contact angle measurements. Additionally, the behavior of the Pt NPs on dual-structured amorphous SiO_2- and Al_2O_3-substrates during high temperature treatments was investigated with a specific interest concerning the NPs' behavior at the interface between these two materials.

4.1 Platinum nanoparticles synthesized via block copolymer micellar nanolithography

For this work, Pt NPs were synthesized via the BCML-technique. With the block copolymer PS(400)-b-P2VP(64) at a concentration of 3 mg/ml and a metal salt loading of 0.35, 5-6 nm sized Pt NPs were fabricated in toluene in a quasi-hexagonal pattern. In the SEM image Figure 4.1a, the regular arrangement of the NPs can be seen and in Figure 4.1b, the quasi-hexagonal structure is pointed out. This is caused by the attractive capillary forces during evaporation of the toluene and repulsive steric and electrostatic interactions between the micelles [84]. Since the platinum salt, hexachloroplatinic acid hexahydrate, does not stabilize the micelles as well as other precursor salts, such as the one for gold nanoparticles, the monodispersity is not ideal and not all Pt NPs are perfectly hexagonally arranged [74]. In Figure 4.1c, the particle sizes of the synthesized nanoparticles are presented and reveal a highly narrow particle size distribution with a mean

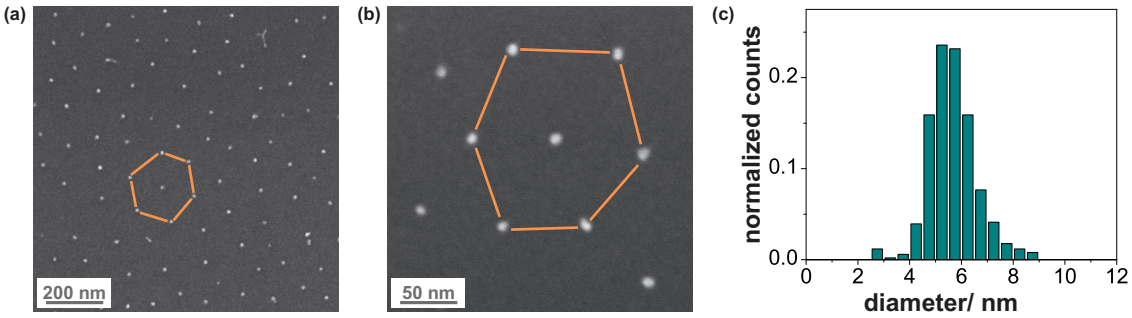

Figure 4.1: (a) and (b) SEM images of Pt NPs synthesized with the BCML technique, which results in a quasi-hexagonal pattern. (c) Size distribution of the synthesized Pt NPs centered around 5-6 nm and was obtained by TEM.

diameter of 5.67 nm and a standard deviation of 0.92 nm. This result was obtained by analysis of more than 500 Pt NPs in bright-field TEM pictures at a magnification of 175 kx and by image processing with the software ImageJ. These NPs were used for all further experiments to study their coarsening behavior at high temperatures on different substrates.

4.2 Sinter studies with scanning electron and atomic force microscopy

These 6 nm sized Pt NPs were immobilized on four different substrates: crystalline quartz SiO_2(0001), thermally oxidized silica SiO_2(ox), crystalline sapphire Al_2O_3(1-102) and amorphous alumina Al_2O_3(a). Their sintering behavior was studied in air at 750°C for 60 min. In the following Figures 4.2, 4.3, 4.4 and 4.5, SEM images of the resulting Pt NP coarsening are shown. Additionally, corresponding PSDs were obtained from height measurements in the AFM and are presented below the SEM images. Pt NPs on all four substrates were organized in a regular quasi-hexagonal pattern and exhibit a narrow Gaussian-shaped height distribution in the AFM graphs centered around 4-5 nm directly after BCML synthesis.

4.2.1 Crystalline quartz SiO_2(0001)

On the crystalline silica, the structure of the Pt NPs starts to degrade after 10 min at 750°C, resulting in larger, sintered NPs (Figure 4.2). After 20 min, the original structure is no longer discernible and the particle sizes have increased considerably. Following this trend, the NP coarsening on the crystalline silica continues at 30 and 45 min until only few large platinum particles can be seen in the SEM image at the 60 min-time point. Interestingly, a light shadow around the sintered NPs can be seen from 10 to 60 min. This is most likely induced by wetting of platinum clusters which are attaching to the larger particles and thus, provoke the build-up of these few massive ones. Accordingly, the PSDs of the Pt NPs have undergone substantial change from 0 to 60 min. The formerly sharp Gaussian-shaped distribution broadens with a clear tail towards larger sizes. In Table 4.1, the extracted mean height, standard deviation and the number of evaluated NPs from the PSDs are presented for each time interval. Even though the nanoparticles

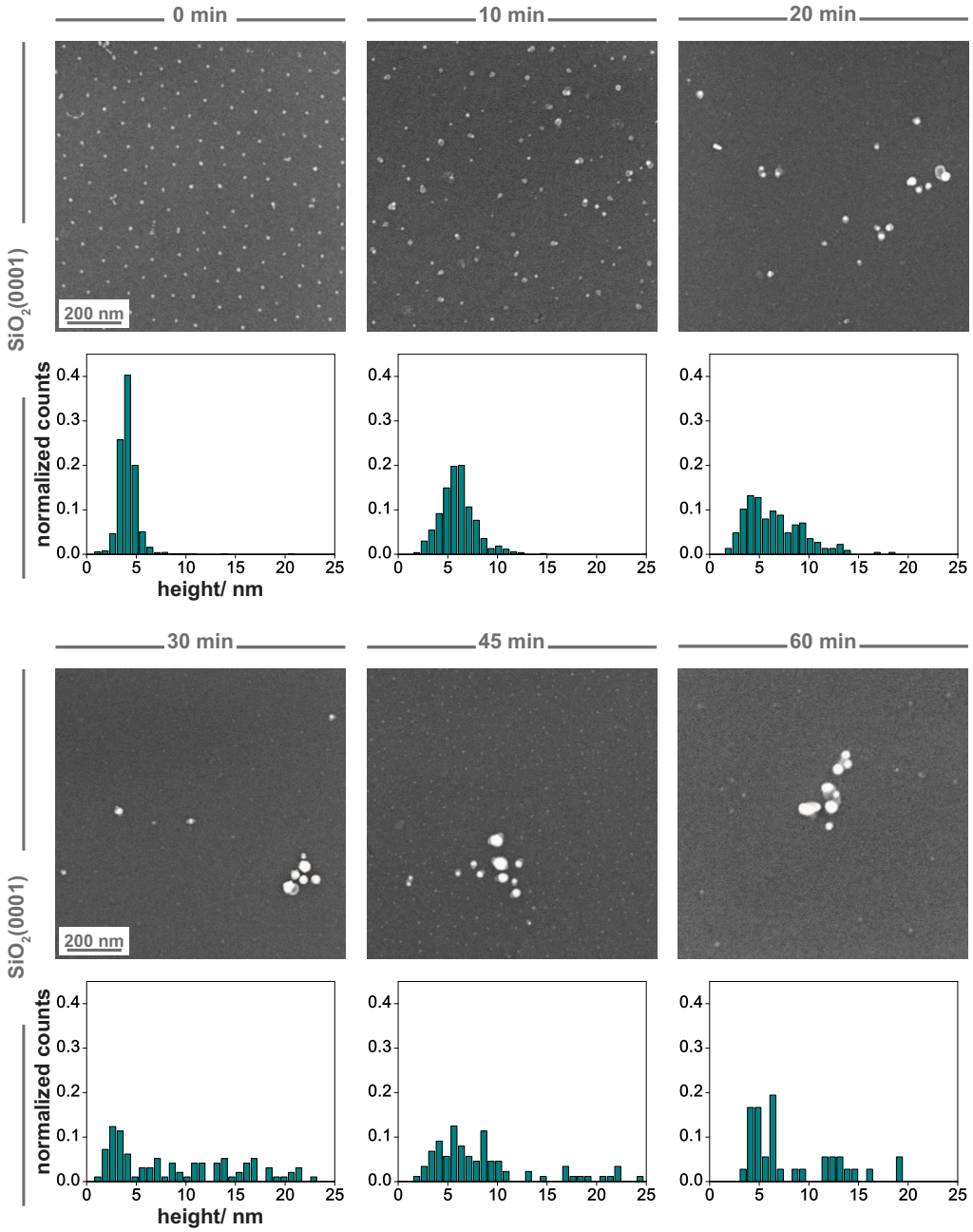

Figure 4.2: SEM images and corresponding PSDs of Pt NPs on $SiO_2(0001)$ during sinter studies in air at 750°C after different time periods. The scale bar in all SEM pictures represents 200 nm.

	0 min	10 min	20 min	30 min	45 min	60 min
mean height	4.19	6.01	6.47	9.69	9.18	8.19
standard deviation	1.00	1.75	2.90	6.80	6.28	4.54
number of NPs	1598	535	227	100	88	36

Table 4.1: Mean heights, standard deviations and the numbers of evaluated NPs extracted from PSDs obtained with AFM for the sintering of Pt NPs on $SiO_2(0001)$.

are approximately 5.5 to 6 nm in size in the TEM measurements, the obtained NPs' heights are lower in the AFM. This is caused by flattening of the initial spherical particles and their wetting on the substrate. Albeit the mean height and standard deviation are calculated from a far-from Gaussian-shaped distribution; they give a first indication of the NP size or height evolution over time at 750°C.

It can be seen that the NPs coarsen from a mean height of 4.19 $\pm$ 1.00 nm at 0 min via 6.01 $\pm$ 1.75 nm and 6.47 $\pm$ 2.90 nm at 10 and 20 min to the larger values of 9.69 $\pm$ 6.80 nm at 30 min, 9.18 $\pm$ 6.28 nm at 45 min and 8.19 $\pm$ 4.54 nm at 60 min. Yet, it must be considered that the analyzed NPs from 20 min on are remarkably less in number compared to the first time points because of the occuring sintering phenomenon (Table 4.1). At 20 min the size distribution broadens considerably towards larger sizes. The following PSDs, between 30 and 60 min, are much more dispersed with the appearance of significantly enlarged particles up to approximately 25 nm.

Since no small particles are observed in the AFM-measurements and since the quasi-hexagonally ordered pattern is quickly lost through the migration of the particles towards each other, PMC is assumed to be the dominant sintering mechanism for these Pt NPs on crystalline silica. In this case, when two small NPs of 4.19 nm initial mean height coalesce, the sintered particle's radius can be calculated to a size of approximately 5.93 nm. This correlates nicely with the increase in NP mean height to 6.01 nm at 10 min. Also a peak shift in the PSD from below 5 to approximately 6 nm is clearly visible at this time point (Figure 4.2).

4.2.2 Thermally oxidized, amorphous silica SiO_2(ox)

On the amorphous, thermally oxidized silica (Figure 4.3), the hexagonal Pt NP pattern has degraded less than on the crystalline silica (Figure 4.2) after exposure at 750°C for 10 min. The sintering that has taken place at this moment manifests itself as a change in the PSDs, observable as a coarsening of the initially sharp Gaussian-like distribution towards smaller and larger sizes with only a slight change of the number of NPs per unit area. This can be seen by the calculated mean height values and standard deviations obtained in the AFM (Table 4.2). Between 0 min and 10 min, the mean height does not change with 4.03 nm and 4.06 nm, while the standard deviation is more than doubled to 1.84 nm at 10 min compared to 0.81 nm at 0 min. This trend continues further for 20 min with a mean height of 4.17 nm and a standard deviation of 2.60 nm, which can also be seen in the PSD-graph. While the main peak remains below 5 nm, an enhanced tail towards larger particle sizes and a simultaneous existance of very small clusters is detected. However at 20 min, the hexagonal arrangement of the Pt NPs becomes indiscernible in the SEM picture and the NPs visually coarsen significantly. This degradation of the NP structure proceeds during the following time intervals of 30, 45 and 60 min yielding a reduced number of bigger particles.

For the evolution of the NP height, the PSD curves change significantly after 20 min. At 30 min, a bimodal height distribution was observed with one peak remaining below 5 nm and a second peak between 9 and 10 nm, resulting in an increased mean height of 6.84 nm and a standard deviation of more than 4 nm. By 45 min, the AFM graph reveals a very broad size distribution

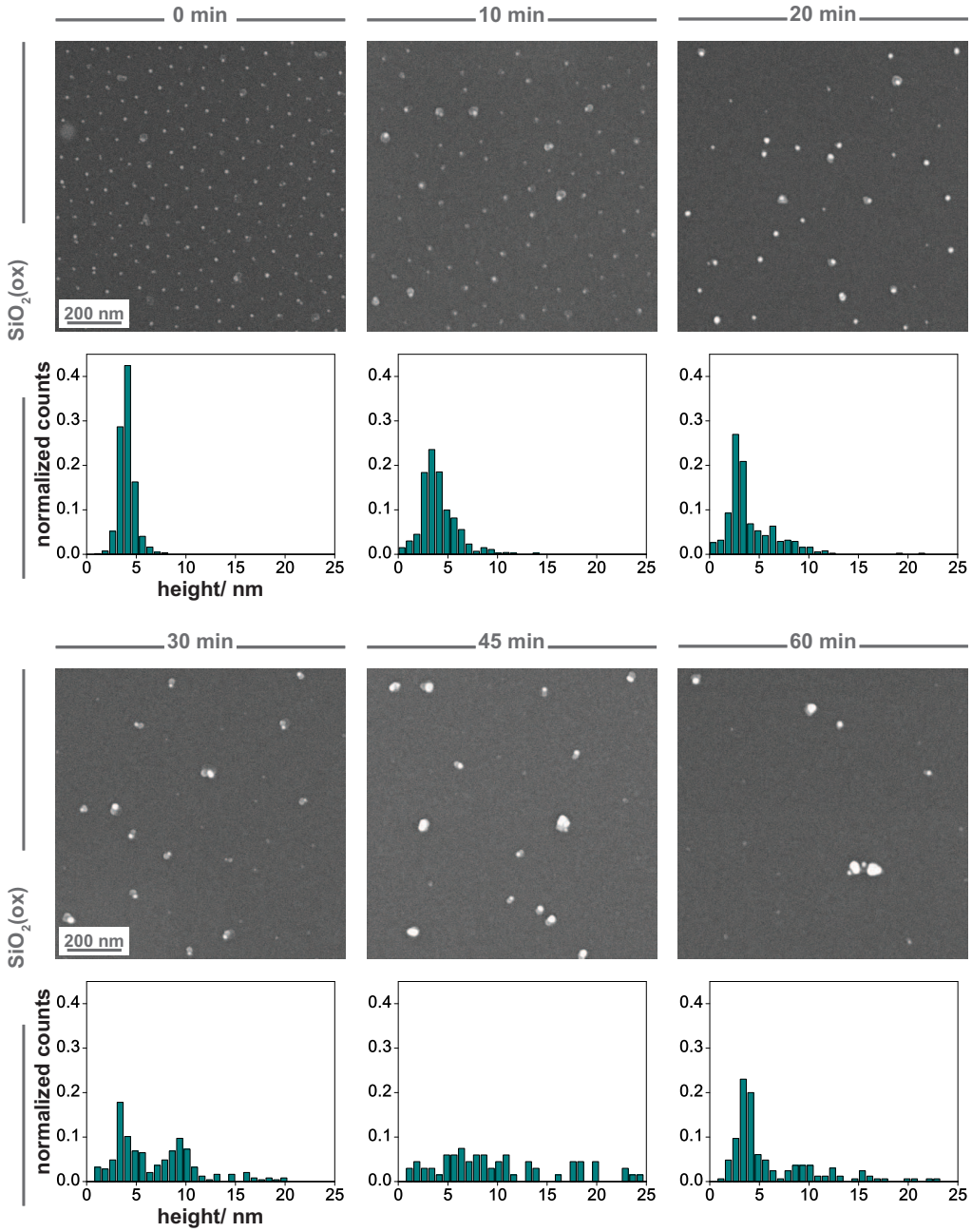

Figure 4.3: SEM images and corresponding PSDs of Pt NPs on SiO_2(ox) during sinter studies in air at 750°C after different time periods. The scale bar in all SEM pictures represents 200 nm.

	0 min	10 min	20 min	30 min	45 min	60 min
mean height	4.03	4.06	4.17	6.84	11.23	6.09
standard deviation	0.81	1.84	2.60	4.07	7.85	4.48
number of NPs	1234	734	378	247	67	165

Table 4.2: Mean heights, standard deviations and the numbers of evaluated NPs extracted from PSDs obtained with AFM for the sintering of Pt NPs on SiO_2(ox).

with NPs up to 25 nm, thus the mean height jumps to a value greater 11 nm. Finally at 60 min, the PSD regains a shape similar to the 20 min-PSD with a single peak below 5 nm again and a tail towards heights of 23 nm. During the Pt NP coarsening on amorphous silica, particles of smaller size than those in the original sample (0 min) were also detected. This leads to the conclusion that the governing sintering mechanism in this case is Ostwald ripening (OR), where adatoms or platinum clusters leave the smaller NPs to attach to larger ones. Additionally, if two particles would coalesce by PMC their radius would change from 4.03 nm at 0 min to approximately 5.7 nm. This phenomenon is not seen in the PSDs since the single peak remains at the sample height value of approximately 4-5 nm and does not shift to higher ones for the first 20 min. Thus, PMC can be ruled out as the dominant sintering mechanism.

This finding agrees with reports about sintering of Pt NPs on amorphous silica by other groups. For example, Larsson *et al.* detected asymmetric, bimodal PSDs with very large NPs using INPS and TEM at 550°C in 4 % O_2/Ar atmosphere and came to the assumption that OR facilitates the thermal coarsening of these 3.3 nm-sized Pt NPs [80]. Similarly, Tabib Zadeh Adibi *et al.* employed TEM to observe 3.0 nm-sized Pt NPs sintering at 500-600°C in the same atmosphere as above on sputtered silica. They saw a progression in the PSDs that began with a single peak distribution and continued via a bimodal distribution back to a single peak distribution. Also, they observed small NPs on all of the samples and concluded OR to be the mechanism behind the sintering. They assume the small NPs to indicate metal redispersion by either (a) trapping these particles due to large interparticle distances or by (b) the formation of Pt oxide, which might interact less with metallic NPs [139]. OR of Pt NPs with the formation of volatile Pt oxide particles has also been reported by Porsgaard and colleagues during thermal treatments of 2 nm and 4 nm-sized Pt NPs on amorphous SiO_2/Si(111) at temperatures above 450°C in XPS [108]. Finally, Simonsen *et al.* used *in situ* TEM to identify OR as the dominant sintering mechanism on amorphous silica-samples after exposure of 1.5 nm Pt NPs to 650°C in synthetic air [127] and Benavidez *et al.* agreed with this by proving that random migration and then coalescence of around 2.5 nm-sized Pt NPs did not occur at 550°C in a 560 Pa oxygen-atmosphere during an environmental TEM study. However, they detected very close-by neighboring NPs to fuse via neck formation and elimination resulting in an anomalous growth pattern with a tail in the PSD towards larger sizes even for the OR sintering mechanism [21].

4.2.3 Crystalline sapphire Al_2O_3(1-102)

On the crystalline alumina, rapid sintering of the Pt NPs can be seen in Figure 4.4. The hexagonal structure is already lost after 10 min and larger particles start to appear, while the number of Pt NPs per unit area decreases significantly. This development continues at the following heating periods coupled with the appearance of a few particles up to even 25 nm. Additionally, shadows around these coarsened bigger particles are seen, indicating the sintering and coalescence of platinum clusters onto them between 10 and 60 min. Simultaneously, the size evolution is indicated by the height graphs obtained in the AFM. Starting with a narrow Gaussian-shaped PSD and a single peak at 4.81 $\pm$ 0.98 nm for the 0 min-sample, the height distributions broaden at the following time intervals. At 10 min, the central peak has moved to a mean size of 6.50 $\pm$ 2.22 nm

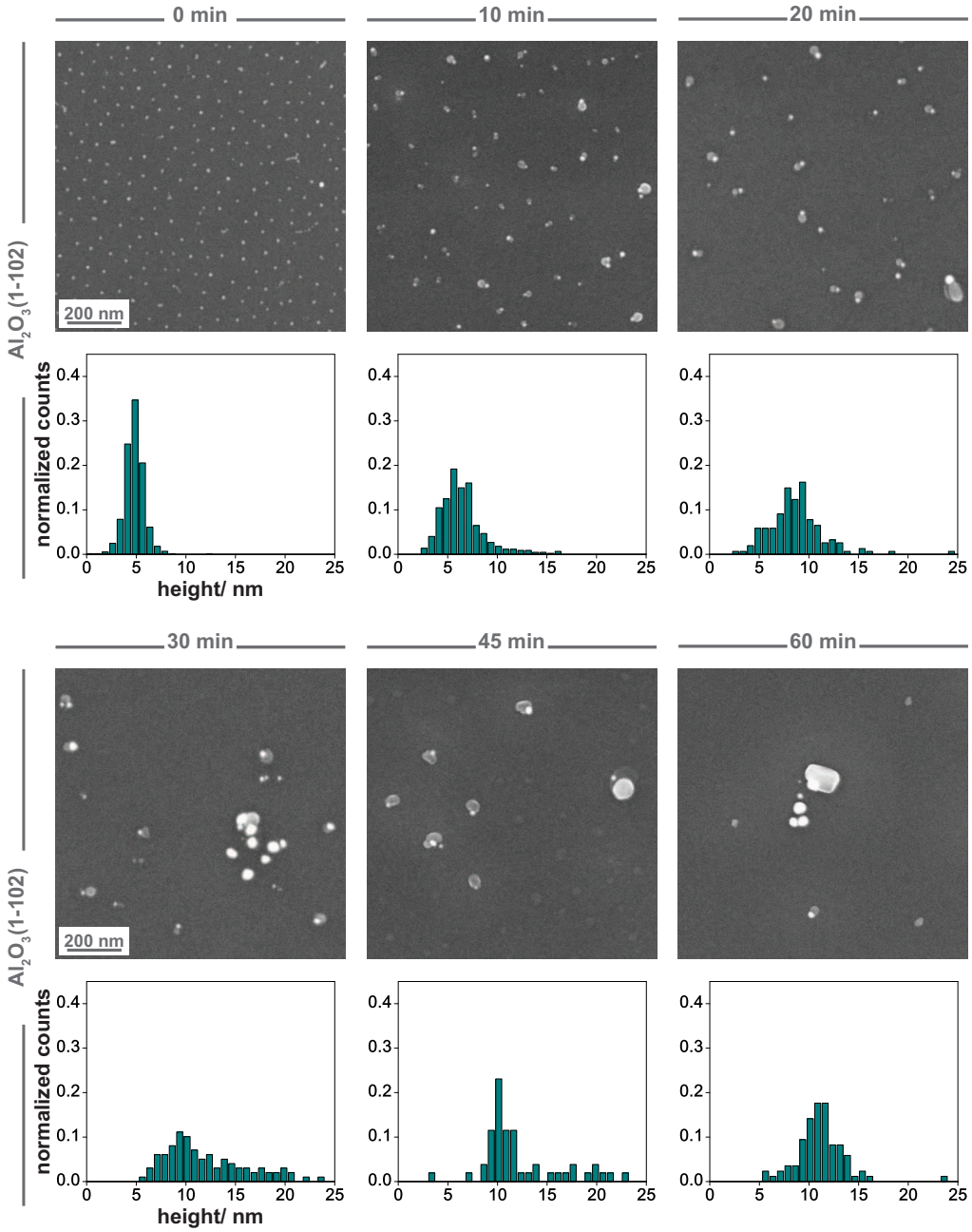

Figure 4.4: SEM images and corresponding PSDs of Pt NPs on Al_2O_3(1-102) during sinter studies in air at 750°C after different time periods. The scale bar in all SEM pictures represents 200 nm.

	0 min	10 min	20 min	30 min	45 min	60 min
mean height	4.81	6.50	8.71	12.68	13.79	11.13
standard deviation	0.98	2.22	2.81	6.23	7.51	2.54
number of NPs	1294	448	154	99	52	85

Table 4.3: Mean heights, standard deviations and the numbers of evaluated NPs extracted from PSDs obtained with AFM for the sintering of Pt NPs on Al_2O_3(1-102).

and a tail towards larger particles with sizes above 15 nm appears. Next at 20 min, the PSD shifts further and centers at 8.71 nm with a standard deviation of 2.81 nm caused by the incidence of large platinum particles up to 25 nm. Then at 30 min, the peak flattens and a very broad distribution with many sintered NPs occurs, pointed out by a mean height of 12.68 nm and a huge standard deviation of more than 6 nm. Continuing at 45 min, particles of less than 8 nm are only rarely detected while large ones are dominant in the PSD. This phenomenon is less pronounced in the final AFM graph at 60 min, which reveals a PSD centered between 11 and 12 nm. Since a decreasing number of NPs is analyzed and evaluated for these mean height and standard deviation values, as well as for the PSD graphs, the results can only be used to give a hint towards the sintering mechanism.

Summarizing, the obtained PSD-graphs for Al_2O_3(1-102) reveal an immediate broadening of the height distributions towards larger sizes and a shift of its center from less than 5 nm towards 11-12 nm, while very small particles cannot be detected at any given time point. Therefore, the migration of whole particles and their coalescence upon meeting as for PMC can be concluded to govern the sintering behavior. In this case, if two individual nanoparticles with an initial 4.8 nm height fuse together the calculated mean size of the resulting particle is approximately 6.8 nm. This correlates nicely with the observed central peak shift for the 10 min-PSD. In agreement, Hejral *et al.* present notable and rapid sintering of Pt stripes with a height of 2 nm on crystalline alumina Al_2O_3(0001) at 277°C, measured with *in situ* high-energy grazing incidence x-ray diffraction and online mass spectrometry [67].

4.2.4 Amorphous alumina Al_2O_3(a)

On the amorphous alumina, the sintering behavior of the Pt NPs is presented in Figure 4.5. Without visible indication of coarsening, the nanoparticles remain in their quasi-hexagonal arrangement for 30 min. Only then, after 45 min a few slightly larger particles appear in the SEM images. This progress is also presented in the corresponding PSDs, obtained with AFM, and its calculated mean height and standard deviation values (Table 4.4). The mean height with a sharp single peak centers at approximately 5 nm for the first two time points at 0 min and 10 min, while only shifting slightly towards 6 nm at 20 min. Yet at 30 min, this peak comes back to below 5 nm, most probably caused by small inaccurancies in the measurements. This shape of the PSD continues with a single peak at around 5 nm for 45 min as well. At later time values however, some larger particles of sizes between 10 and 20 nm arise. Thus, the standard deviation increases to more than 2.5 nm for this heating period. Later at 60 min, the sintering is visible by an agglomeration of a few clustered particles with a height of up to 25 nm in the PSD, while many NPs still remain in their original hexagonal pattern. Thus, the information obtained from SEM and AFM strongly indicates Ostwald ripening to be the prevalent sintering mechanism. None of the PSDs reveal a peak shift of the graphs towards bigger sizes as predicted by the PMC model. If this was the case, the center of the distribution would have evolved from approximately 5 nm towards almost 7 nm.

These findings are in accordance with results by Simonsen *et al.* who showed OR of approximately 3 nm-sized Pt NPs on amorphous alumina at temperatures up to 650°C [125, 126].

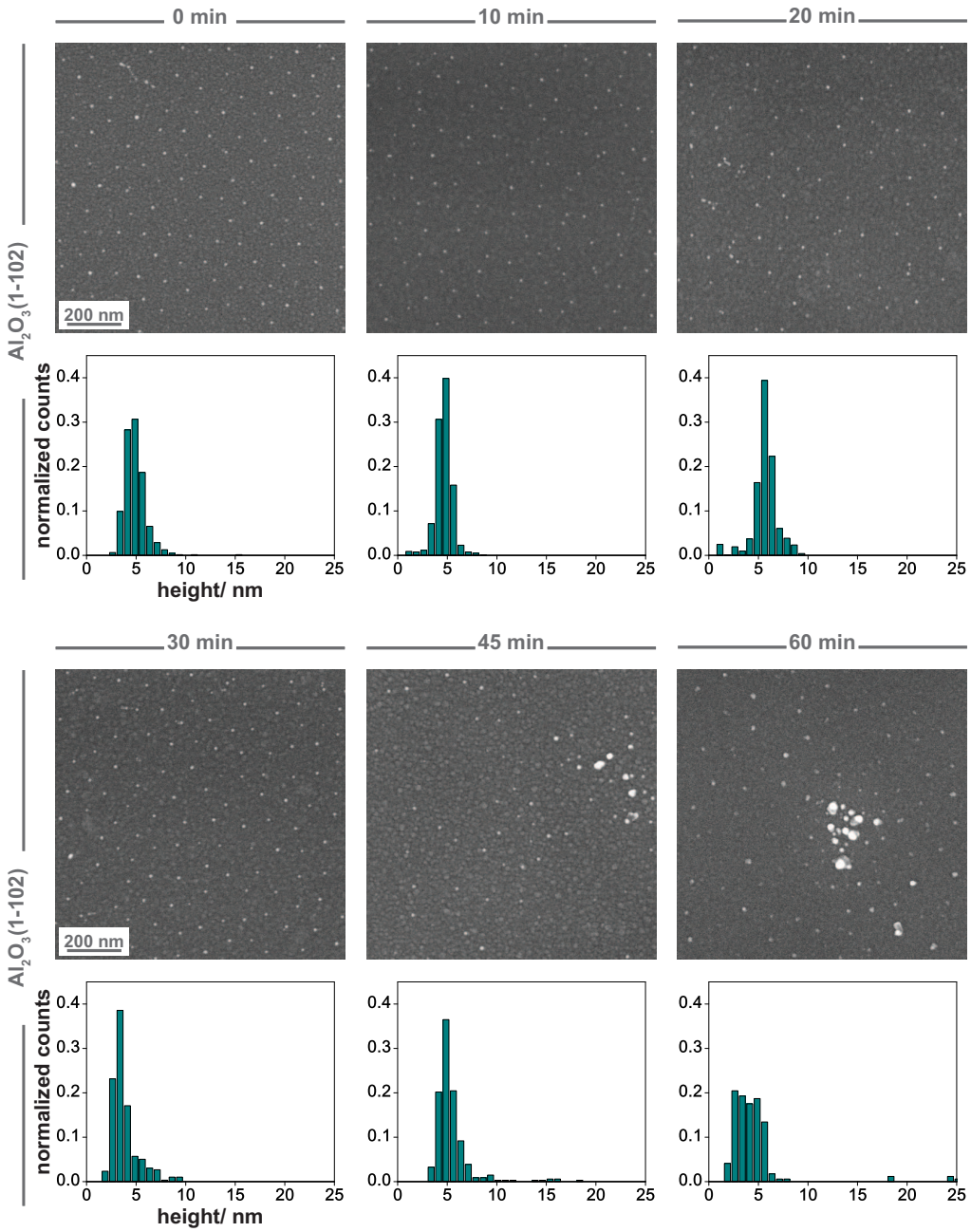

Figure 4.5: SEM images and corresponding PSDs of Pt NPs on $Al_2O_3(a)$ during sinter studies in air at 750°C after different time periods. The scale bar in all SEM pictures represents 200 nm.

	0 min	10 min	20 min	30 min	45 min	60 min
mean height	4.92	4.66	5.64	4.12	5.57	4.67
standard deviation	1.39	0.87	1.30	2.15	2.53	3.83
number of NPs	626	783	726	306	337	171

Table 4.4: Mean heights, standard deviations and the numbers of evaluated NPs extracted from PSDs obtained with AFM for the sintering of Pt NPs on $Al_2O_3(a)$.

Tabib Zadeh Adibi *et al.* also investigated the sintering behavior of 5-6 nm-sized Pt NPs with INPS at 625°C for 10 h in an oxygen-containing atmosphere. During the coarsening of these nanoparticles towards a diameter of approximately 7 to 8 nm, they especially observed the loss of very small particles and thus concluded OR to dominate this phenomenon [137]. Later on, this group presented an enhanced sinter model for OR by a 3D-nanocone-structure of alumina, in which they also detected tiny particles during the thermal treatment at 600°C in 4 % O_2/Ar-gas [138].

Summary of sinter study

In the performed sinter studies at 750°C under atmospheric conditions, Pt NPs coarsen mainly via PMC on the studied crystalline substrates. The PSDs show that the corresponding mean heights, and thus diameters of the nanoparticles evolve towards larger sizes without the evidence of small particles. The Pt NPs behave quite differently on the tested amorphous substrates where OR is the driving mechanism behind the sintering process. On thermally oxidized and amorphous silica, this is manifested in a bimodal distribution of larger particles combined with tiny ones. Pt NPs exhibit significantly higher sinter stability on the amorphous alumina compared to the other three substrates. Larger NPs slowly begin to arise after 45 min without much loss of the hexagonal nanoparticle arrangement. This finding is in agreement with a study by Tabib Zadeh Adibi and coauthors where they applied heat treatments with temperatures up to 600°C in a 4 % O_2/Ar atmosphere. They reported a higher sinter stability of Pt NPs on sputtered alumina compared to sputtered amorphous silica and attributed this higher stabilization to a larger degree of Pt wetting on the alumina [139].

4.3 Parameters influencing sintering behavior

To gain a deeper understanding of Pt NP sintering behavior on the four different investigated substrates, several parameters were analyzed. Thus the adhesion of the nanoparticles to the substrates was measured with LFM, surface roughness was determined in tapping mode-AFM and surface potential of the substrates was obtained with KPFM. Lastly, contact angle measurements revealed disclosure of the surface tension of water on the different supports.

4.3.1 Adhesion of platinum nanoparticles

First, the adhesion of Pt NPs to the different substrates was studied with LFM, which measures the force of friction between the sample and the tip in contact mode [107]. Hereby, the normal force (F_N) is applied to the tip at the cantilever during its horizontal movement across the specimen (Figure 4.6a). Therefore, F_N was adjusted in this experiment. Following a procedure described by Eppler *et al.* [50], an area of 3 µm x 3 µm was scanned with a reduced normal force. As an example, the regular arrangement of the Pt NPs can be seen on crystalline alumina in Figure 4.6b. Then, an increasing F_N was applied onto a smaller area of 1 µm x 1 µm until all Pt NPs were removed. Afterwards, the original area of 3 µm x 3 µm was scanned again with the initial

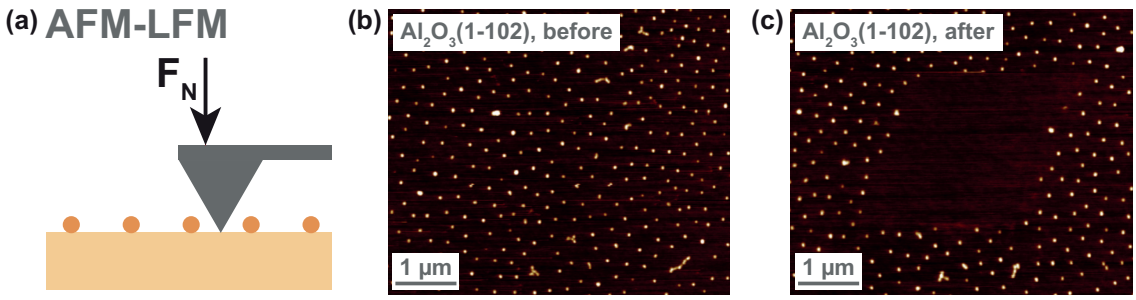

Figure 4.6: (a) Principle of AFM-LFM with the regulation of the normal force F_N applied to the tip to study the adhesion of Pt NPs on different substrates. (b) AFM image of NPs on crystalline Al_2O_3(1-102) as example, measured with reduced F_N. (c) Scan area after applying higher F_N to remove NPs.

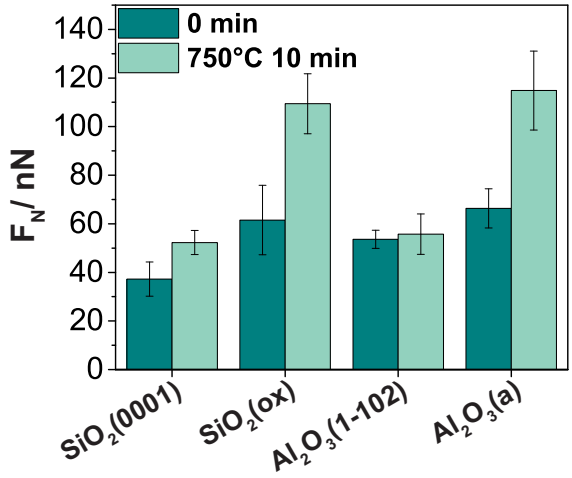

Figure 4.7: Comparison of measured F_N to study Pt NP adhesion on different substrates.

normal force (Figure 4.6c) to verify the complete removal of the NPs. Further AFM images of the adhesion study with LFM are presented in Figure A.1 in Appendix A.

The obtained F_N-values needed to remove the Pt NPs from the alumina and silica substrates before and after heat treatment at 750°C for 10 min are shown in Figure 4.7. For the samples that were not thermally treated (0 min) the resulting normal force needed to remove all of the Pt NPs was generally slightly lower on the crystalline substrates than on the amorphous substrates pertaining for both silica and alumina. Crystalline silica and alumina required normal forces of 37.2 $\pm$ 7.0 nN and 53.6 $\pm$ 3.7 nN respectively compared to 52.3 $\pm$ 5.0 nN and 66.3 $\pm$ 8.1 nN for the amorphous supports. Hereby, the lowest adhesion of the NPs is seen on the crystalline silica-substrate. Treatment at 750°C for 10 min only caused a minor difference in the measured F_N-value for the crystalline alumina with an increase of approximately 2 nN to 55.7 $\pm$ 8.3 nN. On the crystalline silica-substrate a higher F_N-value was obtained with 61.5 $\pm$ 14.3 nN, which is still very comparable to the 0 min-datapoints of all other samples. However, a drastic change was found for the NP adhesion on the amorphous supports during the heat treatment, which was reflected in significantly higher F_N-values. Both amorphous silica and alumina required F_N-values of 109.4 $\pm$ 12.3 nN and 114.8 $\pm$ 16.3 nN to remove the NPs and thus show an almost two-fold gain

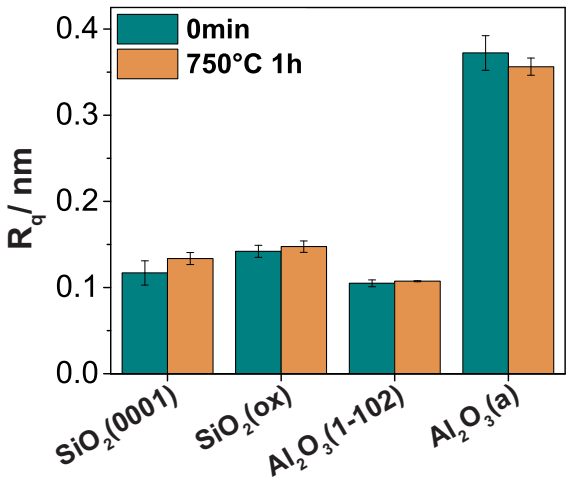

Figure 4.8: Surface roughness (R_q), obtained via AFM, of silica and alumina substrates before and after sintering in air at 750°C for 1 h.

in F_N. Though all small nanoparticles could be scraped off of the amorphous surfaces, some larger sintered particles that had formed during the 10 min oven treatment could not be removed with the AFM, as seen in Figure A.1 in Appendix A on the amorphous silica-sample. Such an increase in F_N of approximately 50 nN for nanoparticle removal has also been reported for these two substrates [50, 146]. As underlying reasons, Eppler *et al.* assumed that a Pt silicide formation is involved [50], whereas Tsirlin *et al.* explained it as a function of increased interaction between the Pt NPs and the alumina substrate [146]. By correlating sintering and adhesion properties of Pt NPs on crystalline and amorphous silica and alumina it becomes evident that NPs adhere more strongly to amorphous substrates, especially after heat treatment. Overall, NPs sinter less on amorphous substrates than on crystalline ones. The mechanism by which they sinter on amorphous supports is dominated by Ostwald ripening, whereas on crystalline substrates NPs sinter through PMC. Thus, it can be concluded that stronger adhesion contributes to Ostwald ripening by increasing Pt NP immobilization. The adhesion of the NPs to the substrates plays a role in the sintering kinetics of Pt NPs on the four tested substrates.

4.3.2 Substrate roughness

As a second parameter, the roughness of these different substrates was studied with AFM to evaluate its influence on the Pt NP sintering. Height information of the substrates was obtained by slow scans in tapping mode. The resulting image root mean squared roughness parameter (R_q), defined as the root mean square average of height deviations, is used to make a statement on the surface roughness. The measured roughness values were determined on samples before and after 1 h heat treatment at 750°C and are displayed in Figure 4.8. At 0 min, crystalline and amorphous silica, as well as crystalline alumina all displayed very similar R_q-values and maximum vertical distances between the highest and lowest surface points with R_q equivalent being 0.117 ± 0.014 nm, 0.142 ± 0.007 nm and 0.105 ± 0.004 nm correspondingly. Also, during the heat treatment at 750°C for 1 h, the measured values changed only slightly to 0.134 ± 0.007 for SiO_2(0001), 0.148 ± 0.007 nm for SiO_2(ox) and 0.107 ± 0.001 nm for Al_2O_3(1-102). In stark

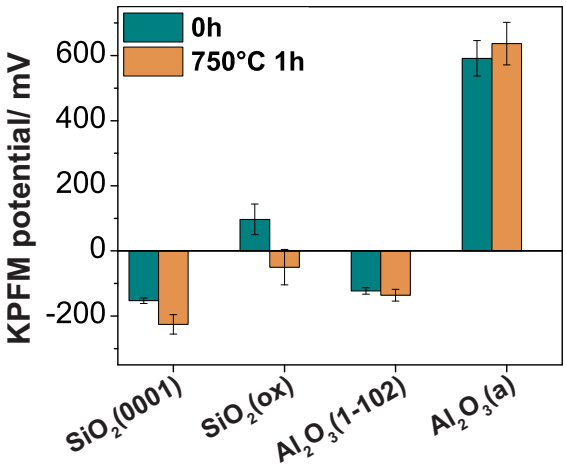

Figure 4.9: KPFM-study with a Pt-Ir tip on silica and alumina before and after sintering in air at 750°C for 1 h.

contrast, the amorphous alumina substrates were characterized by significantly greater roughness of 0.372 ± 0.020 nm before and 0.356 ± 0.010 nm after the heat treatment. Generally, for all substrates no morphological surface alterations became evident during the entire hour of the heat treatment. Due to the sputtered, thick amorphous 100 nm-layer, the roughness on the Al_2O_3(a)-support is almost three-fold greater than on all other tested surfaces.

Since the sintering rate is considerably reduced on the amorphous alumina, it can be concluded that surface roughness is one parameter that obviously contributes to Pt NP sinter stability. This emphasizes the fact that substrate height heterogeneities play a more important role in Pt NP sintering than adhesion, which increased on both amorphous silica and alumina substrates.

4.3.3 Surface potential study with Kelvin probe force microscopy

The surface potential was measured with AFM-based amplitude modulation (AM-) KPFM, which is useful for detecting the contact potential difference between a tip and a sample. Thus, the work function as well as the surface potential can be obtained [102]. Typically used for metals or semiconductors, Ludeke *et al.* also applied the KPFM-technique to oxides such as silica and alumina layers [88]. Accordingly, the here measured V_{CPD}-values between the used Pt-Ir tip and the samples before and after 1 h at 750°C are depicted in Figure 4.9. These were -153.0 ± 8.3 mV and -122.8 ± 9.9 mV for the crystalline silica and alumina-samples before the heat treatment. During the 1 h-time interval at 750°C, the values changed insignficantly to -225.7 ± 30.0 mV and -136.0 ± 17.9 mV respectively, so this exposure to high temperatures does not effect the surface potential of these substrates. Due to high measurement inaccuracies on isolating oxide-samples, standard deviations of ± 100 mV can be neglected. Hence the two tested crystalline supports revealed very similar potentials. Additionally, for the amorphous silica-samples surface potentials of 97.0 ± 47.1 mV before and -50.1 ± 54.4 mV after the oven procedure at 750°C were gained. While these values are higher compared to the crystalline substrates, they do not show a significant rise. Thus, all the measured potentials on crystalline and amorphous silica, as well as

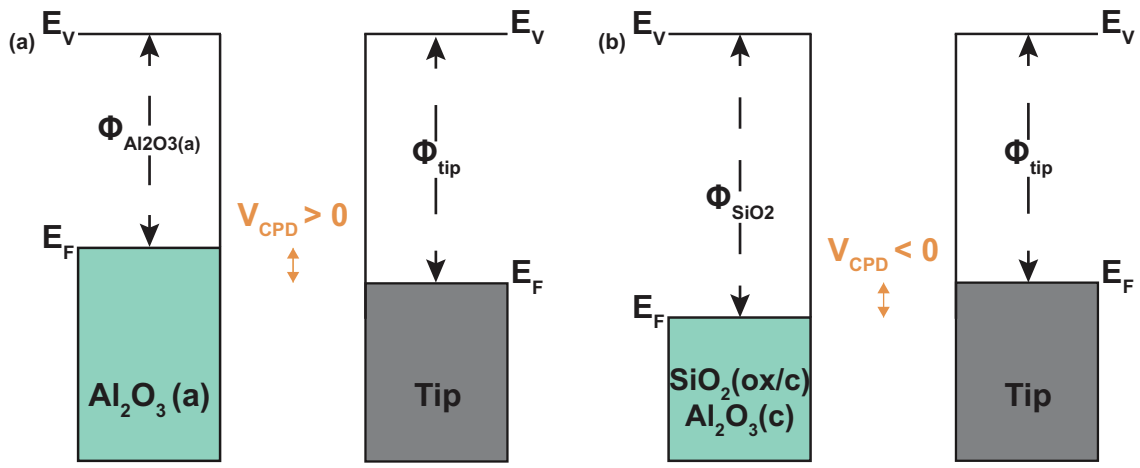

Figure 4.10: Illustration of energy diagrams for the measured (a) amorphous Al_2O_3(a)- or (b) crystalline and amorphous SiO_2(ox/c)- and crystalline Al_2O_3(c)-samples. E_V represents the vacuum energy level, E_F the Fermi energy level and Φ the corresponding work functions of the tip and samples. In the case of (a) amorphous alumina, a positive bias voltage (V_{CPD}), and in the case of (b) the other substrates, a negative V_{CPD} is measured in order to nullify the CPD.

crystalline alumina are comparable, ranging between -200 mV and +100 mV. In stark contrast, a considerably higher surface potential – more than 500 mV above the values of the other surfaces – was obtained on amorphous alumina. Hereby, the values reached 591.6 $\pm$ 54.3 mV before and 636.9 $\pm$ 65.2 mV after the heat treatment. Again, the high temperatures of 750°C in the oven do not seem to considerably change the surface potential of the substrates. Yet, the major rise between maximum 100 mV for amorphous silica and 600 mV for the amorphous alumina reflects a significant surface potential difference between the tested samples.

The matching work functions Φ_{sample} for these materials can be calculated by the converted form of equation 2.2

$$\Phi_{sample} = \Phi_{tip} + e \cdot V.$$

The work function of the tip Φ_{tip} was determined by performing reference measurements on chromium and nickel. Thus, the work function of amorphous alumina is calculated to be 4.8 eV, whereas the other three substrates – crystalline and amorphous silica, as well as crystalline alumina – have work functions ranging from 5.5 eV to 5.7 eV. Illustrating and explaining this work function difference with the help of energy diagrams, Figure 4.10a shows the higher surface potential of the amorphous alumina substrate in contrast to the other supports as in Figure 4.10b. As a result of this higher potential the electrons on the surface of amorphous alumina need less energy to leave the substrate from their Fermi energy level E_F to reach the vacuum energy level E_V, resulting in a higher reactivity. Also considering the stronger adhesion of the Pt NPs on the amorphous alumina substrate during the LFM-measurements, the formation of a bond between these two materials seems likely.

In conclusion, a high surface potential, as seen on the amorphous alumina-support, is one of the factors contributing to a decrease in the Pt NP sintering at high temperatures.

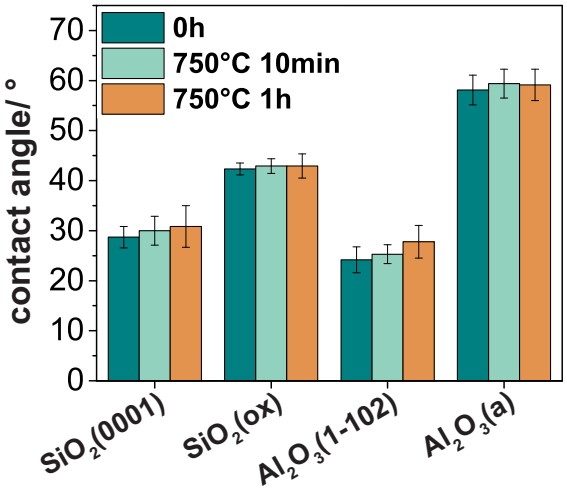

Figure 4.11: Contact angles of water on crystalline and amorphous silica and alumina before (0 h) and after heat treatment for 10 min and 1 h at 750°C.

4.3.4 Surface energy via contact angle measurements

As a last parameter, the contact angle of water was measured on amorphous and crystalline silica, as well as alumina. Figure 4.11 presents the obtained contact angles for the different substrates before and after a 10 min and 1 h-heat treatment at 750°C. For crystalline silica, angles of 28.7 $\pm$ 2.1°, 30.0 $\pm$ 2.9° and 30.8 $\pm$ 4.2° and for crystalline alumina, angles of 24.2 $\pm$ 2.6°, 25.4 $\pm$ 1.9° and 27.8 $\pm$ 3.3° were detected for 0 h, 10 min and 1 h at 750°C respectively. However on amorphous silica, the contact angle increased to 42.3 $\pm$ 1.2°, 42.9 $\pm$ 1.5° and 42.9 $\pm$ 2.4°, thus revealing a considerably more hydrophobic behavior of the water drop on this support compared to the two crystalline substrates. Lastly, the contact angles showed higher values by more than 15° for the amorphous alumina with 58.1 $\pm$ 3.0°, 59.4 $\pm$ 2.9° and 59.1 $\pm$ 3.1°. Hereby, the water wets significantly less on these lastly tested substrate compared to the other ones. Overall, the heat treatment does not effect the contact angles of water on these substrates. Yet, since the interfacial tension between the water drop and the substrate, as well as the surface energy of the substrate in air are unknown, the surface energy of the underlying support cannot be calculated (see Equation 2.8 in chapter 2.2.4). But the overall trend of the water contact angles on crystalline, as well as amorphous silica and alumina correlates very well with the observed sintering of Pt NPs on these supports. A higher contact angle refers to a less pronounced sintering through the Ostwald ripening process, while very low contact angles as seen on the two crystalline substrates refer to rapid Pt NP-coarsening via the PMC-mechanism. The enhanced wetting of water on the crystalline substrates could relate to a more distinct wetting of platinum and therefore a higher surface diffusion of whole Pt NPs on these latter supports. The shadows seen on the crystalline alumina and silica during the above sinter studies (Figure 4.2 and 4.4) strongly support this thesis.

4.4 Sintering of platinum nanoparticles on dual-structured substrates with silica and alumina

The sintering behavior of Pt NPs at the interface between two amorphous materials, silica and alumina, was studied using dual-structured substrates comprising both an alumina- and a silica-section. The particles were immobilized on one of the two materials and then heated to 750°C for different time intervals. Via SEM combined with energy dispersive X-ray spectroscopy (EDX) the sintering was characterized and platinum was identified in the grown particles.

4.4.1 Platinum nanoparticles on SiO_2(a) interfacing particle-free Al_2O_3(a)

For the first sinter study, Pt NPs were placed on the amorphous silica SiO_2(a)-side of the dual surface substrate comprising silica and amorphous alumina, Al_2O_3(a). Their thermal behavior was studied over a time period of 90 min and the resulting SEM images are presented in Figure 4.12a. As it can be seen, the initial regularly arranged Pt NPs at 0 min begin to sinter quickly by loosing their quasi-hexagonal pattern and larger agglomerated particles can be detected after 15 min. This behavior is identical to the one which was observed on the single surface amorphous silica samples shown in Figure 4.3. Sintered NPs up to 60 nm were observed in TEM images (Figure 4.13). These larger particles occur most frequently at the approximately 50 nm high border towards the amorphous alumina. The preferred migration and clustering of Pt NPs in the direction of this interface, where they are more sinter stable, is attributable to the existence of an Ehrlich-Schwoebel barrier, which is theoretically introduced in chapter 3.1 and a schematic illustration of this barrier is shown in Figure 3.4. At this barrier an additional potential needs to be overcome by the NPs to enable them to cross over the border towards alumina [48, 120]. Thus, the barrier slows down nanoparticle migration with the local accumulation of sintered Pt NPs. Yet, those Pt NPs that were initially situated far away from this boundary are not affected. After 30 min, some Pt NPs can be discovered on the amorphous alumina. By detecting backscattered electrons in the SEM, material contrast caused by different atomic numbers of the imaged elements can be made visible. With the ESB-detector, heavier materials like platinum - recognizable by their brighter intensity - can be distinguished from the substrates with lighter elements, such as Al, Si, and O in alumina and silica [3]. This trend of accumulated sintered Pt NPs on the silica-section at the interface towards amorphous alumina continues through the 60 min-time point. And lastly, at 90 min, NPs migrating onto the amorphous alumina were observed at and right behind the border of silica to alumina. Using EDX on these 90 min-samples proves that the bright spots on the amorphous alumina are Pt NPs. In the EDX spectra of Figure 4.14, the measured local points are confirmed to contain platinum by showing a platinum peak at 2.049 keV.

The sintering behavior of these Pt NPs was also observed in comparison to control samples, as shown in Figure B.1a in Appendix B. For these samples, dual-structured amorphous silica-alumina-substrates were fabricated without depositing Pt NPs onto them. During a sinter study over the time interval of 120 min, no migrating bright spots and no platinum could be detected anywhere. Our observations support the hypothesis that, due to thermodynamic reasons, noble

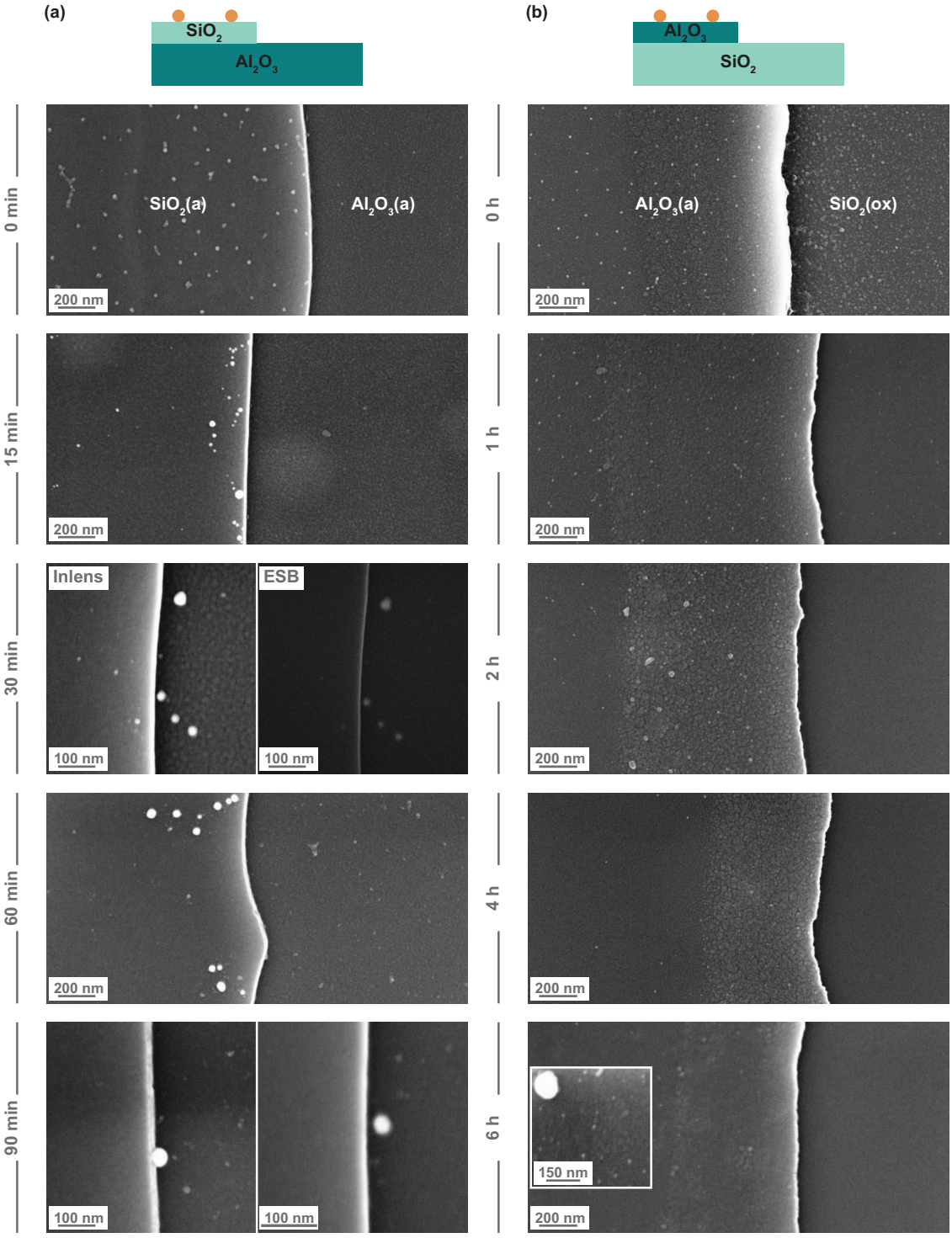

Figure 4.12: SEM images of Pt NPs on dual-structured amorphous silica-alumina-substrates. (a) Pt NPs immobilized on the amorphous silica-side and (b) Pt NPs immobilized on the amorphous alumina-side during sinter studies in air at 750°C. For all SEM images, the Inlens-mode was used to show topographic information. Only for the 30 min-sample in (a), the ESB detector helped to distinguish the heavier element Pt from the lighter substrate elements and thus, the NPs could be identified as Pt NPs.

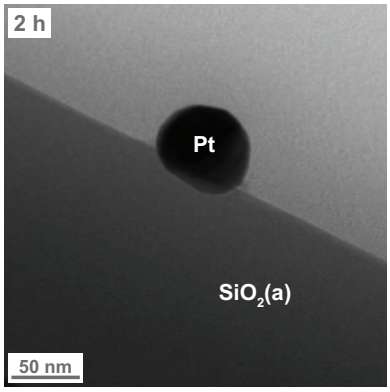

Figure 4.13: TEM image of a sintered, 55-60 nm sized Pt NP on amorphous silica SiO_2(a) after a 2 h-heat treatment at 750°C.

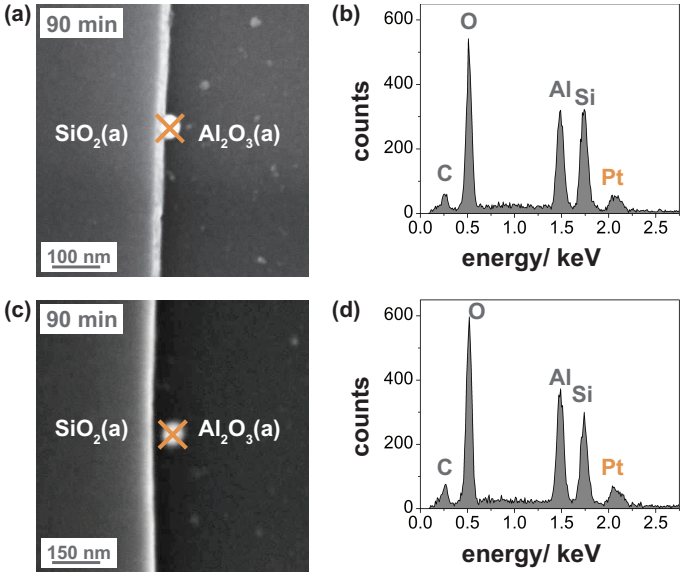

Figure 4.14: (a) and (c) SEM images of Pt NPs migrating from the amorphous silica SiO_2(a)-section onto the amorphous alumina Al_2O_3(a)-side, with the corresponding (b) and (d) EDX spectra to verify it is platinum. Pt peak can be identified at 2.049 keV.

metal nanoparticles do not to stay on rather low metal interaction domains, which in this case is the amorphous silica-side. Instead, they partially migrate onto high metal interaction domains, such as the amorphous alumina with its high surface potential. This sintering behavior is schematically illustrated and summarized in Figure 4.16a.

4.4.2 Platinum nanoparticles on Al_2O_3(a) interfacing particle-free SiO_2(ox)

In a second experiment, the Pt NPs were placed on the amorphous alumina Al_2O_3(a)-side of the dual surface substrate and their thermal behavior was studied over a time period of 6 h. The result of this sinter study is shown in Figure 4.12b. The choice of longer time intervals to observe NP growth during sintering on amorphous alumina is related to the increased sinter stability demonstrated in the individual substrate study in Figure 4.5. Comparable with the above described Pt NPs on the silica-section (Figure 4.12a), the particles are well arranged in their hexagonal pattern at 0 min on the Al_2O_3(a) (Figure 4.12b). The hereby observed coarse silica

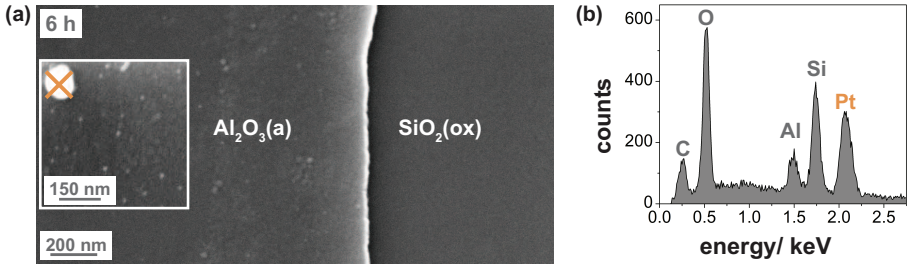

Figure 4.15: (a) SEM image of sintered Pt NP on amorphous alumina Al_2O_3(a), with the corresponding (b) EDX spectrum to verify it is platinum. Pt peak can be identified at an energy of 2.049 keV.

layer on the 0 min-sample is caused by an incomplete removal of the resist. This phenomenon also occured on the reference 0 min-sample without Pt NPs, as shown in Figure B.1b in Appendix B, which looks very similar. Due to their high sinter stability, the Pt NPs remain in their original structure for the first 1 h. After about 2 h at 750°C, the original hexagonal pattern of the NPs starts to disintegrate as NPs migrate away from the border facing the amorphous silica SiO_2(ox). As expected, the NPs sinter more slowly in those areas of the amorphous alumina that are more distant from the border than those very close to it. At the interface the samples also show a slightly changed morphology which is probably caused by the removal of the resist through sonication. This evolution continues in the 4 h-sample with only a few small particles being left in the region close to the barrier towards silica. Furthermore, after exposure at 750°C for 6 h, no small Pt NPs were observed anymore on the alumina near the interface border. However, few large NPs were found on the alumina. These could be identified as platinum particles using EDX (Figure 4.15). The platinum peak in the EDX spectrum is detected at the reported 2.049 keV-energy mark. Yet, none of the coarsened sintered Pt NPs were found on the silica.

The sintering behavior of the Pt NPs was verified using control samples, which are presented in Figure B.1b in Appendix B. Again, the substrates exhibited no morphological changes that could interfere with the sintering behavior of Pt NPs on these supports. Additionally, both the diffusion of aluminum ions into silica as well as the diffusion of silicon ions into alumina could be ruled out by EDX measurements.

Pt NPs sinter much faster on amorphous silica compared to alumina, and preferably migrate into close proximity of the interface (Figure 4.16a). On the contrary, Pt NPs on alumina sinter at a much slower rate and remain on the alumina-side with no visible preferred migration towards the interface to the silica (Figure 4.16b). This suggests that Pt NPs prefer to localize on or as near as possible to the alumina surface, most likely due to its enhanced sinter stability properties.

4.5 Summary

The sintering behavior of Pt NPs on crystalline and amorphous silica and alumina was studied under atmospheric conditions at 750°C. Fast coarsening of the NPs to large particles and the quick loss of their original quasi-hexagonal pattern suggests PMC to be the dominant sintering mechanism on the crystalline substrates. In contrast, Pt NPs on the amorphous substrates

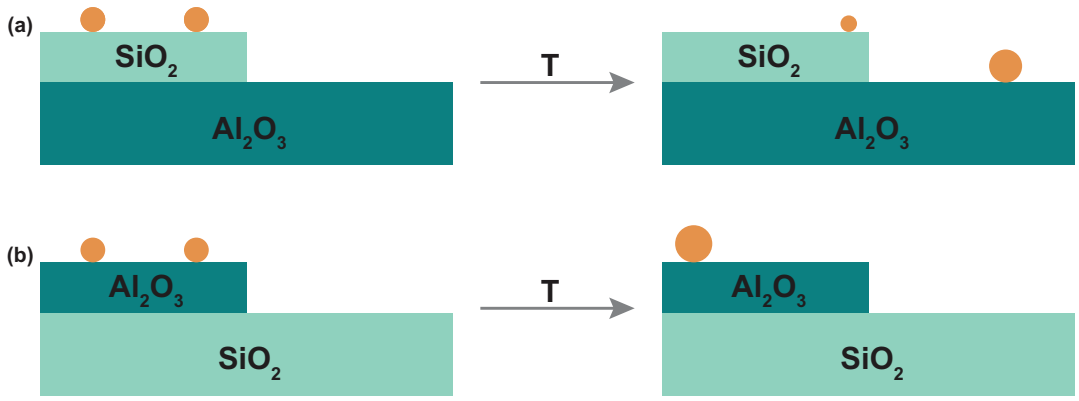

Figure 4.16: Scheme summarizing the sintering behavior of Pt NPs on structured amorphous silica- and alumina-samples. (a) Pt NPs placed on amorphous silica preferably migrate to the interface towards alumina, and some sintered Pt NPs can be detected on the alumina-side after thermal treatment at 750°C. (b) Pt NPs placed on amorphous alumina stay and sinter on the alumina-section, without migrating over to the amorphous silica-side.

remain in their original hexagonal arrangement for longer and very small particles appear over time, suggesting that Ostwald ripening governs this sintering behavior. The comparison of amorphous silica and amorphous alumina reveals that NPs coarsen much faster on amorphous silica. Amorphous alumina displays by far the highest sinter stability.

Pt NPs surface adhesion, substrate roughness, surface potential and energy were analyzed and their influence on sintering behavior was examined. The Pt NPs adhere much more strongly to the amorphous substrates than to the crystalline supports, especially after heat treatment at 750°C for 10 min. In this case, an almost twofold increase in nanoparticle adhesion was detected on the amorphous silica and alumina supports. Thus, stronger adhesion tends to slow down the sintering by impacting the Ostwald ripening process through an advanced Pt NP immobilization. Yet, one primary contributing factor impacting the thermal stability of the nanoparticles is the surface roughness of the amorphous alumina, which is approximately three times greater compared to crystalline alumina and the two tested silica-samples. Hereby, more pronounced substrate height heterogeneities on the amorphous alumina reduce the sintering more than an increased NP adhesion, which was enhanced on both amorphous supports. Additionally, the surface potential of the substrates was investigated with KPFM and amorphous alumina was found to have a considerably higher potential than all the other substrates. This suggests the surface potential of the underlying substrate to be another important factor contributing to the improved sinter stability of Pt NPs on this support. Because amorphous alumina exhibits an increased reactivity, a bond formation between the Pt NPs and the amorphous alumina is hypothesized to take place. Lastly, the contact angles of water on the tested substrates correlate very well with the observed sintering behavior of the Pt NPs. A higher contact angle, thus a lower wetting of water on the substrate, reveals an increased Pt NP sinter stability. This is possibly caused by a reduced Pt NP flattening and therefore, less profound surface diffusion of platinum clusters as detected on the amorphous substrates with OR as dominant sintering mechanism. In sum, the increased surface roughness and the higher surface potential of the substrate underneath the catalytically active

Pt NPs are two dominant factors for governing their sintering behavior, while NP adhesion and surface energy of the support play an important role for the sintering mechanism.

After classifying some important parameters, the performance of Pt NPs on dual-structured substrates containing an amorphous silica- and an amorphous alumina-side was investigated during heat treatments at 750°C, with specific interest in the behavior at the interface between these two materials. NPs situated on the silica-section were generally quicker to grow into larger particles and also showed directional migration towards the interface, which acts as an Ehrlich-Schwoebel barrier. Thus, sintered nanoparticles tend to accumulate at the border towards amorphous alumina. As time progressed, Pt NPs also crossed over it and could be detected on the alumina-section of these samples. EDX and ESB exclusively identified platinum in the migrated nanoparticles. On the other hand, when Pt NPs were placed on amorphous alumina of increased sinter stability and with an interface towards amorphous silica, the NPs remained unaltered until much later time points. In general, Pt NPs immobilized on alumina coarsen much slower. No diffused NPs on the silica-side could be detected at any time with the NPs remaining on the alumina-section. In sum, it appears that Pt NPs favor the high metal interaction alumina substrate with its properties concerning advanced sinter resistivity over the low metal interaction silica substrate.

5 Sintering of platinum nanoparticles on tilted sapphire wafers

In chapter 4, Pt NP sintering was studied on crystalline and amorphous silica and alumina substrates while examining the impact of substrate properties on the sintering behavior. In contrast, this chapter will investigate nanoparticle coarsening on sapphire wafers, Al_2O_3(c), with different tilt angles. Hereby, the surface structuring was performed on the same substrate material excluding the impact of different chemical compositions. Alumina was chosen due to its common application in car converters for exhaust combustion [20]. The structuring was obtained by varying the tilt angle of the sapphire wafers between 0.1° and 15°. This yielded surface heterogeneities in the lower nanometer range of maximum 15 nm. During sinter studies in air and under vacuum, the influence of nanometer-sized surface structuring on the Pt NP's thermal stability was analyzed. Hereby, the focus was placed on whether the step edges act as Ehrlich-Schwoebel (ES) barriers, thus hindering the diffusion of platinum clusters.

5.1 Analysis of tilted sapphire wafers

Nowadays, sapphire as a multifunctional material with its advantages of inertness and superior thermal and mechanical stability is used for diverse engineering purposes in addition to its implementation for catalytic functions. These include the application as substrates for the growth of epitaxial semiconductor films, such as silicon or gallium nitride or for the fabrication of integrated circuits and aligned single-walled carbon nanotubes [46, 90, 40, 63]. Hereby, during the chemical vapor deposition of gallium nitride, the lattice parameters of the latter and sapphire do not completely match depending on the use of *r*-plane (1-102) or *c*-plane (0001) sapphire, yielding diverse dislocation densities in the gallium nitride layer and thus it influences the resulting layer-quality [90, 40]. In the past couple of years, tilting the sapphire substrate has been studied with its influence for the epitaxial growth of such layers [104].

In this thesis, *c*-plane (0001) Al_2O_3-wafers with tilting angles of 0.1°, 4°, 9° and 15° towards the *r*-plane (1-102) have been used, as illustrated in Figure 5.1. It is of interest if the nanoparticles show deviations in their sintering behavior depending on the exposed (0001)-lattice edges. Through an extensive cleaning procedure with acetone, an oxygen plasma and peroxymonosulfuric acid, as well as a heat treatment at 1400°C for 24 h, the amorphous layer was removed on the tilted substrates and the step edges were observed in AFM. The resulting height profiles, which were obtained within the framework of an internship by master student Sarah Young, B.Sc. under my superivision, are shown in Figure 5.2.

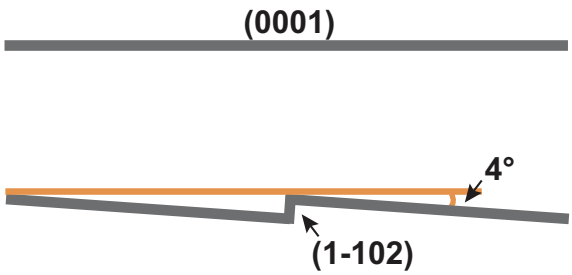

Figure 5.1: Scheme of 4°-tilted Al_2O_3(c)-wafer.

The 0.1°-tilted sapphire substrates reveal regular lattice edges on a height scale in the picometer range. As seen in Figure 5.3a, the average step height is 0.26 ± 0.04 nm and the step size is around 344.67 ± 43.10 nm (Figure 5.3b). Thus, the 5-6 nm sized Pt NPs for the sinter study, which show heights ranging between 4 and 5 nm in AFM-measurements, are much larger compared to the step height of these 0.1°-tilted wafers, serving as a reference later on. Also, the step size should not influence the sintering behavior of the Pt NPs with a size more than 60-times the nanoparticle's diameter and approximately 3-times the interparticle distance between the particles of 80 to 120 nm. When comparing this "flat" substrate with the small 0.1°-angle to the other tilted wafers while keeping a constant height scale from +13.5 nm to -14.2 nm, as shown in Figure 5.2 on the right side, the step edges are hardly visible.

Secondly, in Figure 5.2 on the left side, the step edges of the 4°-tilted sapphire substrates are imaged via AFM and are displayed with a height scale of +3.5 nm to -3.7 nm. Their mean step height is measured to be 3.56 ± 0.92 nm, while their step size is 50.37 ± 12.40 nm (Figure 5.3a and b). For these wafers, the step size has decreased significantly to a seventh of the 0.1°-tilted ones and so very close edges are appearant. In the 3D-view of Figure 5.2, the edges are clearly observable when comparing all substrates with each other on a constant height scale. In this case, the 5-6 nm sized NPs are a little bit larger than the step heights, yet are in their size range. Thus the NPs to are hypothesized to notice the (0001)-lattice edges. Additionally, with an approximate interparticle distance of 80-120 nm, only one individual NP is supposed to be on a step from a vertical viewpoint due to the decreased step sizes.

As third substrates, sapphire wafers with 9°-tilting angles are examined and their height profile is presented in Figure 5.2 with an individual height scale of +5.6 nm to -6.2 nm on the left side and in a 3D-view with the constant height scale for comparison on the right side. Here, the lattice plane edges are even closer to each other than on the 4°-wafers and reveal a step size of 33.67 ± 15.56 nm (Figure 5.3b). Thus again as with the 4°-substrates, each NP with a large interparticle distance of around 100 nm is separately placed on a step when viewed perpendicular to it. The step height of the 9°-tilted sapphires increases to 4.06 ± 1.18 nm (Figure 5.3a), which is comparable to the Pt NP height in AFM of 4-5 nm (as for example in Figure 4.2). This nanoparticle size is slightly lower than the TEM-determined diameter of 5-6 nm for the NPs due to wetting and flattening of the nanoparticles on the substrate.

Lastly, the 15°-tilted substrates result in a disparate AFM height image than the 4° and 9° ones. They reveal an increased step size with 110 ± 34.75 nm while not following the trend of smaller steps for larger tilting angles (Figure 5.3b), which is also seen in the AFM 1D- and 3D-images

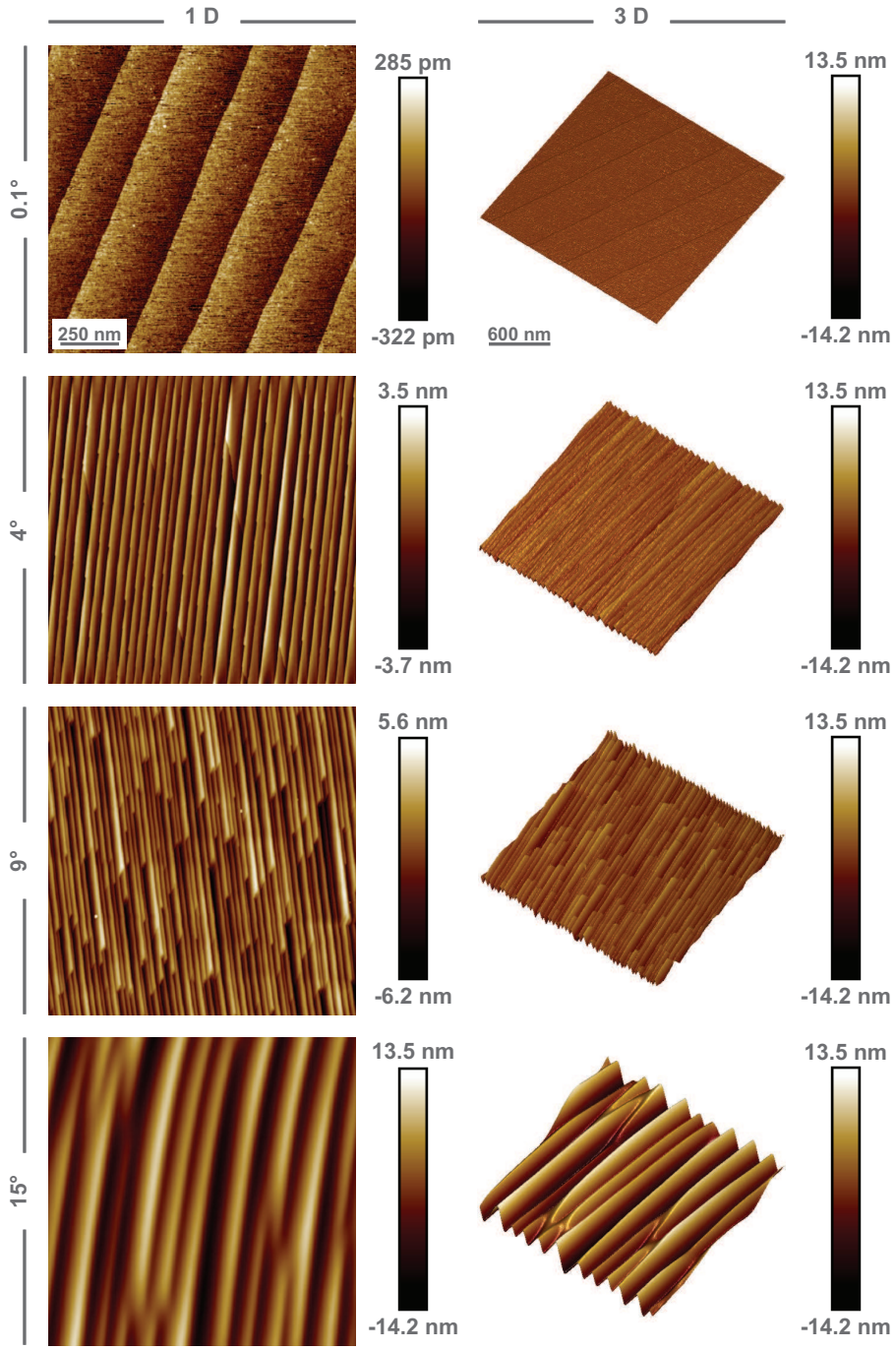

Figure 5.2: Height profiles of 0.1°, 4°, 9° and 15°-tilted Al_2O_3(0001)-wafers by AFM. On the left side (1D), the height scale is individually adapted showing finer structures, while on the right side, the substrates are compared in a 3D-view with a consistent height scale.

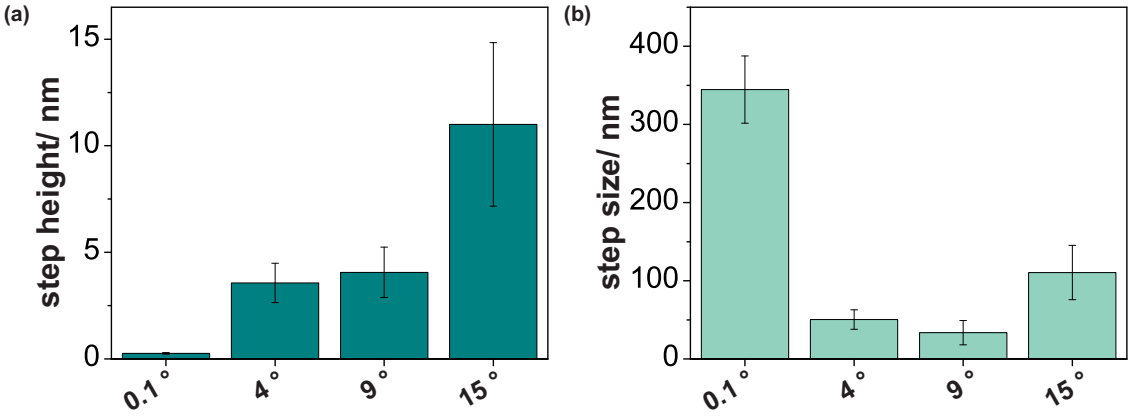

Figure 5.3: Comparison of step (a) height and (b) size of 0.1°,4°,9° and 15°-tilted Al_2O_3(0001)-wafers.

in Figure 5.2. In this case, the Pt NPs disclose similar interparticle distances with the 15°-lattice plane sizes. However, as expected the step height increases to 11.00 ± 3.84 nm (Figure 5.3a) and so, the NPs with a diameter of 5-6 nm and an AFM height of 4-5 nm are smaller than the lattice plane height differences. Thus, the particles are suspected to migrate differently on these steps compared to a flat surface like the 0.1°-tilted wafers. In this case, the step edges are suspected to act as diffusion barriers [136].

As a note, it has to be mentioned that not all tilting wafers - independent of the 4°, 9° or 15° tilt angle - display the exact same step heights and step sizes and therefore, the height profiles are subject to variations due to the cutting and processing by the company as it could be seen on wafers from different batches.

Furthermore, the surface potential of 0.1°- and 15°-tilted sapphire wafers was examined with frequency modulation (FM-)KPFM. Due to an increased sinter stability in high surface potential areas, as seen on the amorphous alumina, the question arises if the NPs experience a similar phenomenon by locally different potentials on the tilted sapphire wafers. In comparison with AM-KPFM, the FM-KPFM technique shows improved lateral resolution on small height and potential scales due to the recording of the force gradient which is more sensitively detected by the small tip than by the whole cantilever as with AM-KPFM [170].

First, the measured height- and potential-AFM images of a 0.1°-tilted Al_2O_3-substrate are presented in Figure 5.4. The profiles of height and surface potential differences in the marked boxes are graphed on the right side and the small step illustration with the arrow indicates the view on the lattice planes. For this 0.1°-tilted sapphire wafer, a normalized height drop from 156 pm to -192 pm and thus, a difference of approximately 350 pm was measured while scanning over the lattice plane edge. At the same time, a decline and relative minimum in the potential was observed. Right before the edge appears, the surface potential peaked slightly at +25 mV, while it then dropped to -40 mV at the very end of the step edge. Afterwards, it rose again to a similar potential as before on the other step with relative fluctuations between -10 mV to $+10$ mV. Therefore, the potential on the steps appears not to be impacted by a nearby edge. Only very close to it a change in surface potential of up to 65 mVcan be detected, which results in a rapid drop of the potential while scanning over the lattice plane edge.

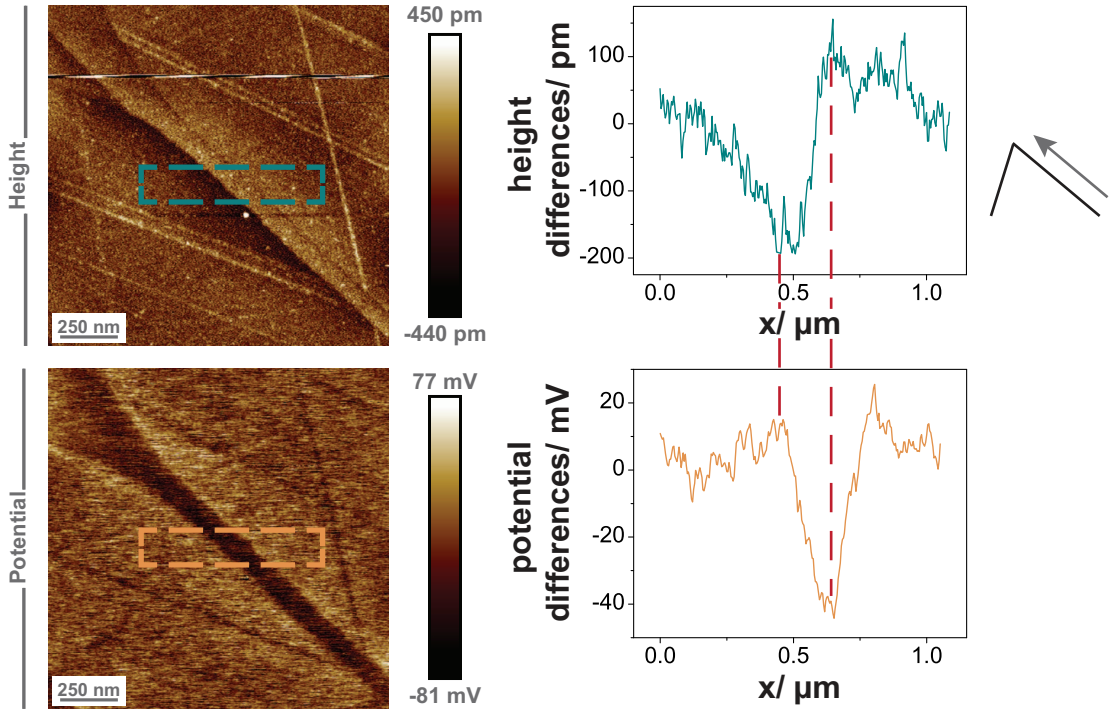

Figure 5.4: Height- and potential-images of a 0.1°-tilted $Al_2O_3(0001)$-wafer in FM-KPFM.

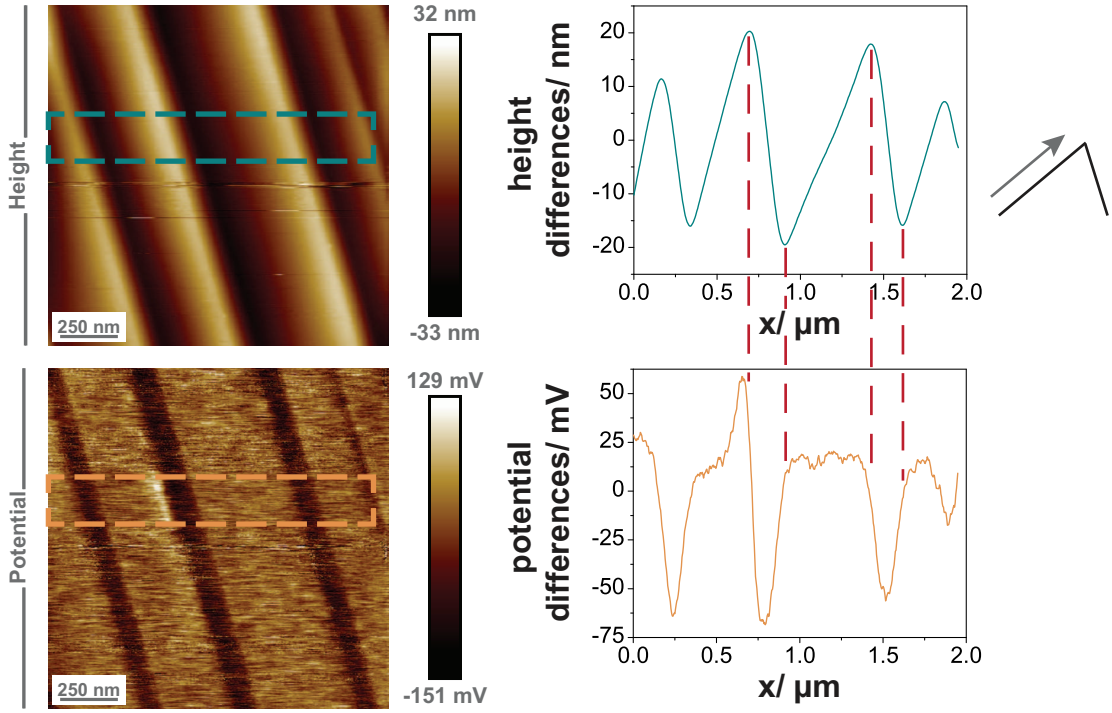

Figure 5.5: Height- and potential-image of a 15°-tilted $Al_2O_3(0001)$-wafer in FM-KPFM.

Secondly, wafers with 15°-tilting angle were observed with FM-KPFM. In Figure 5.5, the height- and potential-images are demonstrated with the respective presentation of the height and potential difference-graphs. Hereby, the behavior of the surface potential is illustrated over three lattice plane edges. These edges exhibited height differences between maximum $+20$ nm and -19 nm and so a drop in height as far as 39 nm occured. At the same time, the potential indicated a significant drop, when the AFM tip was scanned across each step edge. The average surface potential on the step remained similar with only one peak right at the top of the shown edge. Here, the potential rose to $+58$ mV and then declined to -67 mV which yielded a difference of around 125 mV. The other lattice plane edges did not display this peak, yet appear to have a constant surface potential. This single peak might be caused by surface irregularities and measurement inaccuracies. However, directly after each step edge the potential sinks very rapidly by approximately 70 mV.

Summarizing the FM-KPFM experiments, the surface potential experiences a considerable reduction when the AFM tip is scanned over a step edge. Very close to the top of the lattice plane edge an additional increase in potential can be measured for some steps. Yet, the surface potential is relatively constant for all lattice planes remote from this edge. Thus, the drop in potential, as well as the acting of the step edges as diffusion barriers should impact the NP's behavior in the sinter studies [136].

5.2 Sinter studies of platinum nanoparticles on tilted sapphire wafers

The sintering behavior of 5-6 nm sized Pt NPs was then studied on the above characterized 0.1°, 4°, 9° and 15°-tilted *c*-plane (0001) sapphire wafers. Hereby, the discrepancies in nanoparticle coarsening were examined with a special focus on the influence of different step heights and sizes of these tilted substrates. The sinter studies were performed at 750°C in air and also at 1200°C under vacuum.

5.2.1 Sinter study in air at 750 °C

The coarsening behavior of Pt NPs on 0.1°, 4° and 9°-tilted sapphire wafers was analyzed during a sinter study at 750°C under atmospheric conditions. The resulting SEM pictures are shown in Figure 5.6. At 0 min, the Pt NPs are well-arranged in their quasi-hexagonal structure on the 0.1°-tilted substrates, which serve as references. After a heat treatment at 750°C for 10 min, the nanoparticles start to sinter and bigger platinum clusters are oberved. In general the particles start to spread on the sapphire substrate, visible by flat enlarged spots compared to the initial state. This is most probably due to wetting of the Pt NPs and diffusion processes of platinum on the sapphire-surface. Additionally, the hexagonal pattern starts to disintegrate. Sintering for longer times, big clustered nanoparticles appear at 20 min while only a minor fraction of small original particles can still be found. At this time point, most of the Pt NPs sintered to large ones, which is comparable with the sinter study on crystalline *r*-plane (1-102) alumina, as seen in Figure 4.4.

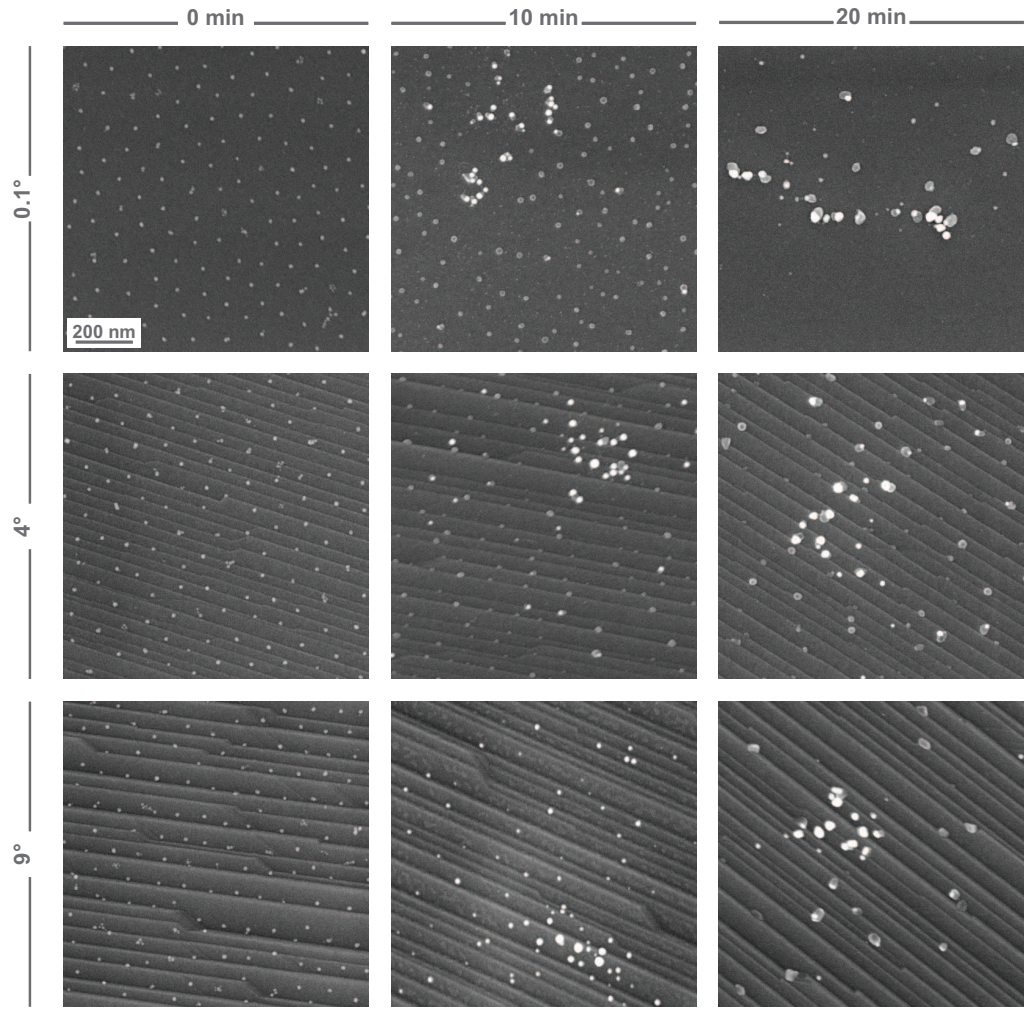

Figure 5.6: SEM images of Pt NPs on 0.1°, 4° and 9°-tilted Al_2O_3(0001)-wafers during sinter studies in air at 750°C after different time periods. The scale bar in all SEM pictures represents 200 nm.

On Al_2O_3(1-102) the particles migrated and coalesced upon meeting each other and the PMC mechanism was determined to govern the coarsening of the Pt NPs. This also seems very likely to be the case on these 0.1°-tilted substrates. From the SEM-images in Figure 5.6, the contribution of Ostwald ripening (OR) cannot be evaluated due to the rapid sintering in the oxygen-containing air.

Also on the 4°-tilted ones, the NP structure appears to be highly regular at the initial 0 min-time point, which supposes that the step heights and sizes of the lattice planes do not interfere with the spin coating process of the micelles. Because of an average step size of approximately 50 nm and an interparticle distance of 80-120 nm, the Pt NPs are individually placed on these lattice steps in a perpendicular direction of the latter ones. After exposing the nanoparticles to a heat treatment at 750°C for 10 min, big clustered particles start to show up. At the same time, spread out smaller platinum particles are preferentially observed at the edges of the steps which seem to be favored by the nanoparticles. This is possibly caused by the measured higher surface potential at the edge before it starts to drop when crossing it. Later on at 20 min, the bigger particles continue to grow

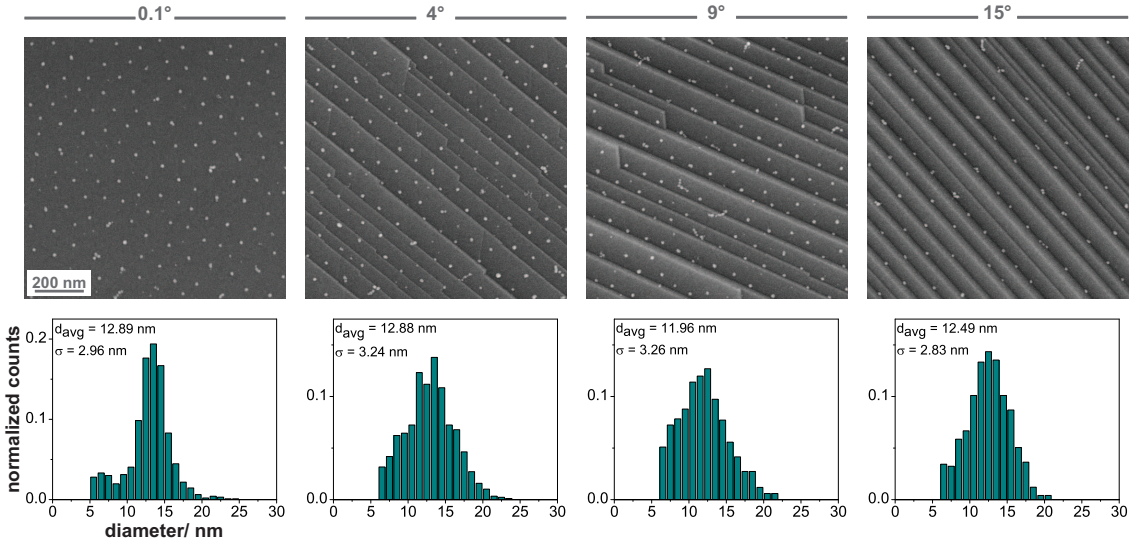

Figure 5.7: SEM images and corresponding PSDs of Pt NPs on 0.1°, 4°, 9° and 15°-tilted $Al_2O_3(0001)$-wafers. The scale bar in all SEM pictures represents 200 nm.

and less small nanoparticles are detected. Again most of the particles appear to prefer the edge of the (0001)-lattice plane steps.

Lastly, the sintering behavior of Pt NPs on 9°-tilted sapphire wafers is presented in Figure 5.6. Contrary to the 0.1° and 4°-ones, the Pt NPs are not regularly arranged in their quasi-hexagonal structure anymore, caused by higher step heights. Here, the particles tend to align rather along the bottom of the lattice plane edges due to a local trapping of the micelles during spin coating. After a heat treatment at 750°C for 10 min, big sintered nanoparticles are seen and the structure of the small particles dissolves completely. Interestingly, for all 0.1°, 4° and 9°-tilted wafers these bigger platinum clusters are especially located very close to each other and not frequently scattered across the whole surface of the wafer. Continuing the oven procedure for 20 min, almost none of the small nanoparticles can be detected for the 9°-tilted sapphire substrates anymore. Only very spread out and big sintered ones are visible, preferably positioned at the step edges. Even though the nanoparticle diameter is in the range of the step heights on the 4° and 9°-tilted supports, no obvious difference in sintering mechanism can be distinguished. The step edges, which act as Ehrlich-Schwoebel barriers, do not hinder the migration of the nanoparticles or the diffusion of the adatoms if OR is present when compared to the reference flat 0.1°-tilted substrates. This is either induced by the high temperature which provides the energy to overcome this barrier or by sintering through volatile platinum oxide particles in the oxygen-containing atmosphere.Yet, overlapping of the spread out big sintered particles and neck formation of these ones, as described for the PMC meachnism, are apparant.

5.2.2 Sinter study in vacuum at 1200 °C

To further evaluate the sintering behavior at a slower pace, another study was performed under vacuum at 1200°C during a time period of 48 h. The absence of oxygen is reported to decrease the sintering rate due to the favorable formation of metal oxide clusters with lower adsorption energies

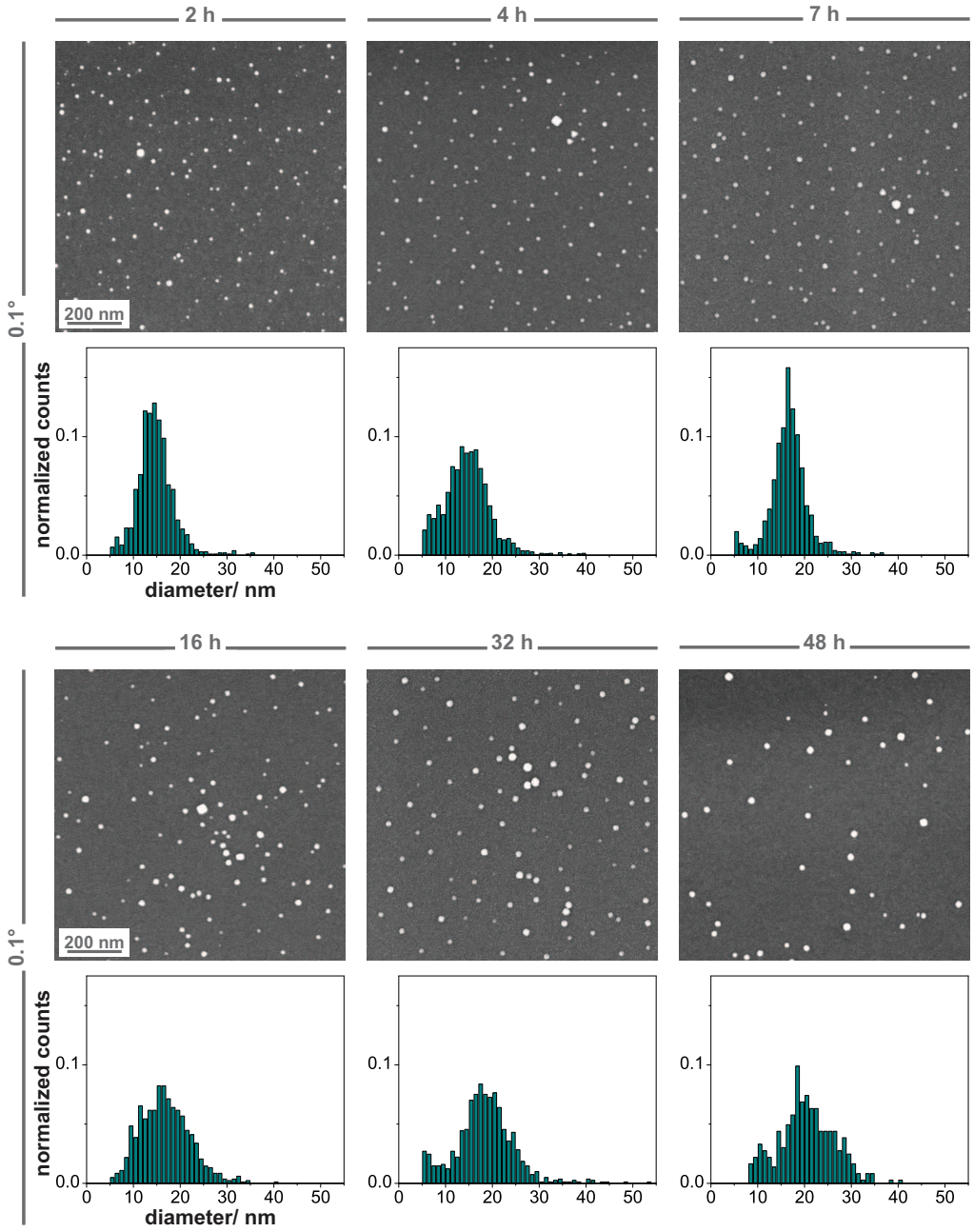

Figure 5.8: SEM images and corresponding PSDs of Pt NPs on 0.1°-tilted $Al_2O_3(0001)$-wafers during sinter studies under vacuum at 1200°C after different time periods. The scale bar in all SEM pictures represents 200 nm.

	0 h	2 h	4 h	7 h	16 h	32 h	48 h
mean height	12.89	14.74	14.68	16.66	16.85	18.42	20.46
standard deviation	2.96	3.87	4.94	4.14	5.30	6.38	5.89
number of NPs	964	1044	1846	1005	827	812	364

Table 5.1: Mean heights, standard deviations and the numbers of evaluated NPs extracted from PSDs obtained with SEM for the sintering of Pt NPs on 0.1°-tilted $Al_2O_3(0001)$-wafers during sinter studies under vacuum at 1200°C.

and thus a faster transport across the substrate towards other particles in oxygen-containing atmospheres [74, 66, 164]. The nanoparticle coarsening in vacuum was monitored through SEM-images and particle size distributions (PSDs) were extracted from these high-resolution pictures with the help of the program ImageJ. The PSDs are presented underneath the corresponding SEM images. Importantly, the resolution limit of the SEM in the range of the NPs' size and the approximately 7 nm carbon coating of the samples to achieve conductive specimens have to be considered when evaluating the obtained results.

As the starting position, the 0 h-samples of 0.1°, 4°, 9° and 15°-tilted sapphire wafers with immobilized 5-6 nm Pt NPs are presented in Figure 5.7. Here, the NPs are regularly arranged in their quasi-hexagonal pattern on the 0.1°-substrates. On the 4°-ones, the continuous structure starts to break down. This phenomenon is further intensified on the 9° and 15°-tilted wafers and provoked by the rising step heights of the latter more tilted substrates. There, the micelles are locally trapped at the bottom of the edges during spin coating and the nanoparticles align along the steps, presenting an irregular hexagonal structure. This effect is particularly present on the 15°-wafer due to an approximately two-fold higher step height compared to nanoparticle size. The associated PSDs underneath the SEM images reveal a Gaussian-shaped distribution for all of the 0 h-samples on the different substrates. However, the shape of the graph with its main peak varies slightly and therefore, mean nanoparticle diameter values of 12.89 $\pm$ 2.96 nm on the 0.1°-, 12.88 $\pm$ 3.24 nm on the 4°-, 11.96 $\pm$ 3.26 nm on the 9°- and 12.49 $\pm$ 2.83 nm on the 15°-tilted supports are calculated. The considerable higher average diameter of 12-13 nm in the SEM images compared to the 5-6 nm size measured by TEM can be explained by the approximately 7 nm-thick carbon coating on the SEM samples to avoid charging triggered by the electron beam. Also, the variations in mean nanoparticle diameter and standard deviations in SEM of the same Pt NP solution are induced by the following size analysis in ImageJ. For this a threshold has to be applied, which yields minorly diverging results.

Afterwards, the nanoparticle coarsening was observed for the 0.1°-tilted sapphire wafers over 48 h and the resulting SEM-images and PSDs are shown in Figure 5.8. The 0.1°-substrates serve as references since their step height is significantly smaller than the NP size and since their step size is considerably larger than the NP interparticle distance. So, the Pt NPs should not be majorly affected by the exposed steps. Due to the absence of oxygen, the sintering rate is drastically reduced and the time interval was extended to much longer periods. After 2 h, the intial structure of the nanoparticles begins to disintegrate by the diffusion of whole nanoparticles on the sapphire surface. Because of this phenomenon and the absence of very small particles, Ostwald ripening can be ruled out as dominating sintering mechanism which agrees with the previous results in chapter 4. Also, the center of the main peak in the PSD shifts from around 13-14 nm for 0 h to 15 nm for 2 h. Additionally, a few larger sintered particles are detected with sizes ranging up to 35 nm. The general average diameter and standard deviation (shown in Table 5.1) changes from 12.89 $\pm$ 2.96 nm at 0 h to 14.74 $\pm$ 3.87 nm for 2 h. Continuing this trend, the PSD further broadens at 4 h with a central peak shift to 15-18 nm and a calculated mean and standard deviation of 14.68 $\pm$ 4.94 nm, while large particles with a size up to 40 nm are seen in the SEM image. After treatment at 1200°C for 7 h, the center of the peak further moves to 17-18 nm. Yet, most of the initial small particles are still observed in their regular arrangement. This changes drastically

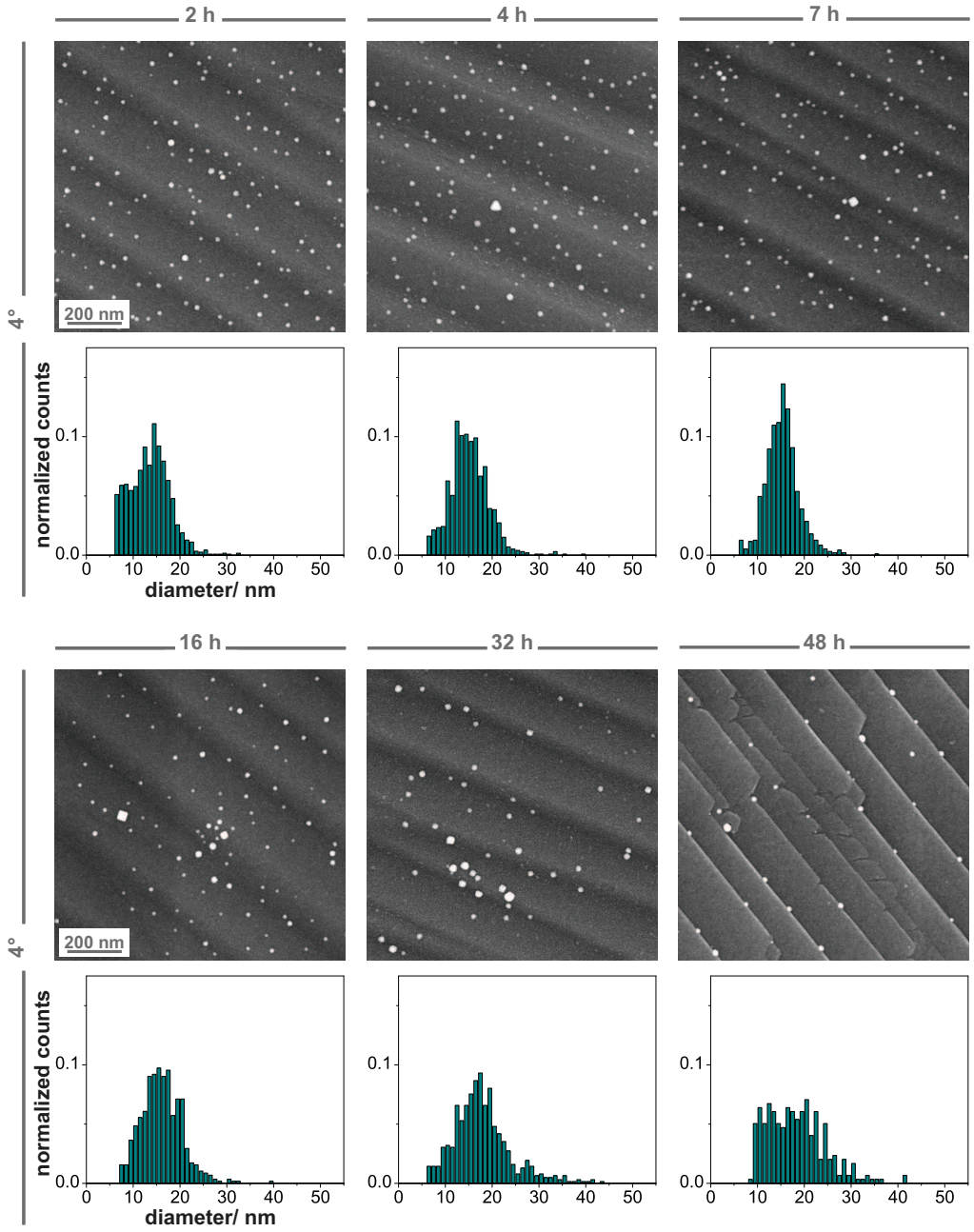

Figure 5.9: SEM images and corresponding PSDs of Pt NPs on 4°-tilted $Al_2O_3(0001)$-wafers during sinter studies under vacuum at 1200°C after different time periods. The scale bar in all SEM pictures represents 200 nm.

	0 h	2 h	4 h	7 h	16 h	32 h	48 h
mean height	12.88	13.60	15.15	15.32	16.12	17.89	18.28
standard deviation	3.24	4.24	4.17	3.52	4.33	6.14	6.22
number of NPs	885	1172	990	948	576	623	297

Table 5.2: Mean heights, standard deviations and the numbers of evaluated NPs extracted from PSDs obtained with SEM for the sintering of Pt NPs on 4°-tilted $Al_2O_3(0001)$-wafers during sinter studies under vacuum at 1200°C.

after 16 h and can be seen in the corresponding SEM-image. The structure is almost completely dissolved and more NPs grow in size. From this time point on, the PSDs broaden with a rise in particle sizes to values above 20 nm. Thus, the average mean diameters and standard deviations which only give an indication on the sintering behavior of the Pt NPs increase to 18.42 $\pm$ 6.38 nm for 32 h and 20.46 $\pm$ 5.89 nm for 48 h. At the last time point, only a reduced number of larger platinum particles are visible while the majority of the small ones disappeared. The governing sintering mechanism seems to be PMC as mentioned above due to the disintegration of the original structure. However, the absence of very small nanoparticles cannot be guaranteed due to the lower resolution of these PSDs obtained with SEM compared to the ones obtained by AFM in chapter 4. Yet, the increasing step heights on the subsequently presented substrates make precise height-measurements at the AFM impossible. Thus, Ostwald ripening could contribute to the sintering behavior of these Pt NPs, which has to be further analyzed.

Next, the nanoparticle coarsening was monitored on the 4°-tilted sapphire wafers and the resulting SEM-images and PSDs are shown in Figure 5.9. The Pt NPs start to lose their original structure after 2 h through particle diffusion on the Al_2O_3(c)-surface which visibly continues for the 4 h and the 7 h-samples. Simultaneously bigger sintered nanoparticles are featured at these time points. Also a few larger ones are detected at 2 h and presented in the PSD with a tail of diameter sizes up to 32 nm. Yet, at the 4 h-time point, even larger particles with 40 nm diameter appear. Generally the central peak in the PSDs shifts to around 15 nm during the first 7 hours, while it was initially detected at 13-14 nm. The calculated mean diameters and standard deviations (Table 5.2) underline this trend with 12.88 $\pm$ 3.24 at 0 h, 13.60 $\pm$ 4.24 nm at 2 h, 15.15 $\pm$ 4.17 nm at 4 h and 15.32 $\pm$ 3.52 nm at 7 h. As seen on the 0.1°-sample, the NP structure is almost completely disintegrated on the 4°-tilted substrate at 16 h and more sintered particles are observed. With a broadened PSD and an average diameter of 16.12 $\pm$ 4.33 nm, further coarsening is indicated. Continuing for 32 h and 48 h, the small particles start to disappear to a greater extent and a more pronounced tail towards nanoparticles with sizes above 40 nm is detected. Thus, the mean NP diameter increases to 17.89 $\pm$ 6.14 nm at 32 h and 18.28 $\pm$ 6.22 nm at 48 h. As it can be seen in the latter SEM pictures, the sintered nanoparticles align preferentially at the edge of the steps, which could be related to the higher surface potential at these points before it drops over the edge. Noticeably, the steps on all of these 2 h to 48 h-samples differ in size compared to the 0 h-sample (Figure 5.7). Yet, this nanoparticle coarsening behavior was repetitively seen on samples with narrower steps as well.

Following, the nanoparticle coarsening was monitored on the 9°-tilted sapphire wafers and the resulting SEM-images and PSDs are shown in Figure 5.10. While the nanoparticles tend to be more aligned along the steps at 0 h (Figure 5.7), at 2 h no considerable loss in Pt NP-structure is observed, opposed to the 0.1°- and 4°-substrates. Here, the average diameter in the corresponding PSD (Table 5.3) increases from 11.96 $\pm$ 3.26 nm to 14.54 $\pm$ 3.51 nm. However, this is caused by a few larger particles with a size of approximately 30 nm, while the central peak is still observed at the same position as on the starting sample. Continuing the heat treatment for 4 h and 7 h, a rising number of bigger sintered particles with diameters up to 40 nm is detected. This leads to larger standard deviations with 4.21 nm for 4 h and 4.08 nm for 7 h. Yet due to many unsintered small particles, the average diameter does not change with 13.96 nm at 4 h and

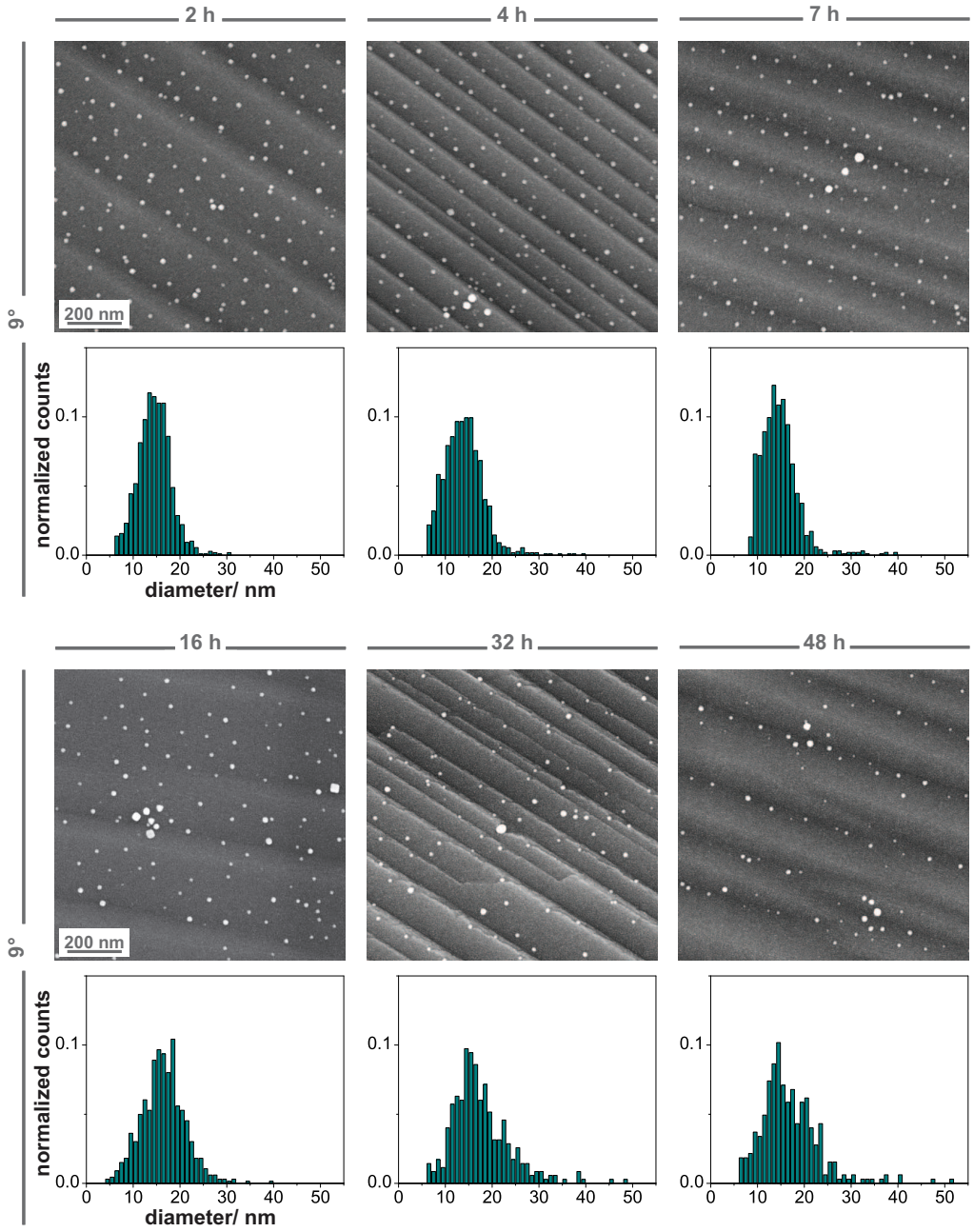

Figure 5.10: SEM images and corresponding PSDs of Pt NPs on 9°-tilted $Al_2O_3(0001)$-wafers during sinter studies under vacuum at 1200°C after different time periods. The scale bar in all SEM pictures represents 200 nm.

	0 h	2 h	4 h	7 h	16 h	32 h	48 h
mean height	11.96	14.54	13.96	14.73	16.44	17.46	16.94
standard deviation	3.26	3.51	4.21	4.08	4.68	5.64	6.34
number of NPs	843	1082	1097	985	662	347	324

Table 5.3: Mean heights, standard deviations and the numbers of evaluated NPs extracted from PSDs obtained with SEM for the sintering of Pt NPs on 9°-tilted $Al_2O_3(0001)$-wafers during sinter studies under vacuum at 1200°C.

14.73 nm at 7 h. Most small NPs still preferentially remain in their position along the steps with no obvious hexagonal arrangement while a few agglomerate. This is likely generated by the diffusion of platinum clusters on the sapphire-surface at this high temperature. As seen before on the other tilted wafers, after 16 h the nanoparticles show a rising number of large particles and an advanced coarsening, which is also indicated by the broader size distribution with a mean diameter and standard deviation of 16.44 $\pm$ 4.68 nm. It appears that less small particles exist while the majority of the particles is enlarged at this time point. Furthermore, after the heat treatment at 1200°C for 32 h, very large clusters of approximately 50 nm arise. The quantity of small particles diminishes and the average diameter shifts to 17.46 $\pm$ 5.64 nm. Hereby, the particles are clearly more arranged towards the step edges when compared to the starting alignment along the bottom of the steps. Thus, the higher surface potential at the lattice step edges presumably attracts the nanoparticles which could be caused by higher particle-substrate interactions leading to longer NP retention times there. Also, they can act as ES barriers so the nanoparticles are hindered to cross over the edges and therefore, the diffusion and migration of the sintered particles is stopped there for some time. The 48 h-time point emphasizes this behavior with large 50 nm-sized sintered particles at the edges and few small nanoparticles remaining at the bottom of the steps. Hereby, the mean diameter of 16.94 $\pm$ 6.34 nm is similar to the one at 32 h.

Lastly, the nanoparticle coarsening was monitored on the 15°-tilted sapphire wafers and the resulting SEM-images and PSDs are shown in Figure 5.11. As it could be seen in Figure 5.7, the nanoparticles are almost completely placed at the bottom of the steps at 0 h. After an oven treatment for 2 h, this phenomenon remains while only a few slightly bigger particles of 20-30 nm size are detected at the step edges. Thus the PSD results in a similar average diameter for these first two time points, but an increased standard deviation (Table 5.4). They are calculated to be 12.49 $\pm$ 2.83 nm for the 0 h-sample and 12.82 $\pm$ 3.67 nm for the 2 h-sample. This trend is reinforced on the 4 h-wafer, where more sintered particles with a size of 40-45 nm migrate towards the edges with the observed higher surface potential, yielding a mean diameter of 13.96 $\pm$ 4.09 nm. Generally, the structure of the small nanoparticles appears to be unaffected during longer heating periods up to 7 h in comparison with the flat 0.1°- and 4°-tilted sapphire wafers. Here at 7 h, the PSD still shows a narrow size distribution without a shift of the central peak and an average diameter of 14.20 $\pm$ 3.67 nm for the 15°-tilted samples. At 16 h however, the NPs' regular structure disintegrates. At this time point, very small particles are observed at the bottom of the steps, while sintered ones are located at the edges. Even though large 40 nm-sized agglomerates are present, the PSD continues to remain at a mean of 14.54 $\pm$ 4.36 nm due to the abundance of small unsintered nanoparticles. However, it has to be noted that the sizes of these small particles are difficult to evaluate due to the dominant step edges in the SEM and in the ImageJ-analysis. Thus, their diameter can differ from the actual value. Yet, at 32 h and 48 h, the distributions of the diameters broaden and large coarsened particles are clearly observed at the step edges. This is also presented by the increasing mean size average and standard deviation of 15.11 $\pm$ 7.11 nm for 32 h and 17.09 $\pm$ 7.10 nm for 48 h. As mentioned above the edges demonstrate higher surface potentials which seems to be favored by the sintered Pt NPs, as observed in the SEM images.

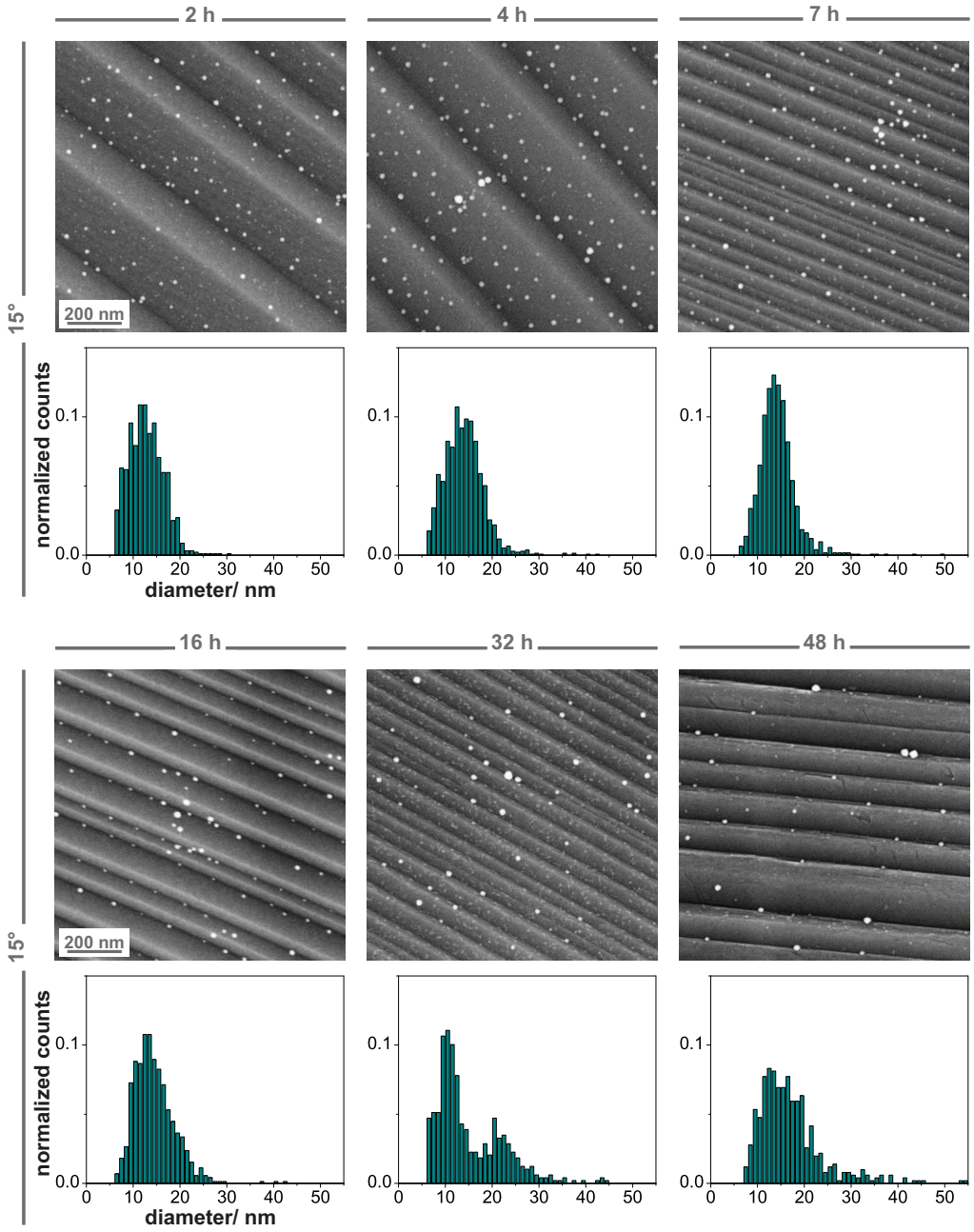

Figure 5.11: SEM images and corresponding PSDs of Pt NPs on 15°-tilted $Al_2O_3(0001)$-wafers during sinter studies under vacuum at 1200°C after different time periods. The scale bar in all SEM pictures represents 200 nm.

	0 h	2 h	4 h	7 h	16 h	32 h	48 h
mean height	12.49	12.82	13.96	14.20	14.54	15.11	17.09
standard deviation	2.83	3.67	4.09	3.67	4.36	7.11	7.10
number of NPs	495	920	1369	1242	715	488	505

Table 5.4: Mean heights, standard deviations and the numbers of evaluated NPs extracted from PSDs obtained with SEM for the sintering of Pt NPs on 15°-tilted $Al_2O_3(0001)$-wafers during sinter studies under vacuum at 1200°C.

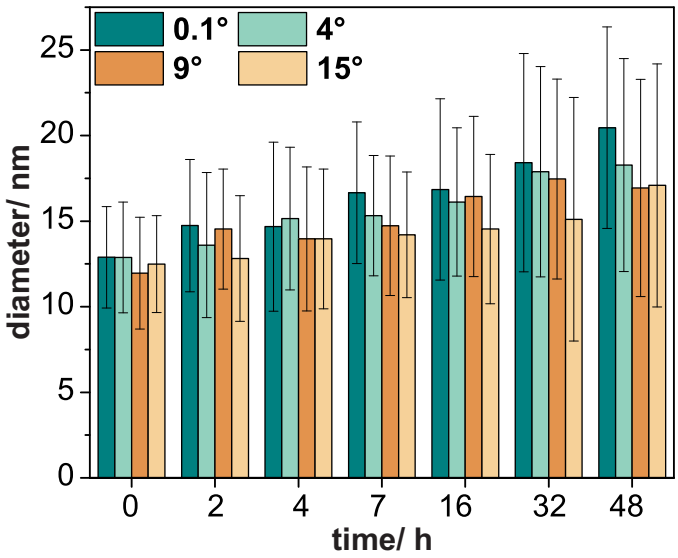

Figure 5.12: Mean diameters extracted from PSDs of 0.1°, 4°, 9° and 15°-titled $Al_2O_3(0001)$-wafers under vacuum at 1200°C after different time periods.

In general, on the 4°, 9° and 15°-tilted sapphire wafers, different morphologies of the substrate are visible. Some reveal clear and precise edges, while others seem to show flatter ones, as in Figure 5.9 and 5.10. Also the step sizes vary considerably between the tested substrates, seen in Figure 5.10 and 5.11. On one hand, this is generated by divergently cut sample batches bought by CrysTec. On the other hand, a restructuring of several surfaces additionally appears, even though, all subtrates were annealed at the same temperature and for the same time duration. This could impact the obained results and thus, the performed sinter studies can only be considered as pretests.

A summary of the above calculated average diameters and standard deviations in the 1200°C-vacuum sinter study is presented in Figure 5.12. Generally speaking, the Pt NPs all coarsen over the 48 h-time interval independent on the tilting angle of the sapphire wafers. However, the increase in average diameter is slightly less on the 9°- and 15°-samples with a mean diameter of around 17 nm after the heat treatment compared to 18 nm for the 4°-ones and 20.5 nm for the 0.1°-ones. It appears that the nanoparticle sintering is reduced and slows down on the more tilted substrates. Interestingly, the large particles all preferentially align along the step edges for the 4°-, 9°- and 15°-tilted samples where a higher surface potential is present. This agrees with the observed slower NP sintering on the amorphous alumina which demonstrated an increased surface potential measured in KPFM compared to the other three tested substrate materials (Figure 4.9). Thus, the nanoparticles tend to prefer these locations. Additionally, the step edges can act as Ehrlich-Schwoebel barriers that hinder the surface migration and diffusion of the platinum clusters. Due to the irregular intial nanoparticle arrangement on the more tilted supports, a clear distinction of the underlying sintering mechanism is complex and not fully possible. As opposed to the AFM, the SEM does not allow to record tiny particles. Ostwald ripening by the diffusion of adatoms could participate in the nanoparticle coarsening mechanism, yet can not be explicitly concluded from the SEM images. On the contrary, migration of larger sintered platinum particles at 1200°C under vacuum was seen on the SEM images from the bottom of the steps to the edges,

as for example on the 16 h-, 32 h- and the 48 h-15°-tilted samples in Figure 5.11. This leads to the conclusion that PMC plays a crucial rule in the sintering of Pt NPs on tilted sapphire wafers.

5.3 Summary

Differently tilted *c*-plane (0001) sapphire wafers were characterized regarding their height profiles in AFM. With increasing tilt angles varying from 0.1° to 15°, the substrates reveal steps with elevating step heights. These are comparable to the nanoparticle diameters for the 4°- and 9°-ones and exceed the nanoparticle size for the 15°-ones. Simultaneously, the step size decreases overall to a dimension similar or smaller than the average interparticle distances between two platinum nanoparticles. Both effects cause the NPs to not be continuously arranged in the quasi-hexagonal pattern anymore on the more tilted supports due to local trapping of the micelles during the spin coating process on the bottom of the steps. With FM-KPFM the surface potential was measured on a flat 0.1°-substrate in analogy to the 15°-substrate. Generally, a significant drop in potential was observed when the AFM tip was scanned over the edges. On the 0.1°-sample a 65 mV-decrease was detected, while the 15°-sample with a much higher step height revealed a 125 mV-decline. As seen on the amorphous alumina, the sinter stability is greatly enhanced in high surface potential areas. Thus, the drop in potential, as well as the functioning of the step edges as diffusion barriers should impact the NP's behavior in the sinter studies.

Afterwards, the coarsening behavior of Pt NPs was studied on these sapphire wafers. First, it was analyzed in a sinter study under atmospheric conditions at 750°C over 20 min yielding no distinct variation in NP coarsening for 0.1°, 4° and 9°-tilted substrates. Rapid sintering was observed for all samples with PMC governing it. In order to slow down this process and to further study the effect of the step edges on the sintering behavior of Pt NPs, the second sinter study was performed under vacuum at 1200°C for a time period of 48 h. In the absence of oxygen, the coarsening rate of the nanoparticles could be significantly reduced. Thus, the sintering in the first study has to occur at least partially via the diffusion and migration of volatile platinum oxide clusters when compared to the vacuum sinter study. Here, all of the nanoparticles slowly coarsened on the tested sapphire wafers with tilt angles between 0.1° and 15° during 48 h through the appearance of very large 50 nm-sized particles. Yet, the increase in average diameter of the sintered platinum clusters was slightly less for the more tilted substrates compared to the flatter supports. Also, the nanoparticles remained longer in their initial arrangement before losing its regular structure during the heat treatment. The majority of the large sintered particles could then be detected at the step edges of the tilted wafers after 48 h, as hypothesized in the FM-KPFM experiments. This observed phenomenon is attributed to the higher local surface potential at the edges before it drops when crossing it and to the functioning of the edges as Ehrlich-Schwoebel barriers, which hinder the migration and diffusion of the particles. Yet, the obtained results can only be taken as indications due to different surface appearances on equally tilted sapphire wafers. This is either caused by variations in the cutting-process by the company or generated by the reconstruction of the surfaces at 1200°C over extended time periods. However, a decrease in sintering rate was observed on more tilted wafers and thus substrates with surface heterogeneities or structuring composed of step edges can enhance the sinter stability.

6 Isolation of platinum nanoparticles via oxide layers

After investigating the influence of the substrate regarding its physical and chemical properties on the sintering behavior of platinum nanoparticles, this chapter focuses on isolating these nanoparticles from each other. By depositing a thin oxide layer on, or preferably around, the particles, this research aims to increase the Pt NPs' coarsening resistance by hindering surface diffusion of platinum clusters or of whole particles. All Pt NPs were immobilized on amorphous alumina, Al_2O_3(a), and the effect of a thin silica and a thin alumina layer was tested during sinter studies in air at 750°C.

For this thesis, the synthesis of oxide layers was adapted from Dipl.-Ing. Mirjam Eisele, Institute for Materials Science Chair 3 at the University of Stuttgart. Additionally, after establishing the experimental procedures the presented results were obtained within the framework of a masterthesis by Tingyu Zhang, B.Sc. under my supervision.

6.1 Theoretical background for nanoparticle isolation with silica and alumina layers

6.1.1 Sol-gel synthesis of silica and alumina layers

Due to its superior simplicity, as well as high purity and homogeneity of the achieved products and due to its low processing temperatures, the sol-gel technique is favored for synthesizing inorganic ceramic oxides and glasses in complex shapes or as thin coatings [68, 31, 153]. The characteristic feature hereby is the transformation of a solution or sol into a rigid gel with tunable porosity. Typically starting with a metal alkoxide solution, as seen in Figure 6.1, a sol as dispersion of colloidal particles in a liquid solution is formed through hydrolyzation and

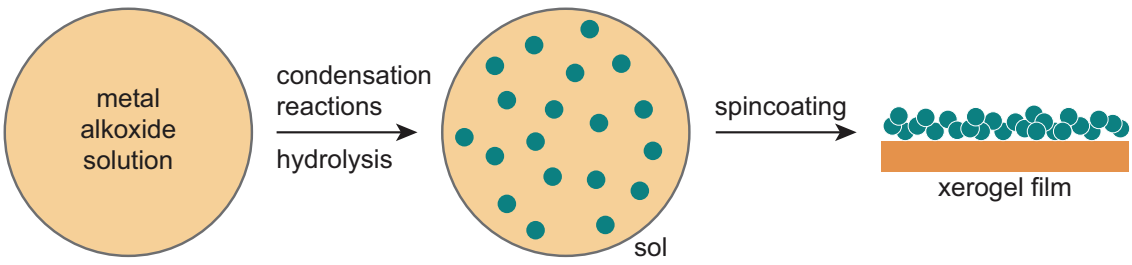

Figure 6.1: Schematic principle of a modified sol-gel process used in this thesis to obtain porous ceramic oxide layers.

condensation reactions. These colloids are small solid particles of sizes ranging between 1 nm and 100 nm. During the condensation monomers polymerize and build up chains and particles which furthermore, grow larger in diameter and agglomerate towards an interconnected 3D network. This gel consists of polymer chains larger than 1 µm and pores in the sub-µm-size range. Coatings can then be achieved by either dip or spin coating it onto the substrates [31, 153]. Depending on the way the liquid in the pores is removed either an areogel of low overall density is fabricated by drying under hypercritical conditions or a xerogel is produced when drying at ambient pressures through thermal evaporation [68].

First only used to prepare common glasses and ceramics in the 18th century [153], coatings and films are gaining importance. These are of particular interest for ionic conductors, for antireflection purposes with the example of indium tin oxide and its advanced insulation properties in glass windows or for corrosion protection applications due to their distinguished chemical stability [77, 68, 153, 18]. Fibers are another fabrication shape for sol-gel synthesized glasses and ceramics [68]. As an example, Choi *et al.* recently reported the fabrication of silica nanofibers with diameters as small as 200 nm [37]. Additional applications of sol-gel processed materials feature the use of areogels as thermal superinsulators in solar energy systems with porosities up to 98 % [151] and their operation as catalysts or catalyst supports in the case of silica, alumina, zirconia and titania amongst other inorganic ceramic oxides [103]. Lastly, in the past 25 years the sol-gel synthesis has also been implemented in the biomaterials field. Lu *et al.* synthesized a 2-100 nm thick silica shell with incorporated fluorescent dies around superparamagnetic iron oxide nanoparticles. Thus, they were able to create multifunctional particles that can be triggered by an externally applied magnetic field and simultaneously tracked by *in situ* fluoresence microscopy for medical and biological appliations [87]. As a result of low processing temperatures and mild conditions during the sol-gel technique, enzymes and proteins can also be encapsulated to yield biosensors, electrodes or other advanced biomaterials [8]. For example, Arcos *et al.* applied sol-gel materials composed of silica as drug delivery systems for bone tissue regeneration [4].

In the seventies, one decisive step for the wide popularity of the sol-gel technique was the achievement by Stoeber *et al.* to synthesize monodispersed spherical silica particles while controlling the morphology and size of the powder. They hydrolyzed tetraethyl orthosilicate (TEOS) in alcoholic solutions and in the presence of ammonia which served as the morphological catalyst. Thus, colloidal particles with diameters ranging between 50 nm and 2 µm were achieved [135, 18].

To explain the principle of sol-gel polymerization, the mechanism of silica is given as an example. SiO_2-gels are obtained from silicon alkoxide solutions through the occurence of different reaction steps, which are outlined in Figure 6.2. First, TEOS with $R = CH_2CH_3$ partially hydrolyzes in water to form silanol Si-OH groups (Figure 6.2a). Afterwards, instead of fully hydrolyzing to silicic acid, condensation between either two silanols (Figure 6.2b) or between a silanol and an ethoxy group (Figure 6.2c) takes place resulting in a bridging siloxane Si-O-Si group [31, 68]. Meanwhile water or alcohol are ejected and remain in the pores of the network [68]. These reactions are initiated at various sites within the solution resulting in sol particles whose cross-linking depends on the pH amongst other parameters. Depending on the utilization of an acid- or base-catalyst different final gel shapes are observed. At low pH with a resulting slow hydrolysis, the silica gel constitutes of rather linear molcules with occasional cross-links. However at high

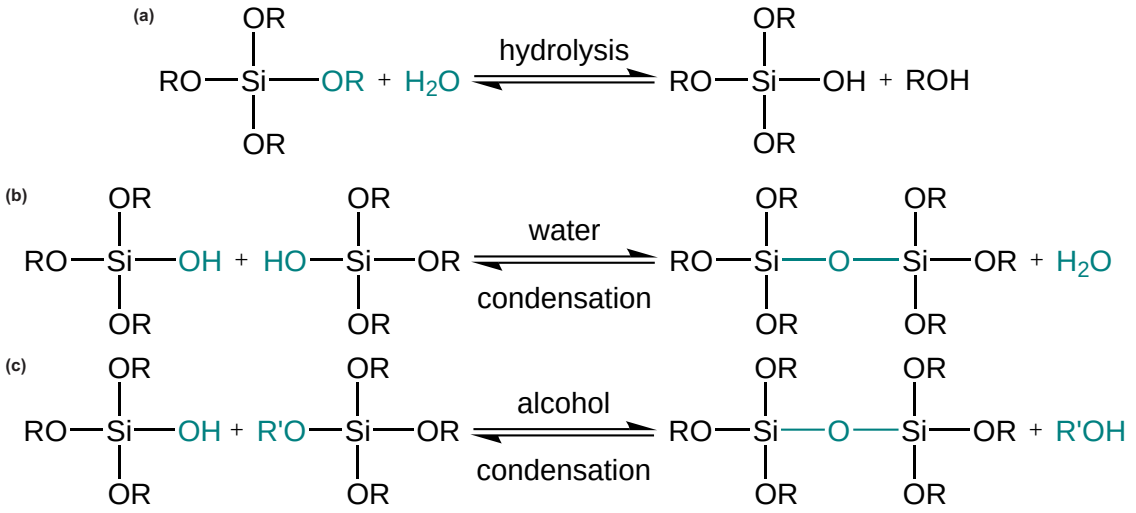

Figure 6.2: (a) Hydrolysis or (b) water and (c) alcohol condensation to form SiO_2-structure in silica solution via TEOS-based sol-gel synthesis.

pH, fast hydrolysis occurs and so independent clusters with more branches are build up. In this thesis, porous silica films were synthesized following the route of Rouse *et al.* by a base-catalyzed sol-gel procedure of TEOS in aqueous solution [116].

Similarly, alumina-gels are obtained by a sol-gel synthesis following the procedure of Nass *et al.* [100]. However, since the aluminum alkoxide aluminum-sec-butoxide (ASB) starting material leads to rapid precipitation during the hydrolysis step, it first has to be chelated with the ligand ethylacetoacetate (EAA), as seen in the reaction of Figure 6.3a. This significantly slows down the reactivity of the aluminum alkoxide towards water [9]. Afterwards, hydrolysis (Figure 6.3b) as described above occurs and a sol of small particles is formed [100].

Such nanocrystalline alumina is then reported to be used as heterogeneous catalyst support with the advantages of high surface area and an elevated number of active alumina sites for the catalytic reaction [91, 154].

6.1.2 Isolation of nanoparticles against sintering

Over the past ten years, isolating noble metal nanoparticles with oxide layers for catalytic applications has become increasingly important to avoid nanoparticle sintering and thus the loss of their catalytic activity. Shielding nanoparticles from each other, Ma *et al.* tested a 20-30 nm thick amorphous silica layer via atomic layer deposition on approximately 5 nm-sized gold nanoparticles which were immobilized on titania. This yielded stabilized particles against nanoparticle coarsening, yet, a loss of catalytic activity resulted from the coverage with SiO_2 [89]. Later on, Feng *et al.* were able to prove an inhibition of sintering at 500°C for compactly and densely covered 1-2 nm palladium nanoparticles (Pd NPs) with a thicker alumina-layer on Al_2O_3-substrates via atomic layer deposition. When applying an extremely thin alumina coat, Pd NPs' activity could be preserved during methanol decomposition. They attributed these phenomena to an improved anchorage of the nanoparticles on the substrates through the alumina layer and to the coverage of only low-coordination palladium sites which

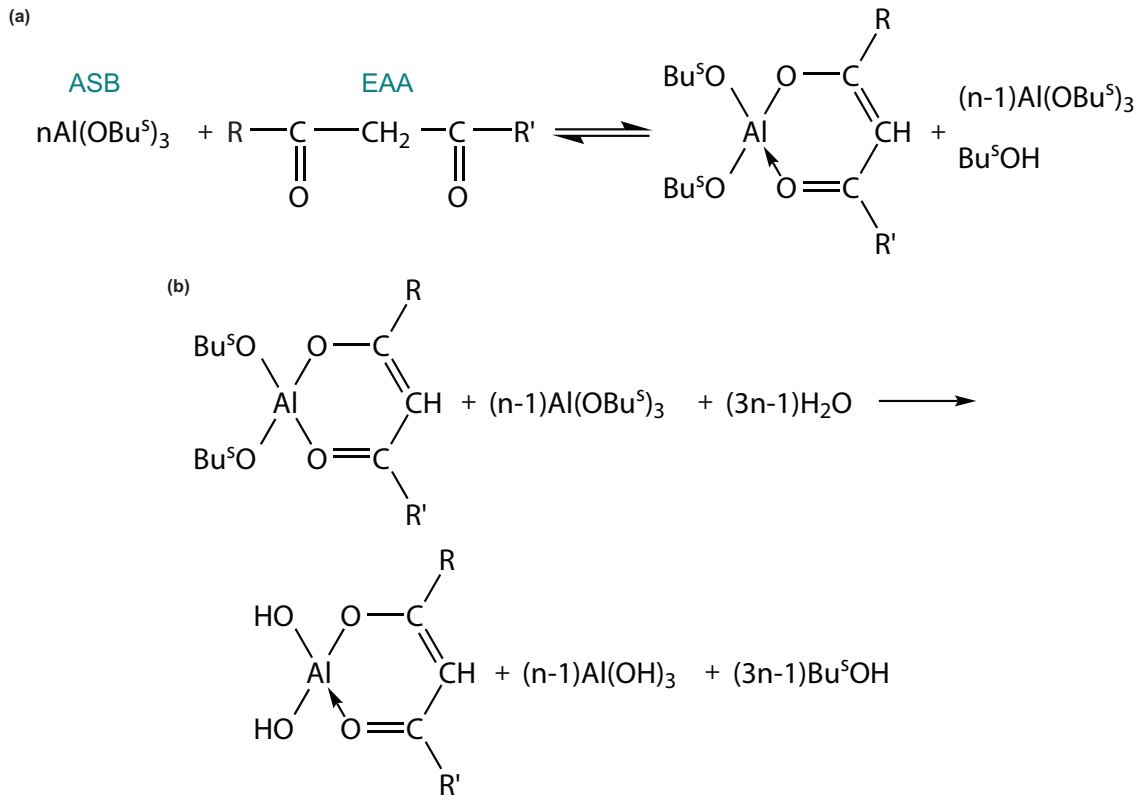

Figure 6.3: Chemical reactions during formation of alumina solution: (a) Chelation of aluminium-sec-butoxide (ASB) with ethylacetoacetate (EAA) and subsequent (b) hydrolysis. R is CH_3 and R' is OC_2H_5 with n = 1-4 [100].

do not effect the NPs' activity [51]. Other approaches include individual encapsulation of gold nanoparticles in hollow silica spheres to separate the metal particles from each other and achieve higher sinter stabilities. Simultaneously, the particles are shielded from poisoning by adsorbing molecules [162]. Similarly, Arnal *et al.* packed individual gold nanoparticles in zirconia spheres with 3-4 nm pores in the shell which stabilized them against elevated temperatures. However, this synthesis route is costly and time-consuming [5]. On the other hand, mesoporous silica can be a promising candidate to slow down NP coarsening. Unsupported 14 nm platinum nanoparticles were covered with a 17 nm-thick SiO_2-shell and resisted sintering up to 750°C under atmospheric conditions. At the same time, the mesoporous structure of the silica layer allowed the free access of the reactants in the ethylene hydrogenation and CO oxidation to reach the platinum core and so, Joo *et al.* claimed to reach catalytic activities comparable to that of uncovered platinum nanoparticles [76]. Another example is the encapsulation of 3 nm-sized Pt NPs on 120 nm silica beads by a thin layer of mesoporous silica with a thickness of only few tens of nanometers. These nanoparticles were observed to coarsen less at temperatures of 800°C, while regaining their catalytic activity for *cis*- and *trans*-2-butenes in the presence of hydrogen after etching of the silica layer [81]. Applying a TEOS-based reaction, Dai *et al.* synthesized a porous silica coating around 3-4 nm Pt NPs deposited on titania nanofibers. Sintering in air at a temperature of 750°C was reduced because the silica sheath slowed down the surface diffusion of platinum clusters or particles by acting as a physical barrier. However, the hydrogenation of methyl red demonstrated a concurrent drop in catalytic acitivity by almost 40 % [43]. Lastly, Lu *et al.*

prevented the coverage of 3-4 nm Pt NPs on a fibrous structure of titania by first capping the particles with PVP before depositing a silica layer via a TEOS-based sol-gel process. Afterwards, the polymer was removed during a calcination step and the Pt NP-surrounding silica coating of a few nanometers slowed down the nanoparticle coarsening. When studying their activity by the model reduction reaction of *p*-nitrophenol, the turn over was slowed down by silica coatings as thick as the platinum particles [86]. Thus, the importance of controlling the layer-thickness to achieve high sinter stability and to maintain high catalytic activity is stressed.

In this chapter, 5-6 nm Pt NPs immobilized on stable amorphous alumina supports were isolated from each other either by a silica or by an alumina layer which were synthesized via sol-gel techniques. The nanoparticle sintering behavior was analyzed at 750°C under atmospheric conditions regarding these two layer materials. The goal was to achieve an enhanced sinter-stable system which could be applied in automotive exhaust combustion applications.

6.2 Isolation of platinum nanoparticles via silica layer

To begin with, the Pt NPs were isolated by a TEOS-based SiO_2-layer. This layer was characterized by focusing on structure, composition and coverage of the nanoparticles. Following the coarsening of these nanoparticles was analyzed in a sinter study with SEM.

6.2.1 Characterization of silica layer

First, the aging of the colloidal particles in the synthesized silica solution was studied with AFM. In Figure 6.4, the resulting images of particles at different aging time ranging between one and 21 days are presented with a constant height scale.

As it can be seen in these AFM images (Figure 6.4) and also later on in the SEM pictures (Figure 6.7), the xerogel film appears to rather consist of individual nanoparticles instead of being a dense layer due to its low thickness of a few nanometers. Evaluating the height by comparting it to the AFM height scale, the colloidal nanoparticles reveal a size remarkably below 4 nm after spin coating the solution onto the amorphous alumina substrates which also comprises a roughness on a 3 nm-scale.

Thus, after 1 day of TEOS sol aging time, tiny silica particles are obtained. These visibly grow during longer stirring times of the solution prior to the spin coating process until they reach a diameter three-to-four-times the initial one after 21 days. The observed triangles are measured independently of the scanning direction, thus it can be assumed that the particles do not exhibit a perfectly spherical shape. Independent of optional measurement inaccurancies and tip artefacts, the size evolution of the silica particles in the sol over time is clearly preserved. This trend was also described by Rouse *et al.* and Eisele [116, 49]. They explained the growth of colloidal silica particles by a stop of nucleation when the monomer concentration falls below a specific solubility value. Thereupon, the particles continue to only grow through the addition of further monomers. These are distributed in the solution and rise in number by the dissolution of smaller silica

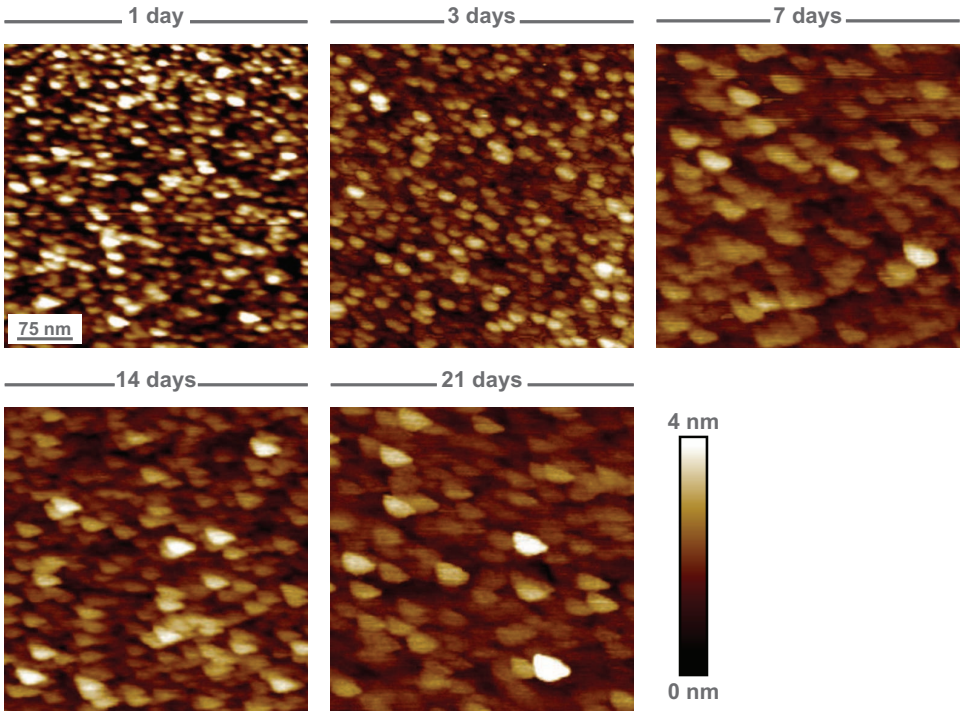

Figure 6.4: Aging study of silica-solution over time with AFM.

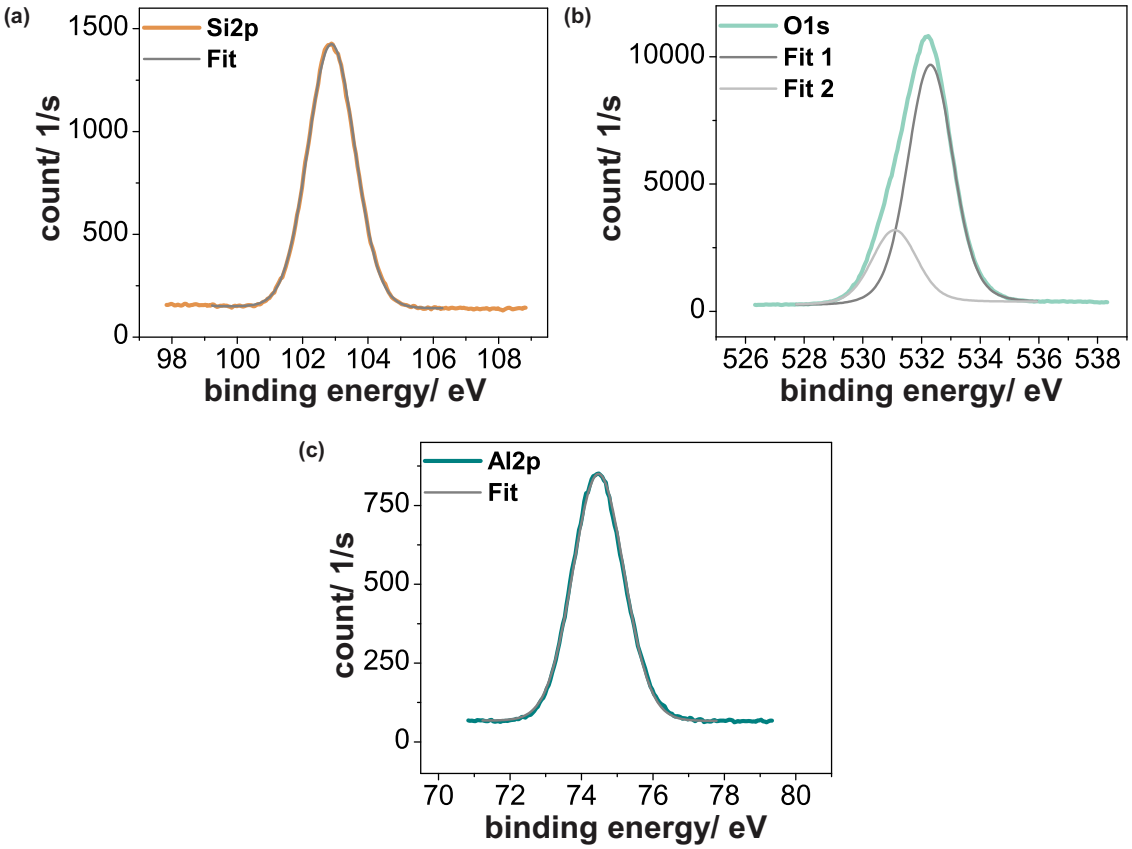

Figure 6.5: XPS-spectra of silica-layer regarding (a) Si-peak, (b) O-peak and (c) Al-peak to confirm SiO_2-formation.

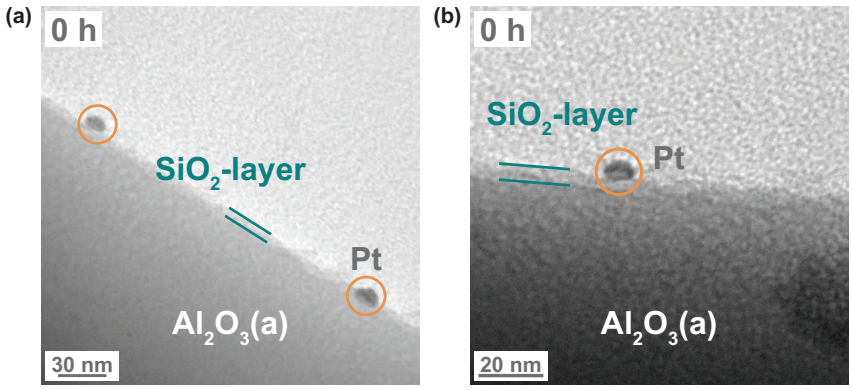

Figure 6.6: (a) and (b) Cross sections of isolated Pt NPs with a silica layer in TEM.

particles according to the Ostwald ripening concept for nanoparticles. Over time, the amount of bigger particles increases while smaller particles disappear [49].

Secondly, the composition of the layer was examined with XPS. The received spectra for silicon (Si2p), oxygen (O1s) and aluminum (Al2p) are presented in Figure 6.5a, b and c respectively. Plotting the counts versus binding energy for silicon reveals a main Si2p peak with 18.4 at% at 102.9 eV which is very close to the reported silicon peak in silica of 103.2-103.8 eV [35]. The slight shift towards lower binding energies in the measured sample is caused by an overcompensation of positive charges when photoelectrons are removed from an isolating sample. The oxygen O1s curve can be fitted to two peaks with binding energies of 532.3 eV and an amount of 41.5 at%, as well as 531.1 eV and an amount of 12.9 at%. These values correspond to oxygen reported in silica with an energy of 532.5-533.3 eV and in alumina of 530.0-531.8 eV [35]. The first peak at a higher energy with a bigger portion of oxygen is generated by the silica layer, while the second smaller peak is triggered by the amorphous alumina substrate underneath the Pt NPs and the silica layer. The support also gives rise to the detected aluminum Al2p peak with a binding energy of 74.5 eV and an amount of 17.0 at% which exists in the range of known Al2p peaks for alumina with binding energies ranging between 73.5 eV and 74.5 eV [35]. Thus, the formation of a pure silica layer by the colloidal particles obtained in this TEOS-based sol-gel synthesis without observing any impurities can be concluded in the XPS spectra. Also, the layer is assumed to be thin because of the detected amorphous alumina underneath the silica layer.

Lastly, the arrangement of the Pt NPs and the silica particles was investigated in TEM. Cross sections of samples with immobilized platinum particles and a thin silica layer were imaged and are shown in Figure 6.6a and b. Dark round spots indicate the platinum nanoparticles with diameters of 5-6 nm on top of the amorphous alumina support. Also a thin irregular brighter strip with a size less than 5 nm when compared with the Pt NPs is observed which corresponds to the synthesized sol-gel silica layer. It does not cover the particles but instead can be seen to be deposited around them. Therefore, the conclusion can be drawn that the silica layer is not spread on top of the platinum nanoparticles and so the necessary active platinum sites should remain available for the catalytic reaction.

6.2.2 Sinter study of platinum nanoparticles isolated with silica layer

Afterwards, the isolated Pt NPs with a silica layer around them were tested in a sinter study at 750°C under atmospheric conditions and their resistance to nanoparticle coarsening was analyzed with SEM. In Figure 6.7, the resulting images are presented for time intervals of 0 h, 1 h, 2 h and 4 h. Pt NPs without a surrounding silia layer on amorphous alumina are taken as references to compare the sintering behavior with and without the SiO_2-isolation. Inlens-pictures of the silica-coated substrates reveal information about the surface with higher resolution at the nanometer-scale, while the SE2-ones of the same samples contain in-depth information about the material contrast since the detected BE-electrons have backscatter coefficients that correlate with the atomic number of the element [34]. Due to variations in BCML-synthesis, the interparticle distance varies between the different samples. Yet for the same time point, the samples with and without the silica layer always reveal similar particle density on the substrates prior to the heat treatment.

At 0 h the Pt NPs are regularly arranged in their quasi-hexagonal pattern on the references, as well as on the substrates with a SiO_2-layer in the Inlens- and SE2-images. In Inlens-mode the bigger brighter spots correspond to the Pt NPs while the smaller, coarse and darker ones present the silica colloids. To distinguish these further, the high-atomic-number element platinum is seen as bright points when analyzed with the SE2-detector and the light elements Si, O and Al from the layer and the substrate disappear in the background highlighting the hexagonal structure of the Pt NPs. After 1 h-heat treatment at 750°C, few platinum particles start to leave the regular structure on the reference sample. Since most other small particles remain in their original pattern, Ostwald ripening can be concluded to govern the sintering behavior of the Pt NPs on Al_2O_3(a), as also proven in chapter 4. In comparison, the silica coated samples disclose a more ordered Pt NP structure with almost all nanoparticles still in their intial positions. This enhanced sinter stability is clearly identified at the 2 h-time interval. While most of the nanoparticles on the reference sample disappeared and larger particles are formed, no such evidence is seen on the NP-sample with the silica isolation. Here, the vast majority of the Pt NPs stays in the hexagonal arrangement. Overall more nanoparticles appear which was caused by an initially reduced interparticle distance on both the silica isolated and the reference samples at 2 h. Lastly, at 4 h, this trend continues with a significant amount of approximately 60-70% of the originally sized small nanoparticles remaining on the amorphous alumina substrate when separated from each other with a SiO_2-layer. No obvious sintering can be detected on the samples. However, very big platinum particles of sizes ranging between 50 and 100 nm are visible on the references revealing nanoparticle coarsening without the protective silica layer in between the particles. Lu *et al.* attribute the reduced sintering rate of the isolated Pt NPs to a weaker bonding between the platinum and the surrounding silica layer which acts as an additional energy barrier, the Ehrlich-Schwoebel barrier. This SiO_2-layer causes a diminished diffusion and migration of the Pt NPs or platinum adatoms on their tested titania support [86].

TEM cross sections of annealed alumina samples with immobilized Pt NPs and a separating SiO_2-layer at 750°C for 2 h are displayed in Figure C.1 in Appendix C. The platinum nanoparticles are observed as dark points without having grown in size on the amorphous alumina. Additionally,

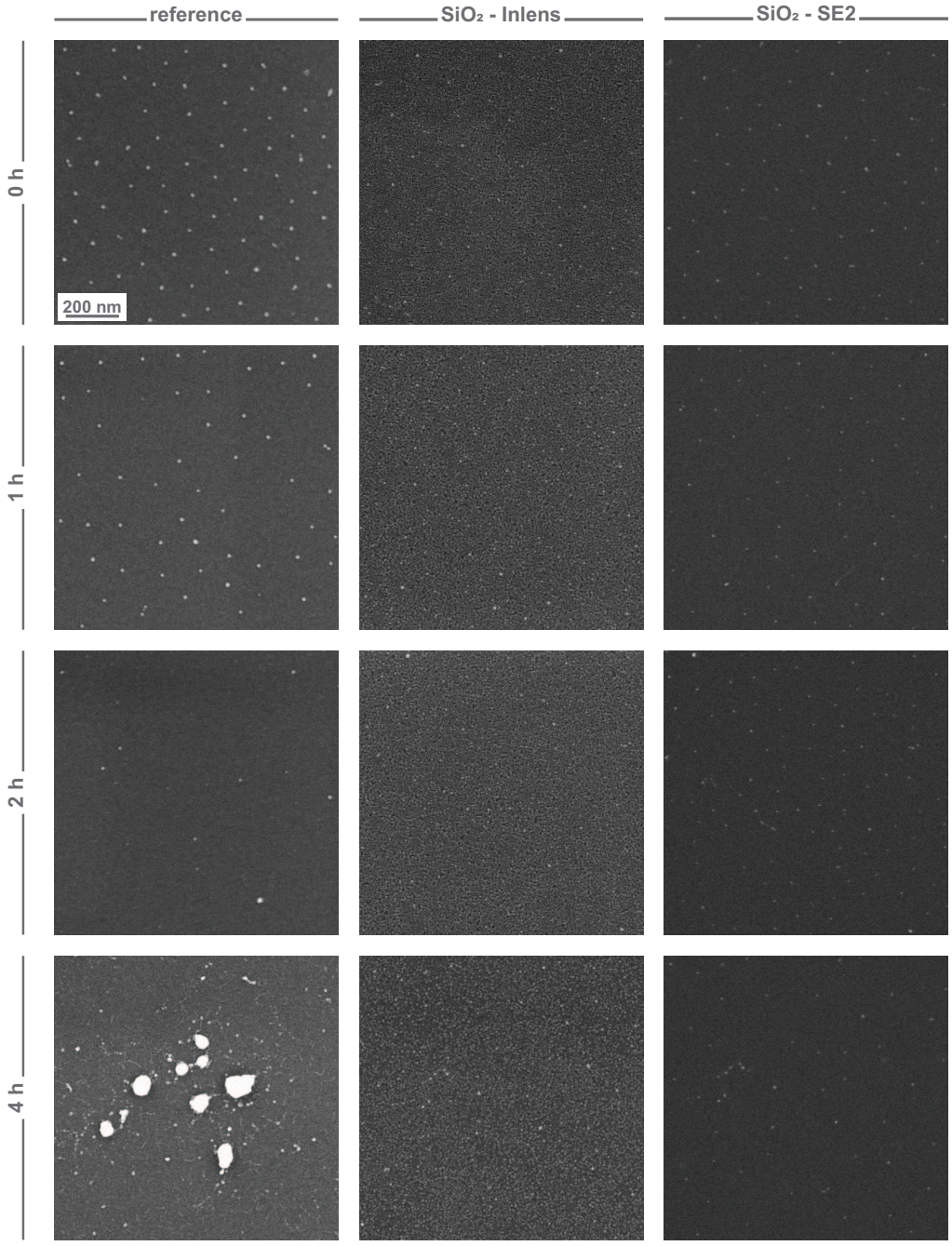

Figure 6.7: SEM images with different detectors of Pt NPs with and without an isolating silica layer during sinter studies in air at 750°C after different time periods. The first column presents the samples without the silica layer (references), obtained by the Inlens-detector. The second and the third columns show images of the samples with the silica layer obtained by the Inlens-detector for topographical information, and by the SE2-detector for material contrast information respectively. The scale bar in all SEM pictures represents 200 nm.

the thin layer composed of colloidal silica particles appears as a lighter band on the alumina and around the nanoparticles without showing coverage of these ones. Thus, it can be concluded that the silica layer does not, or only slightly, changes its morphology during the sinter process without an indication of interferring with the nanoparticles. These remain uncovered during the heat treatment.

Additionally, an attempt was made to test the catalytic activity of the isolated Pt NPs via the demonstration of an azo-bond hydrogenation in the dye methyl red (see Figure D.1 in Appendix D) with Ultraviolet-visible spectroscopy (UV-Vis), as reported by Briseno *et al.*, Dai *et al.* and Formo *et al.* [29, 43, 53]. Secondly, the reduction of *p*-nitrophenol (Figure D.3a in Appendix D) as a model reaction for catalytic activities of Pt NPs by Lu *et al.* was studied on the samples as well [86]. Yet due to an insufficient loading of Pt NPs, as identified by inductively coupled plasma optical emission spectroscopy (ICP-OES), no significant changes in UV-Vis spectra could be detected for both chemical reactions (Figure D.2 and D.3b in Appendix D). Even the sensitive CO adsorption method via calometry failed because of the extremely low Pt NP concentration on the substrates. Therefore, the catalytic activity could not be successfully measured for the nanoparticles.

Summarizing, the TEM cross sections revealed uncovered Pt NPs when a silica layer is deposited around the NPs to separate them from each other. Sinter studies at 750°C in air proved the increased stability against NP coarsening. Thus, the isolation of Pt NP with SiO_2 is a promising concept to create an improved sinter-stable exhaust combustion system.

6.3 Isolation of platinum nanoparticles via alumina layer

The Pt NPs were also isolated by a sol-gel-synthesized Al_2O_3-layer. This layer was characterized by focusing on particle size of alumina colloids in the sol. Additionally, the coating thickness, its composition and its deposition related to the nanoparticles were investigated. Later on, the coarsening of these nanoparticles was analyzed in a sinter study with SEM.

6.3.1 Characterization of alumina layer

The sol consisting of colloidal alumina particles was examined regarding its particle sizes with DLS. The resulting graph is shown in Figure 6.8 and reveals a formation of Al_2O_3-colloids with a hydrodynamic radius below 10 nm. Hereby, the majority of the particles were detected at a size below 4 nm. This yields an average diameter of 2.56 nm and a standard deviation of 2.41 nm. Since dirt easily contributes to measurement inaccuracies and since these particles are near the lower measurement range, the obtained DLS-data can only give an indication of the existing colloidal particle sizes. Yet, it can be concluded that tiny alumina nanoparticles contribute to the layer formation.

The thickness of the resulting dense layer was then measured with ellipsometry and is illustrated in Figure 6.9. Different concentrations of the alumina solution ranging from 0.01 mol/l to 0.1 mol/l were tested. The resulting layer thickness before and after a calcination step at 500°C

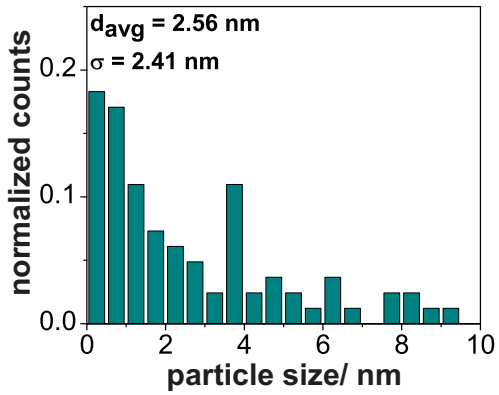

Figure 6.8: Characterization of particle sizes in alumina solution measured by DLS.

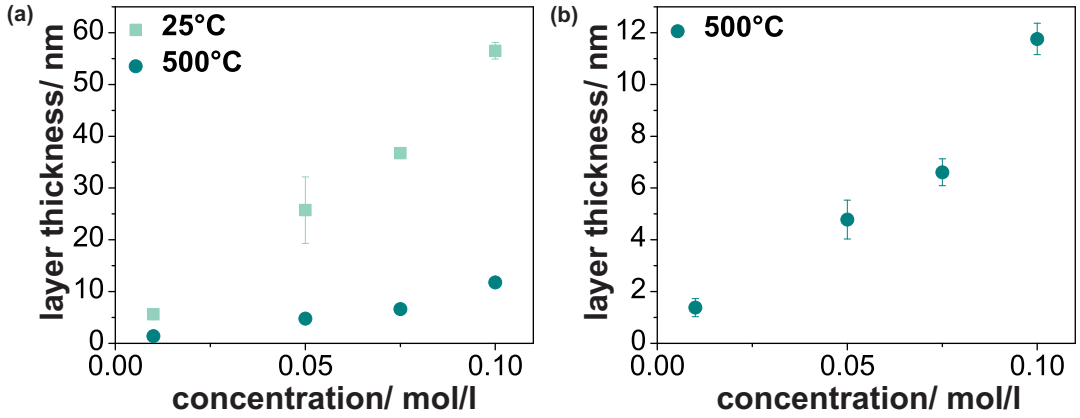

Figure 6.9: Layer thickness of 0.01-0.1 mol/l concentrated spin coated alumina solutions: (a) Comparison of the thickness before (25°C) and after (500°C) a 1 h-heat treatment at 500°C in air. (b) Inset of heat-treated samples regarding the correlation between layer thickness and concentration.

for 1 h is presented in the 25°C- and 500°C-curves in Figure 6.9a. For the samples without a following heat treatment a layer thickness of 5.62 ± 0.94 nm for 0.01 mol/l, 25.74 ± 6.41 nm for 0.05 mol/l, 36.75 ± 0.36 nm for 0.075 mol/l and 56.52 ± 1.6 nm for 0.1 mol/l was obtained. Thus, the spin coating of a higher concentrated sol linearly correlates with a thicker alumina layer afterwards. However, the heat treatment at 500°C for 1 h drastically reduces the layer thickness by approximately 80 % to 1.38 ± 0.35 nm for 0.01 mol/l, 4.78 ± 0.75 nm for 0.05 mol/l, 6.61 ± 0.52 nm for 0.075 mol/l and 11.76 ± 0.61 nm for 0.1 mol/l. For an improved illustration, these values are plotted additionally in Figure 6.9b. The linearly corresponding evolution of layer thickness with sol concentration also applies in this case. The detected shrinkage in thickness is induced by a combustion of the inclosed organic components including butoxide and the chelating agent. Therefore, the ASB-EAA-based sol-gel technique allows a fine tuning of the layer thickness. In initial tests the TEM cross sections of an alumina layer with a 0.075 mol/l-concentration and a thickness of 6-7 nm revealed completely covered nanoparticles. So, for further experiments, a sol concentration of 0.03 mol/l was used yielding an approximate alumina layer-thickness of 3 nm which is smaller than the 5-6 nm sized Pt NPs.

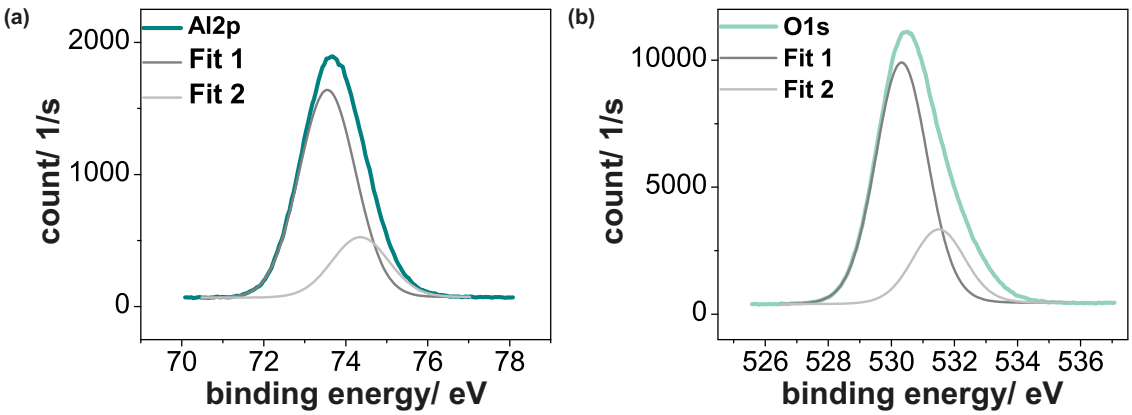

Figure 6.10: XPS-spectra of isolating alumina layer on silicon regarding (a) Al-peak and (b) O-peak to confirm Al_2O_3-formation.

The chemical composition of the isolating alumina layer on silicon was investigated with XPS. The obtained spectra of aluminum (Al2p) and oxygen (O1s) are shown in Figure 6.10a and b respectively. Hereby, the measured aluminum reveals a main Al2p peak at 73.6 eV with 30 at% and a minor peak at 74.4 eV with 8.7 at%. These fit exactly into the reported range of binding energies for aluminum in alumina with 73.5-74.5 eV [35]. Similarly, two oxygen O1s peaks exist with 40.9 at% at a binding energy of 530.3 eV and with 12.5 at% at 531.5 eV which fit to the reported oxygen O1s-spectra in alumina between 529.9 eV and 531.8 eV as well. Since a high concentration of alumina solution was used in this XPS measurement which resulted in a thick layer, no Si-peak could be detected.

Lastly, TEM cross sections of Pt NPs immobilized on amorphous alumina, Al_2O_3(a), which consists of a thick alumina layer deposited via PVD on a silicon wafer, and a 0.03 mol/l-sol derived isolating Al_2O_3-layer are presented in Figure 6.11. The dark spots mark the platinum nanoparticles, while a sligthly different grey band compared to the amorphous alumina support can be identified as the isolating Al_2O_3-layer. In both TEM images, the derived alumina layer is not on top of the Pt NPs since its height is visibly less than the nanoparticles. Thus, the platinum particles remain uncovered during the spin coating process of the alumina sol and the following calcination step.

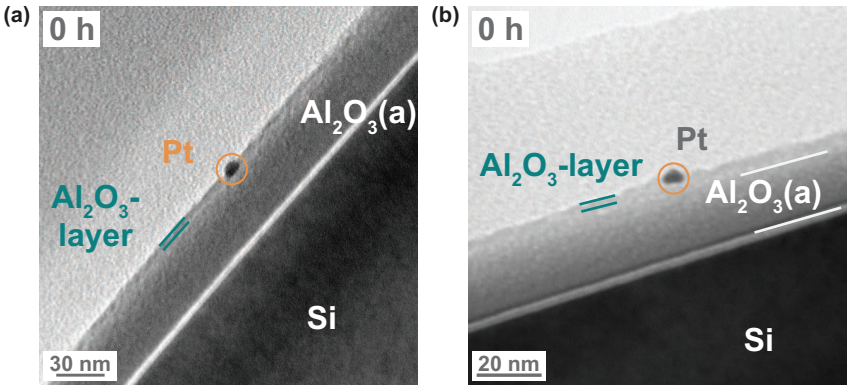

Figure 6.11: (a) and (b) Cross sections of isolated Pt NPs with an alumina layer in TEM.

6.3.2 Sinter study of platinum nanoparticles isolated with alumina layer

The sintering behavior of 5-6 nm Pt NPs with an isolating alumina layer was studied with SEM in Inlens- and SE2-mode and the obtained images are displayed in Figure 6.12. Comparable to the study with the silica layer, as in Figure 6.7, samples with the layers are compared to reference samples without regarding the arrangement and number of Pt NPs. At 0 h, the Pt NPs are regularly positioned in their quasi-hexagonal structure on the reference caused by the BCML-synthesis. This can also be seen for the samples with the alumina layer when analyzed with the SE2-detector, which allows the differentiation of platinum from the light elements aluminum and oxygen that are present in the alumina layer and the substrate underneath the particles. In the Inlens-picture, the Pt NPs are also explicitly visible, yet the alumina layer structure causes a highly nonuniform and disturbed background. As it appears, the layer has an irregular structure displaying circles of varying sizes which either indicate a hole or a thinner area of sol-gel derived and deposited Al_2O_3. Also, the interparticle distance between the Pt NPs on the two samples with alumina layer at 0 h and 1 h are diminished in comparison with the ones on the reference. This phenomenon is caused by unpreventable differences in spin coating of the Pt NP-BCML-solution, yet it does not interfere with the sinter study. On the contrary, closer NPs are subject to an increased coarsening behavior.

After 1 h at 750°C, few nanoparticles start to disappear on the references, similar to the ones in the sinter study with the silica layer as in chapter 6.2.2. This is also induced by an Ostwald ripening process where platinum adatoms or clusters preferentially leave smaller nanoparticles and diffuse over the surface until they reach bigger ones. However, no bigger particles are detected at this time point. In comparison, the Pt NPs with an isolating alumina layer around them do not seem to be influenced by the heat treatment because all of them remain in their original positions without an indication of nanoparticle or cluster migration, as seen in the SE2-picture. After 1 h, no circular spots of the alumina are visible in the Inlens-mode anymore suggesting a uniform thin layer without irregularities. In contrast, the layer visibly begins to coarsen again at the 2 h-time interval and continues to do so at 4 h where big holes appear. This is triggered by a morphological transfomation of the thin Al_2O_3-layer at these high temperatures. Though the layer undergoes a reconstruction process, the platinum nanoparticles are left uncovered in TEM cross sections of samples annealed at 750°C for 2 h. The TEM images are shown in Figure C.2a and b in Appendix C. Hence, the layer does not grow in size or on top of the particles. This would hinder their catalytic activity which again could not be analyzed due to the limited Pt NP loading as explained in chapter 6.2.2. However, during the SEM-sinter study, the Pt NPs on the samples with an alumina layer remain unaffected by its morphological changes and at 2 h, a large majority of Pt NPs are found in the initial pattern with similar interparticle distances as on the references. No indication of NP coarsening can be drawn and the branch of NPs on the bottom right corner in this picture was generated by variations in micelle deposition during the BCML-synthesis. On the 2 h-reference sample, an increasing number of platinum particles is missing while one of them is enlarged due to NP sintering. Lastly, at 4 h, almost none of the original 5-6 nm Pt NPs on the reference samples are visible anymore but large clustered particles with sizes between 50 nm and 100 nm are detected. If the nanoparticles are separated from each other with a 3 nm alumina layer, a majority of these, approximately 80-90 %, remain in their original spots and no bigger Pt

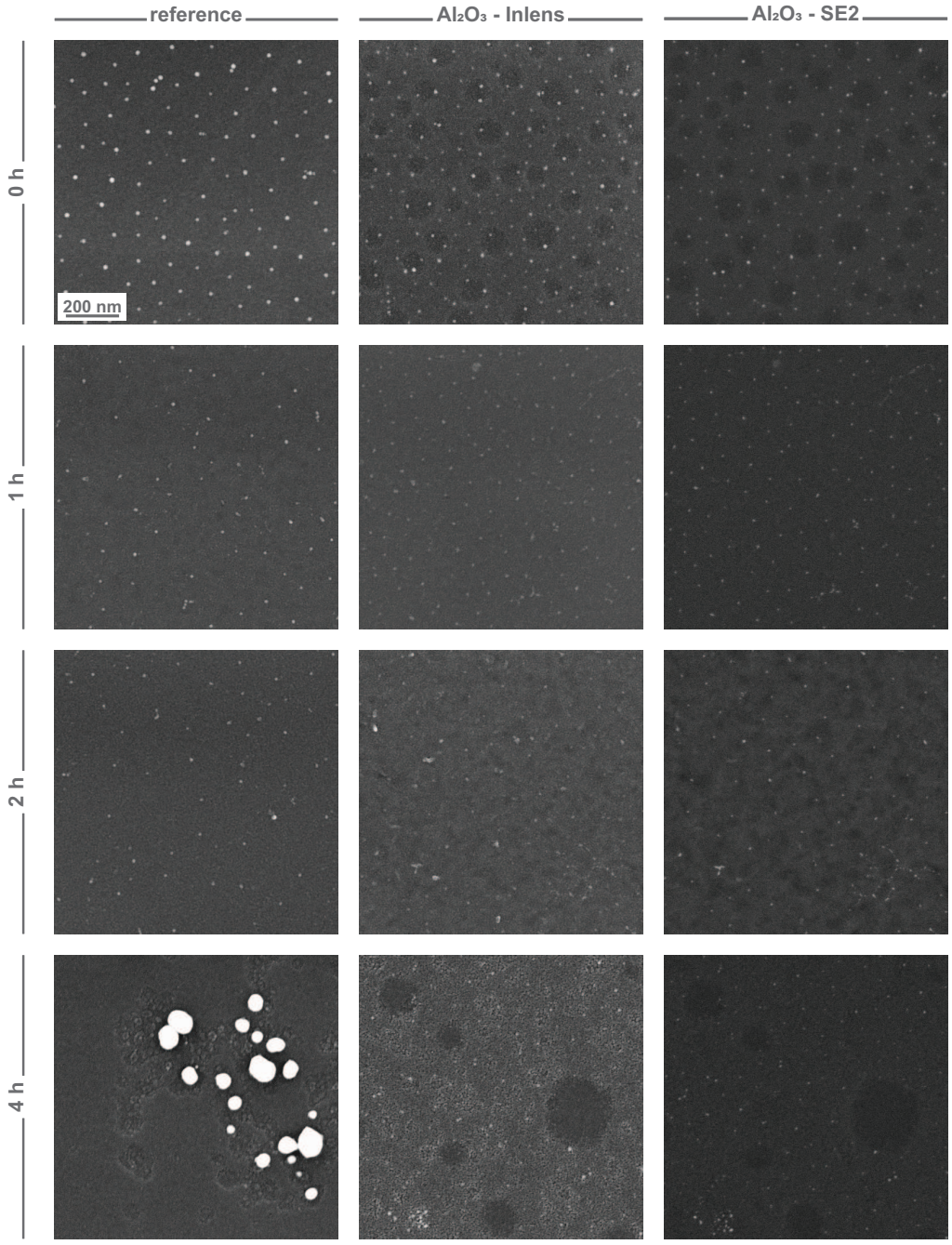

Figure 6.12: SEM images with different detectors of Pt NPs with and without an isolating alumina layer during sinter studies in air at 750°C after different time periods. The first column presents the samples without the alumina layer (references), obtained by the Inlens-detector. The second and the third columns show images of the samples with the alumina layer obtained by the Inlens-detector for topographical information, and by the SE2-detector for material contrast information respectively. The scale bar in all SEM pictures represents 200 nm.

NPs are formed. Interestingly, the small platinum nanoparticles all disappear when this alumina layer is destroyed as it can be seen in the holes of the Inlens- and the corresponding SE2-images at the 4 h time point. This proves that the sol-gel derived alumina layer successfully prevents a coarsening of Pt NPs and enables the establishment of an improved sinter-stable system.

6.4 Summary

In this chapter, the goal was to isolate Pt NPs from each other by depositing a thin oxide layer around the particles in order to increase their coarsening resistance by hindering surface diffusion of platinum clusters or whole particles. First, nanoparticles were separated via a silica layer derived from a TEOS-based sol-gel synthesis. AFM allowed the characterization of the sol and revealed a growth in colloidal silica particle sizes upon aging time which was not seen for the following sol of alumina in the second layer system. An XPS study confirmed the formation of only SiO_2 in the silica layer without impurities or side products and cross sections of immobilized Pt NPs with the silica layer in TEM showed that the particles remain uncovered during the spin coating process of the sol. Thus, their catalytic activity should only be minorly affected by the silica. This could not be analyzed by the model reactions of methyl-red hydrogenation or *p*-nitrophenol due to an insufficient platinum loading which did not yield detectable changes in absorbance measured with UV-vis (Appendix D). In a subsequent sinter study, only few nanoparticles disappeared from their original position during a 4 h-heat treatment at 750°C when separated from each other by the silica layer while a large majority of approximately 60-70 % did not show any indications for sintering. However, when matched to reference samples without the SiO_2-layer, considerable sintering could be seen on these ones by the appearance of large clustered Pt NPs.

Secondly, an alumina layer was deposited on the samples with Pt NPs and investigated in comparison with the silica-one. DLS measurements demonstrated that the synthesized sol consists of tiny alumina colloids with sizes mainly below 4 nm and layers manufactured out of these are linearly correlated to the sol concentration. Thus, a 3 nm-thick alumina layer consisting of Al_2O_3 without impurities, as tested in XPS, was used for further experiments which did not cover up the Pt NPs, as proven by the TEM cross sections. During a sinter study at 750°C in air, a large majority with approximately 80-90 % of the platinum particles remained in their initial quasi-hexagonal arrangement and sintering only occurred in the places where the isolating alumina layer was destroyed due to morphological reconstruction at high temperatures.

Consequentially, both the silica and the alumina layer successfully separate the Pt NPs from each other and significantly slow down the sintering rate when compared to samples without these protecting films. Since only a minor difference in NP coarsening could be observed in the sinter studies with SiO_2 and Al_2O_3, the layers act as Ehrlich-Schwoebel barrier independent of their composition hindering the diffusion of platinum adatoms, clusters or whole particles on the underlying support surface. Thus, an isolating oxide layer around the catalytic active nanoparticles is a promising concept to create sinter-stable exhaust combustion systems.

7 Conclusion

To investigate the thermal stability of platinum nanoparticles in modern car converters, model systems with lower complexity have been used in this PhD thesis. The sintering behavior of 5-6 nm Pt NPs, synthesized via BCML, was studied on both crystalline and amorphous silica and alumina substrates with SEM and AFM. Additionally, the influence of individual parameters on the NP's thermal stability could be independently analyzed and characterized.

Sinter studies at 750°C under atmospheric conditions for 60 min revealed fast coarsening of the Pt NPs on the crystalline substrates with a quick loss of their original quasi-hexagonal pattern. Here, PMC was the dominant sintering mechanism. In contrast, Pt NPs on amorphous substrates remained in their initial arrangement for longer times. In addition, the appearance of very small particles proposes OR to govern the sintering behavior on these supports; however, amorphous alumina displayed three times higher thermal stability compared to the other tested substrates. As key parameters, the surface adhesion of Pt NPs, substrate roughness, surface potential and energy were investigated by LFM, AFM, AM-KPFM and contact angle measurements. Pt NPs were attached more strongly to the amorphous substrates than on the crystalline supports, especially after a heat treatment at 750°C. This gave rise to an almost twofold increase in nanoparticle adhesion; thus, a stronger adhesion tends to slow down the sintering by impacting the OR process through an advanced Pt NP immobilization. However, one of the main contributing factors impacting the sintering stability of the nanoparticles is the surface roughness of the amorphous alumina, which was approximately three times greater on amorphous alumina when compared to crystalline alumina and the two tested silica-samples. Additionally, the surface potential was found to also have a considerably higher value on amorphous alumina and as such, a greater reactivity of the alumina with the Pt NPs is suggested when compared to the other substrates. Lastly, a low contact angle of water on the crystalline supports correlates well with a more distinct wetting of platinum. Therefore, a higher surface diffusion of whole Pt NPs was hypothesized for PMC which governs NP coarsening on these crystalline supports. In sum, the increased surface roughness and the higher surface potential of the substrate underneath the catalytically active Pt NPs are two dominant factors for governing their sintering behavior, while NP adhesion and surface energy of the support play an important role in the sintering mechanism.

Furthermore, the Pt NPs were tested on structured surfaces composed of an amorphous alumina- and silica-side during heat treatments in air at 750°C with a focus on the behavior at the interface between these two materials. NPs situated on the silica were generally faster to grow into larger particles and also showed directional migration with a following accumulation towards and at the interface, which acts as an Ehrlich-Schwoebel barrier. Later on, Pt NPs were also observed to cross over the border and could be detected on the alumina-section. Alternatively, when Pt NPs were placed on the amorphous alumina-side with an increased sinter stability and an

interface towards amorphous silica, the NPs remained unaltered until much later time points due to slower coarsening. No diffused NPs could be detected on the silica-section at any time with the NPs remaining on the alumina-side. Thus, it appears that Pt NPs favor the high metal interaction alumina substrate with the above tested characteristics over the low metal interaction silica substrate, thereby revealing the influence of compositional structuring on the coarsening behavior of Pt NPs.

Afterwards, the impact of structural heterogeneities on the thermal stability of the Pt NPs was examined with differently tilted *c*-plane (0001) sapphire wafers. They showed increasing step heights and overall decreasing step sizes for more tilted substrates in AFM-measurements. In a sinter study under atmospheric conditions at 750°C, very fast NP coarsening via PMC was observed due to a proposed volatile platinum oxide formation without a distinct variation in NP behavior on the 0.1°, 4° and 9°-tilted substrates. Slowing down the sintering rate in the absence of oxygen, a second sinter study performed under vacuum at 1200°C showed a smaller increase in average diameter of the sintered platinum clusters for the more tilted-sapphire wafers compared to the flatter ones. Accordingly, the majority of the large sintered particles could be detected at the step edges where a significant drop in surface potential was measured when crossing over it in FM-KPFM-measurements. Also, the edges function as Ehrlich-Schwoebel barriers, thus hindering the migration and diffusion of the particles; so the positive influence of surface structuring consisting of different height irregularities on the coarsening behavior of Pt NPs could be identified.

Lastly, the sinter resistance of Pt NPs on amorphous alumina was successfully increased by the deposition of an isolating silica or alumina layer between them by simple sol-gel techniques. These films hindered the surface diffusion of platinum clusters or whole particles from migrating towards each other. Sinter studies at 750°C under atmospheric conditions demonstrated no obvious indications for particle coarsening over a 4 h-time period for the NPs with either separating layer when compared to reference samples without the silica- or alumina-protection. While TEM cross sections showed that the particles were uncovered by the thin layers, the sintering could be significantly reduced using these approaches. Independent of their composition, the diffusion of Pt clusters could be decelerated.

Thus, an isolating oxide layer around the catalytically active nanoparticles on amorphous alumina with a high substrate roughness, NP adhesion and surface potential compared to the other three tested substrates is a promising concept to create sinter-stable exhaust combustion systems. Implementing these promising findings from the model system to an industrially relevant scale will be the next step. This would then reduce the amount of costly and harmful Pt NPs while maintaining a high activity in order to fulfill upcoming strict regulations on exhaust standards, as well as to lower the health risks in high population density areas with an increasing number of cars.

Bibliography

[1] Severin Amelinckx, Dirk Van Dyck, J Van Landuyt, and Gustaaf Van Tendeloo. *Electron microscopy: principles and fundamentals*. John Wiley and Sons, 2008.

[2] Kwangjin An and GaborA Somorjai. Nanocatalysis I: Synthesis of metal and bimetallic nanoparticles and porous oxides and their catalytic reaction studies. *Catalysis Letters*, 145(1):233–248, 2015.

[3] Tomohiro Aoyama, Masayasu Nagoshi, Hideki Nagano, Kaoru Sato, and Shigeaki Tachibana. Selective backscattered electron imaging of material and channeling contrast in microstructures of scale on low carbon steel controlled by accelerating voltage and take-off angle. *ISIJ International*, 51(9):1487–1491, 2011.

[4] Daniel Arcos and Maria Vallet-Regi. Sol-gel silica-based biomaterials and bone tissue regeneration. *Acta Biomaterialia*, 6(8):2874–2888, 2010.

[5] Pablo M. Arnal, Massimiliano Comotti, and Ferdi Schueth. High-temperature-stable catalysts by hollow sphere encapsulation. *Angewandte Chemie*, 118(48):8404–8407, 2006.

[6] M. A. Asoro, D. Kovar, Y. Shao-Horn, L. F. Allard, and P. J. Ferreira. Coalescence and sintering of pt nanoparticles: in situ observation by aberration-corrected haadf stem. *Nanotechnology*, 21(2):025701, 2010.

[7] Didier Astruc, Feng Lu, and Jaime Ruiz Aranzaes. Nanopartikel als regenerierbare Katalysatoren: an der Nahtstelle zwischen homogener und heterogener Katalyse. *Angewandte Chemie*, 117(48):8062–8083, 2005.

[8] David Avnir, Sergei Braun, Ovadia Lev, and Michael Ottolenghi. Enzymes and other proteins entrapped in sol-gel materials. *Chemistry of Materials*, 6(10):1605–1614, 1994.

[9] Florence Babonneau, Laure Coury, and Jacques Livage. Aluminum sec-butoxide modified with ethylacetoacetate: An attractive precursor for the sol-gel synthesis of ceramics. *Journal of Non-Crystalline Solids*, 121(1):153–157, 1990.

[10] Chunli Bai and Minghua Liu. From chemistry to nanoscience: Not just a matter of size. *Angewandte Chemie International Edition*, 52(10):2678–2683, 2013.

[11] L. Robert Baker, Griffin Kennedy, Matthijs Van Spronsen, Antoine Hervier, Xiaojun Cai, Shiyou Chen, Lin-Wang Wang, and Gabor A. Somorjai. Furfuraldehyde hydrogenation on titanium oxide-supported platinum nanoparticles studied by sum frequency generation vibrational spectroscopy: Acid-base catalysis explains the molecular origin of strong metal-support interactions. *Journal of the American Chemical Society*, 134(34):14208–14216, 2012.

[12] R. T. K. Baker. The relationship between particle motion on a graphite surface and tammann temperature. *Journal of Catalysis*, 78(2):473–476, 1982.

[13] R. T. K. Baker, E. B. Prestridge, and R. L. Garten. Electron microscopy of supported metal particles. *Journal of Catalysis*, 56(3):390–406, 1979.

[14] A. Baldan. Review progress in ostwald ripening theories and their applications to nickel-base superalloys part I: Ostwald ripening theories. *Journal of Materials Science*, 37(11):2171–2202, 2002.

[15] Calvin H. Bartholomew. *Sintering Kinetics of Supported Metals: Perspectives from a Generalized Power Law Approach*, volume Volume 88, pages 1–18. Elsevier, 1994.

[16] Calvin H. Bartholomew. Mechanisms of catalyst deactivation. *Applied Catalysis A: General*, 212(1-2):17–60, 2001.

[17] Ernst Bauer. Phaenomenologische Theorie der Kristallabscheidung an Oberflaechen. *Zeitschrift fuer Kristallographie-Crystalline Materials*, 110(1-6):372–394, 1958.

[18] Aldona Beganskiene, Valdas Sirutkaitis, Maryte Kurtinaitiene, Remigijus Juskenas, and Aivaras Kareiva. FTIR, TEM and NMR investigations of Stoeber silica nanoparticles. *Mater Sci (Medziagotyra)*, 10:287–290, 2004.

[19] F. Behafarid and B. Roldan Cuenya. Towards the understanding of sintering phenomena at the nanoscale: Geometric and environmental effects. *Topics in Catalysis*, 56(15):1542–1559, 2013.

[20] Alexis T. Bell. The impact of nanoscience on heterogeneous catalysis. *Science*, 299(5613):1688–1691, 2003.

[21] Angelica D. Benavidez, Libor Kovarik, Arda Genc, Nitin Agrawal, Elin M. Larsson, Thomas W. Hansen, Ayman M. Karim, and Abhaya K. Datye. Environmental transmission electron microscopy study of the origins of anomalous particle size distributions in supported metal catalysts. *ACS Catalysis*, 2(11):2349–2356, 2012.

[22] Parthasarathi Bera, Arup Gayen, M. S. Hegde, N. P. Lalla, Lorenzo Spadaro, Francesco Frusteri, and Francesco Arena. Promoting effect of CeO2 in combustion synthesized Pt/CeO2 catalyst for CO oxidation. *The Journal of Physical Chemistry B*, 107(25):6122–6130, 2003.

[23] Abhijit Biswas, Ilker S. Bayer, Alexandru S. Biris, Tao Wang, Enkeleda Dervishi, and Franz Faupel. Advances in top-down and bottom-up surface nanofabrication: Techniques, applications and future prospects. *Advances in Colloid and Interface Science*, 170(1-2):2–27, 2012.

[24] J. M. Blakely and H. Mykura. Surface self diffusion and surface energy measurements on platinum by the multiple scratch method. *Acta Metallurgica*, 10(5):565–572, 1962.

[25] David Brandon and Wayne D Kaplan. *Microstructural characterization of materials*. John Wiley and Sons, 2013.

[26] D. Briggs and M.P. Seah. *Practical Surface Analysis, Auger and X-ray Photoelectron Spectroscopy*. Wiley, 1990.

[27] P. Brijesh and S. Sreedhara. Exhaust emissions and its control methods in compression ignition engines: A review. *International Journal of Automotive Technology*, 14(2):195–206, 2013.

[28] Clemens Brinkmeier, Gerhart Eigenberger, Jens Bernnat, Ute Tuttlies, Volker Schmeisser, and Frank Opferkuch. Autoabgasreinigung - eine Herausforderung fuer die Verfahrenstechnik. *Chemie Ingenieur Technik*, 77(9):1333–1355, 2005.

[29] Alejandro L. Briseno, Stefan C. B. Mannsfeld, Eric Formo, Yujie Xiong, Xianmao Lu, Zhenan Bao, Samson A. Jenekhe, and Younan Xia. Adding new functions to organic semiconductor nanowires by assembling metal nanoparticles onto their surfaces. *Journal of Materials Chemistry*, 18(44):5395–5398, 2008.

[30] Albert Bruix, Jose A. Rodriguez, Pedro J. Ramirez, Sanjaya D. Senanayake, Jaime Evans, Joon B. Park, Dario Stacchiola, Ping Liu, Jan Hrbek, and Francesc Illas. A new type of strong metal-support interaction and the production of H2 through the transformation of water on Pt/CeO2(111) and Pt/CeOx/TiO2(110) catalysts. *Journal of the American Chemical Society*, 134(21):8968–8974, 2012.

[31] AM Buckley and M Greenblatt. The sol-gel preparation of silica gels. *J. Chem. Educ*, 71(7):599, 1994.

[32] Charles T. Campbell. Ultrathin metal films and particles on oxide surfaces: structural, electronic and chemisorptive properties. *Surface Science Reports*, 27(1):1–111, 1997.

[33] Anmin Cao, Rongwen Lu, and Goetz Veser. Stabilizing metal nanoparticles for heterogeneous catalysis. *Physical Chemistry Chemical Physics*, 12(41):13499–13510, 2010.

[34] Zeiss NTS GmbH Carl. Handbuch fuer die Rasterelektronenmikroskope SUPRA(VP) und ULTRA. 2004.

[35] Jill Chastain, Roger C King, and JF Moulder. *Handbook of X-ray photoelectron spectroscopy: a reference book of standard spectra for identification and interpretation of XPS data*. Physical Electronics Eden Prairie, MN, 1995.

[36] Guangxu Chen, Huayan Yang, Binghui Wu, Yanping Zheng, and Nanfeng Zheng. Supported monodisperse Pt nanoparticles from [Pt3(CO)3(2-CO)3]52-clusters for investigating support-Pt interface effect in catalysis. *Dalton Transactions*, 42(35):12699–12705, 2013.

[37] Sung-Seen Choi, Seung Goo Lee, Seung Soon Im, Seong Hun Kim, and Yong L Joo. Silica nanofibers from electrospinning/sol-gel process. *Journal of Materials Science Letters*, 22(12):891–893, 2003.

[38] B. Chu. *Dynamic Light Scattering*, pages 335–372. Springer Netherlands, Dordrecht, 2008.

[39] Li Chunzeng, Minne Stephen, Hu Yan, Ma Ji, He Jianli, Mittel Henry, Kelly Vinson, Erina Natalia, Guo Senli, and Mueller Thomas. PeakForce Kelvin Probe Force Microscopy. *Bruker Nano Surfaces www. bruker.com*, Application Note 140.

[40] MD Craven, SH Lim, F Wu, JS Speck, and SP DenBaars. Structural characterization of nonpolar (1120) a-plane gan thin films grown on (1102) r-plane sapphire. *Applied physics letters*, 81(3):469–471, 2002.

[41] Beatriz Roldan Cuenya. Synthesis and catalytic properties of metal nanoparticles: Size, shape, support, composition, and oxidation state effects. *Thin Solid Films*, 518(12):3127–3150, 2010.

[42] Beatriz Roldan Cuenya and Farzad Behafarid. Nanocatalysis: size- and shape-dependent chemisorption and catalytic reactivity. *Surface Science Reports*, 70(2):135–187, 2015.

[43] Yunqian Dai, Byungkwon Lim, Yong Yang, Claire M. Cobley, Weiyang Li, Eun Chul Cho, Benjamin Grayson, Paul T. Fanson, Charles T. Campbell, Yueming Sun, and Younan Xia. A sinter-resistant catalytic system based on platinum nanoparticles supported on TiO2 nanofibers and covered by porous silica. *Angewandte Chemie*, 122(44):8341–8344, 2010.

[44] Abhaya K. Datye, Qing Xu, Karl C. Kharas, and Jon M. McCarty. Particle size distributions in heterogeneous catalysts: What do they tell us about the sintering mechanism? *Catalysis Today*, 111(1-2):59–67, 2006.

[45] Poelman Dirk and Smet Philippe Frederic. Methods for the determination of the optical constants of thin films from single transmission measurements: a critical review. *Journal of Physics D: Applied Physics*, 36(15):1850, 2003.

[46] Elena R. Dobrovinskaya, Leonid A. Lytvynov, and Valerian Pishchik. *Properties of Sapphire*, pages 55–176. Springer US, Boston, MA, 2009.

[47] Peter Eaton and Paul West. *Atomic force microscopy*. Oxford University Press, 2010.

[48] Gert Ehrlich and F. G. Hudda. Atomic view of surface self-diffusion: Tungsten on tungsten. *The Journal of Chemical Physics*, 44(3):1039–1049, 1966.

[49] Mirjam Eisele. Abscheidung von SiO2 auf Keramik-Substraten. *Diploma Thesis, University of Stuttgart*, 2013.

[50] Aaron S. Eppler, Guenther Rupprechter, Erik A. Anderson, and Gabor A. Somorjai. Thermal and chemical stability and adhesion strength of Pt nanoparticle arrays supported on silica studied by transmission electron microscopy and atomic force microscopy. *The Journal of Physical Chemistry B*, 104(31):7286–7292, 2000.

[51] Hao Feng, Junling Lu, Peter C. Stair, and Jeffrey W. Elam. Alumina over-coating on Pd nanoparticle catalysts by atomic layer deposition: Enhanced stability and reactivity. *Catalysis Letters*, 141(4):512–517, 2011.

[52] Stephan Foerster and Thomas Plantenberg. Von selbstorganisierenden Polymeren zu Nanohybrid- und Biomaterialien. *Angewandte Chemie*, 114(5):712–739, 2002.

[53] Eric Formo, Eric Lee, Dean Campbell, and Younan Xia. Functionalization of electrospun TiO2 nanofibers with Pt nanoparticles and nanowires for catalytic applications. *Nano Letters*, 8(2):668–672, 2008.

[54] Atsushi Fukuoka, Jun-ichi Kimura, Tadashi Oshio, Yuzuru Sakamoto, and Masaru Ichikawa. Preferential oxidation of carbon monoxide catalyzed by platinum nanoparticles in mesoporous silica. *Journal of the American Chemical Society*, 129(33):10120–10125, 2007.

[55] Katarzyna M. Gadomska, Sebastian J. Lechner, and Joachim P. Spatz. Gold-nanoparticle-decorated glass microspheres. *Particle and Particle Systems Characterization*, 30(11):940–944, 2013.

[56] B. C. Gates. Supported metal clusters: Synthesis, structure, and catalysis. *Chemical Reviews*, 95(3):511–522, 1995.

[57] R. Glass, M. Arnold, J. Bluemmel, A. Kueller, M. Moeller, and J. P. Spatz. Micro-nanostructured interfaces fabricated by the use of inorganic block copolymer micellar monolayers as negative resist for electron-beam lithography. *Advanced Functional Materials*, 13(7):569–575, 2003.

[58] Helmut Goesmann and Claus Feldmann. Nanoparticulate functional materials. *Angewandte Chemie International Edition*, 49(8):1362–1395, 2010.

[59] Jean-Francois Gohy. *Block Copolymer Micelles*, pages 65–136. Springer Berlin Heidelberg, Berlin, Heidelberg, 2005.

[60] W. I. Goldburg. Dynamic light scattering. *American Journal of Physics*, 67(12):1152–1160, 1999.

[61] C. G. Granqvist and R. A. Buhrman. Size distributions for supported metal catalysts. *Journal of Catalysis*, 42(3):477–479, 1976.

[62] David B. Hall, Patrick Underhill, and John M. Torkelson. Spin coating of thin and ultrathin polymer films. *Polymer Engineering and Science*, 38(12):2039–2045, 1998.

[63] Song Han, Xiaolei Liu, and Chongwu Zhou. Template-free directional growth of single-walled carbon nanotubes on a- and r-plane sapphire. *Journal of the American Chemical Society*, 127(15):5294–5295, 2005.

[64] Wenhai Han and F Michael Serry. Force spectroscopy with the atomic force microscope. *Application Note www. agilent. com*, 2011.

[65] Thomas W. Hansen, Andrew T. DeLaRiva, Sivakumar R. Challa, and Abhaya K. Datye. Sintering of catalytic nanoparticles: Particle migration or ostwald ripening? *Accounts of Chemical Research*, 46(8):1720–1730, 2013.

[66] P. J. F. Harris. Growth and structure of supported metal catalyst particles. *International Materials Reviews*, 40(3):97–115, 1995.

[67] Uta Hejral, Patrick Muller, Olivier Balmes, Diego Pontoni, and Andreas Stierle. Tracking the shape-dependent sintering of platinum-rhodium model catalysts under operando conditions. *Nat Commun*, 7, 2016.

[68] Larry L Hench and Jon K West. The sol-gel process. *Chemical reviews*, 90(1):33–72, 1990.

[69] Arnim Henglein. Small-particle research: physicochemical properties of extremely small colloidal metal and semiconductor particles. *Chemical Reviews*, 89(8):1861–1873, 1989.

[70] Akio Hiraki. Low temperature reactions at Si/metal interfaces; what is going on at the interfaces? *Surface Science Reports*, 3(7):357–412, 1983.

[71] Chin-Pei Hwang and Chuin-Tih Yeh. Platinum-oxide species formed by oxidation of platinum crystallites supported on alumina. *Journal of Molecular Catalysis A: Chemical*, 112(2):295–302, 1996.

[72] Chin-Pei Hwang and Chuin-Tih Yeh. Platinum-oxide species formed on progressive oxidation of platinum crystallites supported on silica and silica-alumina. *Journal of Catalysis*, 182(1):48–55, 1999.

[73] Malvern Instruments. Dynamic light scattering: an introduction in 30 minutes. *Technical Note Malvern, MRK656-01*, pages 1–8, 2012.

[74] Sarah Jahn. Thermisches Verhalten mono- und bimetallischer Nanopartikel fuer die Katalyse. *PhD thesis, Ruprecht-Karls-Universitaet Heidelberg, Heidelberg*, 2015.

[75] Chun-Jiang Jia and Ferdi Schueth. Colloidal metal nanoparticles as a component of designed catalyst. *Physical Chemistry Chemical Physics*, 13(7):2457–2487, 2011.

[76] Sang Hoon Joo, Jeong Young Park, Chia-Kuang Tsung, Yusuke Yamada, Peidong Yang, and Gabor A. Somorjai. Thermally stable Pt/mesoporous silica core-shell nanocatalysts for high-temperature reactions. *Nat Mater*, 8(2):126–131, 2009.

[77] L. C. Klein. Sol-gel processing of ionic conductors. *Solid State Ionics*, 32:639–645, 1989.

[78] Nikolaus Knorr and Stefan Vinzelberg. Charge writing and detection by EFM and KPFM scanning probe techniques. *Microscopy and Analysis*, page 7, 2012.

[79] D. Y. Kwok and A. W. Neumann. Contact angle measurement and contact angle interpretation. *Advances in Colloid and Interface Science*, 81(3):167–249, 1999.

[80] Elin M. Larsson, Julien Millet, Stefan Gustafsson, Magnus Skoglundh, Vladimir P. Zhdanov, and Christoph Langhammer. Real time indirect nanoplasmonic in situ spectroscopy of catalyst nanoparticle sintering. *ACS Catalysis*, 2(2):238–245, 2012.

[81] Ilkeun Lee, Qiao Zhang, Jianping Ge, Yadong Yin, and Francisco Zaera. Encapsulation of supported Pt nanoparticles with mesoporous silica for increased catalyst stability. *Nano Research*, 4(1):115–123, 2011.

[82] I. M. Lifshitz and V. V. Slyozov. The kinetics of precipitation from supersaturated solid solutions. *Journal of Physics and Chemistry of Solids*, 19(1):35–50, 1961.

[83] Alan Lo and Rex T. Skodje. Kinetic and monte carlo models of thin film coarsening: Cross over from diffusion-coalescence to ostwald growth modes. *The Journal of Chemical Physics*, 112(4):1966–1974, 2000.

[84] Theobald Lohmueller, Daniel Aydin, Marco Schwieder, Christoph Morhard, Ilia Louban, Claudia Pacholski, and Joachim P. Spatz. Nanopatterning by block copolymer micelle nanolithography and bioinspired applications. *Biointerphases*, 6(1):MR1–MR12, 2011.

[85] Theobald Lohmueller, Eva Bock, and Joachim P. Spatz. Synthesis of quasi-hexagonal ordered arrays of metallic nanoparticles with tuneable particle size. *Advanced Materials*, 20(12):2297–2302, 2008.

[86] Ping Lu, Charles T. Campbell, and Younan Xia. A sinter-resistant catalytic system fabricated by maneuvering the selectivity of SiO2 deposition onto the TiO2 surface versus the Pt nanoparticle surface. *Nano Letters*, 13(10):4957–4962, 2013.

[87] Yu Lu, Yadong Yin, Brian T. Mayers, and Younan Xia. Modifying the surface properties of superparamagnetic iron oxide nanoparticles through a sol-gel approach. *Nano Letters*, 2(3):183–186, 2002.

[88] R. Ludeke. Electrical characterization of gate oxides by scanning probe microscopies. *Journal of Non-Crystalline Solids*, 303(1):150–161, 2002.

[89] Zhen Ma, Suree Brown, Jane Y. Howe, Steven H. Overbury, and Sheng Dai. Surface modification of Au/TiO2 catalysts by SiO2 via atomic layer deposition. *The Journal of Physical Chemistry C*, 112(25):9448–9457, 2008.

[90] T Matsuoka and E Hagiwara. Gan growth on novel lattice-matching substrate: Tilted m-plane sapphire. *physica status solidi (a)*, 188(2):485–489, 2001.

[91] Teuvo Maunula, Yoshiaki Kintaichi, Megumu Inaba, Masaaki Haneda, Kazuhito Sato, and Hideaki Hamada. Enhanced activity of In and Ga-supported sol-gel alumina catalysts for NO reduction by hydrocarbons in lean conditions. *Applied Catalysis B: Environmental*, 15(3):291–304, 1998.

[92] Wilhelm Melitz, Jian Shen, Andrew C. Kummel, and Sangyeob Lee. Kelvin probe force microscopy and its application. *Surface Science Reports*, 66(1):1–27, 2011.

[93] Stefan Moessmer, Joachim P. Spatz, Martin Moeller, Thomas Aberle, Juergen Schmidt, and Walther Burchard. Solution behavior of poly(styrene)-block-poly(2-vinylpyridine) micelles containing gold nanoparticles. *Macromolecules*, 33(13):4791–4798, 2000.

[94] Michael D. Morse. Clusters of transition-metal atoms. *Chemical Reviews*, 86(6):1049–1109, 1986.

[95] Dale E Morton, Blaine Johs, and Jeff Hale. Optical monitoring of thin films using spectroscopic ellipsometry. In *Proceedings of the annual technical conference-society of vacuum coaters*, pages 299–305.

[96] A. Z. Moshfegh. Nanoparticle catalysts. *Journal of Physics D: Applied Physics*, 42(23):233001, 2009.

[97] J. A. Moulijn, A. E. van Diepen, and F. Kapteijn. Catalyst deactivation: is it predictable?: What to do? *Applied Catalysis A: General*, 212(1-2):3–16, 2001.

[98] Yasutaka Nagai, Takeshi Hirabayashi, Kazuhiko Dohmae, Nobuyuki Takagi, Takashi Minami, Hirofumi Shinjoh, and Shin'ichi Matsumoto. Sintering inhibition mechanism of platinum supported on ceria-based oxide and Pt-oxide-support interaction. *Journal of Catalysis*, 242(1):103–109, 2006.

[99] Radha Narayanan and Mostafa A. El-Sayed. Catalysis with transition metal nanoparticles in colloidal solution: Nanoparticle shape dependence and stability. *The Journal of Physical Chemistry B*, 109(26):12663–12676, 2005.

[100] Ruediger Nass and Helmut Schmidt. Proceedings of the fifth international workshop on glasses and ceramics from gels synthesis of an alumina coating from chelated aluminium alkoxides. *Journal of Non-Crystalline Solids*, 121(1):329–333, 1990.

[101] AW Neumann and RJ Good. *Techniques of measuring contact angles*, pages 31–91. Springer, 1979.

[102] M. Nonnenmacher, M. P. O Boyle, and H. K. Wickramasinghe. Kelvin probe force microscopy. *Applied Physics Letters*, 58(25):2921–2923, 1991.

[103] G. M. Pajonk. Aerogel catalysts. *Applied Catalysis*, 72(2):217–266, 1991.

[104] Sung Hyun Park, Dae Young Moon, and Jin Sub Park. Effects of r-plane sapphire substrate tilt angles on the growth behavior of nonpolar a-plane gan. *Journal of the Korean Physical Society*, 58(41):906–910, 2011.

[105] Stephen C. Parker and Charles T. Campbell. Kinetic model for sintering of supported metal particles with improved size-dependent energetics and applications to Au on TiO2(110). *Physical Review B*, 75(3):035430, 2007.

[106] R. Pecora. *Basic Concepts - Scattering and Time Correlation Functions*, pages 2–40. Springer Netherlands, Dordrecht, 2008.

[107] Richard D. Piner and Chad A. Mirkin. Effect of water on lateral force microscopy in air. *Langmuir*, 13(26):6864–6868, 1997.

[108] Soeren Porsgaard, Lindsay R. Merte, Luis K. Ono, Farzad Behafarid, Jeronimo Matos, Stig Helveg, Miquel Salmeron, Beatriz Roldan Cuenya, and Flemming Besenbacher. Stability of platinum nanoparticles supported on SiO2/Si(111): a high-pressure x-ray photoelectron spectroscopy study. *ACS Nano*, 6(12):10743–10749, 2012.

[109] Z. H. Qin, M. Lewandowski, Y. N. Sun, S. Shaikhutdinov, and H. J. Freund. Encapsulation of Pt nanoparticles as a result of Strong Metal-Support Interaction with Fe3O4 (111). *The Journal of Physical Chemistry C*, 112(27):10209–10213, 2008.

[110] C.N.R. Rao and Kanishka Biswas. Characterization of nanomaterials by physical methods. *Annual Review of Analytical Chemistry*, 2(1):435–462, 2009.

[111] Buddy D Ratner, Allan S Hoffman, Frederick J Schoen, and Jack E Lemons. *Biomaterials science: an introduction to materials in medicine*. Academic press, 2004.

[112] R. M. Rioux, H. Song, M. Grass, S. Habas, K. Niesz, J. D. Hoefelmeyer, P. Yang, and G. A. Somorjai. Monodisperse platinum nanoparticles of well-defined shape; synthesis, characterization, catalytic properties and future prospects. *Topics in Catalysis*, 39(3-4):167–174, 2006.

[113] R. M. Rioux, H. Song, J. D. Hoefelmeyer, P. Yang, and G. A. Somorjai. High-surface-area catalyst design synthesis, characterization, and reaction studies of platinum nanoparticles

in mesoporous SBA-15 silica. *The Journal of Physical Chemistry B*, 109(6):2192–2202, 2005.

[114] Emil Roduner. Size matters: why nanomaterials are different. *Chemical Society Reviews*, 35(7):583–592, 2006.

[115] Hyun-Seog Roh, Ki-Won Jun, Wen-Sheng Dong, Sang-Eon Park, and Yung-Il Joe. Partial oxidation of methane over Ni/Al2O3 catalysts. *Chemistry Letters*, 30(7):666–667, 2001.

[116] Jason H. Rouse and Gregory S. Ferguson. Preparation of thin silica films with controlled thickness and tunable refractive index. *Journal of the American Chemical Society*, 125(50):15529–15536, 2003.

[117] E. Ruckenstein and B. Pulvermacher. Growth kinetics and the size distributions of supported metal crystallites. *Journal of Catalysis*, 29(2):224–245, 1973.

[118] E. Ruckenstein and B. Pulvermacher. Kinetics of crystallite sintering during heat treatment of supported metal catalysts. *AIChE Journal*, 19(2):356–364, 1973.

[119] Marina Ruths and Jacob N. Israelachvili. *Surface Forces and Nanorheology of Molecularly Thin Films*, pages 417–515. Springer Berlin Heidelberg, Berlin, Heidelberg, 2008.

[120] Richard L. Schwoebel. Step motion on crystal surfaces. II. *Journal of Applied Physics*, 40(2):614–618, 1969.

[121] LE Scriven. Physics and applications of dip coating and spin coating. In *MRS proceedings*, volume 121, page 717. Cambridge Univ Press.

[122] FM Serry. Improving the accuracy of afm force measurements: The thermal tune solution to the cantilever spring constant problem. *Veeco Application Notes*, 14, 2005.

[123] N. Raveendran Shiju and Vadim V. Guliants. Recent developments in catalysis using nanostructured materials. *Applied Catalysis A: General*, 356(1):1–17, 2009.

[124] Daisuke Shindo and Tetsuo Oikawa. *Energy Dispersive X-ray Spectroscopy*, pages 81–102. Springer Japan, Tokyo, 2002.

[125] Soren B. Simonsen, Ib Chorkendorff, Soren Dahl, Magnus Skoglundh, Kristoffer Meinander, Thomas N. Jensen, Jeppe V. Lauritsen, and Stig Helveg. Effect of particle morphology on the ripening of supported pt nanoparticles. *The Journal of Physical Chemistry C*, 116(9):5646–5653, 2012.

[126] Soren B. Simonsen, Ib Chorkendorff, Soren Dahl, Magnus Skoglundh, Jens Sehested, and Stig Helveg. Direct observations of oxygen-induced platinum nanoparticle ripening studied by in situ TEM. *Journal of the American Chemical Society*, 132(23):7968–7975, 2010.

[127] Soren Bredmose Simonsen, Ib Chorkendorff, Soren Dahl, Magnus Skoglundh, Jens Sehested, and Stig Helveg. Ostwald ripening in a Pt/SiO2 model catalyst studied by in situ TEM. *Journal of Catalysis*, 281(1):147–155, 2011.

[128] Joachim P Spatz, Thomas Herzog, Stefan Moessmer, Paul Ziemann, and Martin Moeller. Micellar inorganic-polymer hybrid systems-a tool for nanolithography. *Advanced Materials*, 11(2):149–153, 1999.

[129] Joachim P Spatz and Sebastian Lechner. Substrate surface structured with thermally stable metal alloy nanoparticles, a method for preparing the same and uses thereof, in particular as a catalyst. 2014.

[130] Joachim P. Spatz, Stefan Moessmer, Christoph Hartmann, Martin Moeller, Thomas Herzog, Michael Krieger, Hans-Gerd Boyen, Paul Ziemann, and Bernd Kabius. Ordered deposition of inorganic clusters from micellar block copolymer films. *Langmuir*, 16(2):407–415, 2000.

[131] Joachim P Spatz, Stefan Moessmer, and Martin Moeller. Mineralization of gold nanoparticles in a block copolymer microemulsion. *Chemistry-A European Journal*, 2(12):1552–1555, 1996.

[132] Joachim P Spatz, Arno Roescher, and Martin Moeller. Gold nanoparticles in micellar poly (styrene)-b-poly (ethylene oxide) films-size and interparticle distance control in monoparticulate films. *Advanced Materials*, 8(4):337–340, 1996.

[133] Joachim P. Spatz, Sergei Sheiko, and Martin Moeller. Ion-stabilized block copolymer micelles film formation and intermicellar interaction. *Macromolecules*, 29(9):3220–3226, 1996.

[134] Kurt H Stern. *Metallurgical and ceramic protective coatings*. Springer Science and Business Media, 1996.

[135] Werner Stoeber, Arthur Fink, and Ernst Bohn. Controlled growth of monodisperse silica spheres in the micron size range. *Journal of Colloid and Interface Science*, 26(1):62–69, 1968.

[136] Joseph A. Stroscio, D. T. Pierce, M. D. Stiles, A. Zangwill, and L. M. Sander. Coarsening of unstable surface features during Fe(001) homoepitaxy. *Physical Review Letters*, 75(23):4246–4249, 1995.

[137] Pooya Tabib Zadeh Adibi, Torben Pingel, Eva Olsson, Henrik Groenbeck, and Christoph Langhammer. Plasmonic nanospectroscopy of platinum catalyst nanoparticle sintering in a mesoporous alumina support. *ACS Nano*, 10(5):5063–5069, 2016.

[138] Pooya Tabib Zadeh Adibi, Torben Pingel, Eva Olsson, Henrik Groenbeck, and Christoph Langhammer. Pt nanoparticle sintering and redispersion on a heterogeneous nanostructured support. *The Journal of Physical Chemistry C*, 120(27):14918–14925, 2016.

[139] Pooya Tabib Zadeh Adibi, Vladimir P. Zhdanov, Christoph Langhammer, and Henrik Groenbeck. Transient bimodal particle size distributions during Pt sintering on alumina and silica. *The Journal of Physical Chemistry C*, 119(2):989–996, 2015.

[140] Mieko Takagi. Electron-diffraction study of liquid-solid transition of thin metal films. *Journal of the Physical Society of Japan*, 9(3):359–363, 1954.

[141] S. J. Tauster. Strong metal-support interactions. *Accounts of Chemical Research*, 20(11):389–394, 1987.

[142] S. J. Tauster, S. C. Fung, and R. L. Garten. Strong metal-support interactions. group 8 noble metals supported on titanium dioxide. *Journal of the American Chemical Society*, 100(1):170–175, 1978.

[143] Andrea Thorenz and Armin Reller. Discussion of risks of platinum resources based on a function orientated criticality assessment - shown by cytostatic drugs and automotive catalytic converters. *Environmental Sciences Europe*, 23(1):1–12, 2011.

[144] Harland Tompkins and Eugene A Irene. *Handbook of ellipsometry*. William Andrew, 2005.

[145] Michael C Tringides. *Surface Diffusion: Atomistic and Collective Processes*, volume 360. Springer Science and Business Media, 2013.

[146] T. Tsirlin, J. Zhu, J. Grunes, and G. A. Somorjai. AFM and TEM studies of Pt nanoparticle arrays supported on alumina model catalyst prepared by electron beam lithography. *Topics in Catalysis*, 19(2):165–170, 2002.

[147] Tien T. Tsong. Mechanisms of surface diffusion. *Progress in Surface Science*, 67(1 - 8):235–248, 2001.

[148] J. A. Venables. Rate equation approaches to thin film nucleation kinetics. *Philosophical Magazine*, 27(3):697–738, 1973.

[149] John Venables. *Introduction to surface and thin film processes*. Cambridge University Press, 2000.

[150] John A. Venables. Atomic processes in crystal growth. *Surface Science*, 299:798–817, 1994.

[151] A. Venkateswara Rao and Sharad D. Bhagat. Synthesis and physical properties of teos-based silica aerogels prepared by two step (acid-base) sol-gel process. *Solid State Sciences*, 6(9):945–952, 2004.

[152] Carl Wagner. Theorie der Alterung von Niederschlaegen durch Umloesen (Ostwald-Reifung). *Zeitschrift fuer Elektrochemie, Berichte der Bunsengesellschaft fuer physikalische Chemie*, 65(7-8):581–591, 1961.

[153] Duhua Wang and Gordon P. Bierwagen. Sol-gel coatings on metals for corrosion protection. *Progress in Organic Coatings*, 64(4):327–338, 2009.

[154] J. A. Wang, X. Bokhimi, A. Morales, O. Novaro, T. Lopez, and R. Gomez. Aluminum local environment and defects in the crystalline structure of sol-gel alumina catalyst. *The Journal of Physical Chemistry B*, 103(2):299–303, 1999.

[155] Zhong Lin Wang. *Transmission Electron Microscopy and Spectroscopy of Nanoparticles*, pages 37–80. Wiley-VCH Verlag GmbH, 2001.

[156] Ian M Watt. *The principles and practice of electron microscopy*. Cambridge University Press, 1997.

[157] John F Watts and John Wolstenholme. An introduction to surface analysis by XPS and AES. *An Introduction to Surface Analysis by XPS and AES, by John F. Watts, John Wolstenholme, pp. 224. ISBN 0-470-84713-1. Wiley-VCH, May 2003.*, page 224, 2003.

[158] Kristina Wettergren, Florian F. Schweinberger, Davide Deiana, Claron J. Ridge, Andrew S. Crampton, Marian D. Roetzer, Thomas W. Hansen, Vladimir P. Zhdanov, Ueli Heiz, and Christoph Langhammer. High sintering resistance of size-selected platinum cluster catalysts by suppressed ostwald ripening. *Nano Letters*, 14(10):5803–5809, 2014.

[159] John A Woollam, Blaine D Johs, Craig M Herzinger, James N Hilfiker, Ron A Synowicki, and Corey L Bungay. Overview of variable-angle spectroscopic ellipsometry (vase): I. basic theory and typical applications. In *Optical Metrology*, pages 3–28.

[160] C. R. M. Wronski. The size dependence of the melting point of small particles of tin. *British Journal of Applied Physics*, 18(12):1731, 1967.

[161] Juwei Wu, Wei Liu, Xia Xiang, Kai Sun, Fenghua Liu, Chao Cai, Shaobo Han, Yongyong Xie, Sean Li, and Xiaotao Zu. From Ni(OH)2/Graphene composite to Ni@Graphene core-shell a self-catalyzed epitaxial growth and enhanced activity for nitrophenol reduction. *Carbon*, 117:192–200, 2017.

[162] Si-Han Wu, Chih-Ta Tseng, Yu-Shen Lin, Cheng-Han Lin, Yann Hung, and Chung-Yuan Mou. Catalytic nano-rattle of Au@ hollow silica: towards a poison-resistant nanocatalyst. *Journal of Materials Chemistry*, 21(3):789–794, 2011.

[163] P. Wynblatt. Particle growth in model supported metal catalysts-II. comparison of experiment with theory. *Acta Metallurgica*, 24(12):1175–1182, 1976.

[164] P. Wynblatt and N. A. Gjostein. Supported metal crystallites. *Progress in Solid State Chemistry*, 9:21–58, 1975.

[165] P. Wynblatt and N. A. Gjostein. Particle growth in model supported metal catalysts-I. theory. *Acta Metallurgica*, 24(12):1165–1174, 1976.

[166] Jung Whan Yoo, David Hathcock, and Mostafa A. El-Sayed. Characterization of Pt nanoparticles encapsulated in Al2O3 and their catalytic efficiency in propene hydrogenation. *The Journal of Physical Chemistry A*, 106(10):2049–2054, 2002.

[167] Hongjun You, Shengchun Yang, Bingjun Ding, and Hong Yang. Synthesis of colloidal metal and metal alloy nanoparticles for electrochemical energy applications. *Chemical Society Reviews*, 42(7):2880–2904, 2013.

[168] Thomas Young. Phil. *Trans Roy. Soc*, 95:65–75, 1805.

[169] Riyan Zahaf, Jae Wook Jung, Zachary Coker, Songkil Kim, Tae-Youl Choi, and Donggeun Lee. Pt catalyst over SiO2 and Al2O3 supports synthesized by aerosol method for HC-SCR DeNOx application. *Aerosol and Air Quality Research*, 15(6S):2409–2421, 2015.

[170] Ulrich Zerweck, Christian Loppacher, Tobias Otto, Stefan Grafstroem, and Lukas M. Eng. Accuracy and resolution limits of kelvin probe force microscopy. *Physical Review B*, 71(12):125424, 2005.

[171] Zhi-cheng Zhang, Biao Xu, and Xun Wang. Engineering nanointerfaces for nanocatalysis. *Chemical Society Reviews*, 43(22):7870–7886, 2014.

[172] Martin Zinke-Allmang, Leonard C. Feldman, and Marcia H. Grabow. Clustering on surfaces. *Surface Science Reports*, 16(8):377–463, 1992.

Abbreviations and Symbols

Abbreviations

4-AP	p-Aminophenol
4-NP	p-Nitrophenol
4-NPI	4-Nitrophenolate ion
AFM	Atomic force microscopy
Al_2O_3	Alumina
AM-KPFM	Amplitude modulation KPFM
ASB	Aluminum-tri-sec-butoxide
BCML	Block copolymer micellar lithography
BE	Backscattered electrons
CMC	Critical micelle concentration
CO	Carbon monoxide
CPD	Contact potential difference
E_F	Fermi energy level
E_V	Vacuum energy level
EAA	Ethylacetoacetate
EDX	Energy dispersive X-ray spectroscopy
ES barrier	Ehrlich-Schwoebel barrier
ESB	Energy selective backscattered mode at the SEM
FM-KPFM	Frequency modulation KPFM
HC	Hydrocarbon
ICP-OES	Inductively coupled plasma-optical emission spectroscopy
IPA	Isopropanol
KPFM	Kelvin probe force microscopy
LFM	Lateral force microscopy
LSW theory	Theory from Lifshitz, Slyozov and Wagner
$NaBH_4$	sodium borohydride
NO_x	Nitrogen oxide
NP	Nanoparticle
OR	Ostwald ripening
P2VP	Poly-2-vinylpyridine
PMC	Particle migration and coalescence
PS	Polystyrene
PSD	Particle size distribution
Pt NP	Platinum nanoparticle
rpm	Rounds per minute
SE	Secondary electrons
SEM	Scanning electron microscopy
SiO_2	Silica
SMSI	Strong metal-support interaction
TEM	Transmission electron microscopy
TEOS	Tetraethyl orthosilicate
UV-Vis	Ultraviolet-visible spectroscopy
W10	Hydrogen/argon gas mixture
XPS	X-ray photoelectron spectroscopy

Symbols

α	Deflection sensitivity of AFM cantilever
β	Adatom vibration frequency for OR sinter model
β'	Adatom jump frequency for OR sinter model
Δ	Ellipsometric parameter Delta
ΔE_{ES}	Ehrlich-Schwoebel energy barrier

ΔV ..... Potential difference
Φ ..... Work function
Φ_{sample} ..... Work function of AFM sample
Φ_{tip} ..... Work function of AFM tip
γ ..... Surface energy
γ^* ..... Interfacial energy between material A and B
γ_{LV} ..... Liquid-vapor surface tension
γ_{SL} ..... Solid-liquid interfacial tension
γ_{SV} ..... Surface energy of solid in vapor
η ..... Viscosity
ϑ ..... Contact angle
λ ..... Wavelength
ρ ..... Complex ratio of reflection coefficients in ellipsometry
τ_a ..... Adsorption residence time of adatoms on substrate
υ_a ..... Atomic vibration frequency
υ_d ..... Diffusion frequency
υ_p ..... Adatom vibration frequency on particle
υ_s ..... Adatom vibration frequency on support
Ω ..... Atomic volume of NP
ω ..... Frequency
Ψ ..... Ellipsometric parameter Psi
a ..... Jump distance
A_d ..... Rate constant for diffusion-limited OR sinter growth law
A_v ..... Rate constant for vapor phase transport of platinum oxide in OR sinter growth law
A/B/C_k ..... Fitting parameters in Cauchy equation for extinction coefficient in ellipsometry
A/B/$C_{n.}$ ..... Fitting parameters in Cauchy equation for optical constant index in ellipsometry
C ..... Capacitance
c ..... Concentration
c'_s ..... Adatom concentration on substrate right next to particle for OR sinter model
c_p ..... Adatom concentration on particle for OR sinter model
c_s ..... Adatom concentration on substrate for OR sinter model
D ..... Diffusion coefficient
d ..... Diameter
d_0 ..... Initial diameter
D_1 ..... Adatom diffusion coefficient for OR sinter model
d_a ..... Atomic diameter
D_p ..... Particle diffusion coefficient
D_{s0} ..... Frequency factor for PMC sinter model
D_s ..... Surface self-diffusion coefficient
e ..... Elementary charge
E_{act} ..... Activation energy for PMC sinter model
$E_{ad,m}$ ..... Sublimation energy of bulk metal for OR sinter model
$E_{ad,s}$ ..... Sublimation energy of support for OR sinter model
E_a ..... Adsorption energy
E_b ..... Binding energy
E_d ..... Diffusion energy
E_k ..... Kinetic energy
F ..... Force
F_{el} ..... Electrostatic force
F_N ..... Normal force
H ..... Standard free energy
H_{ps} ..... Free energy difference of adatom on particle and on substrate for OR sinter model
H_{sm} ..... Free migration energy of adatom on substrate for OR sinter model
$h\upsilon$ ..... Energy of X-rays
I ..... Intensity

K ..... Constant for general sintering growth law
k ..... Boltzmann constant
k_{ext} ..... Extinction coefficient
$K_{ij/ik}$ ..... Coefficient for PMC sinter model
k_{LFM} ..... Spring constant of AFM cantilever
L ..... Loading ratio of micelles
l ..... Distance for OR sinter model
M ..... Molar mass
m ..... Mass
M_n ..... Number average molar mass of polymer
n ..... Optical constant index
$n_1(t)$ ..... Areal density of adatoms as a function of time during nucleation
n_k ..... Number of NPs per unit support area for PMC sinter model
p ..... Pressure
q ..... Integer in general sinter growth law
R ..... Rate of atoms at arrival on surface during nucleation
r^* ..... Critical radius for OR sinter model
r_H ..... Hydrodynamic radius
r_p ..... Fresnel reflection coefficient for p-polarized light
r_s ..... Fresnel reflection coefficient for s-polarized light
s ..... Interatomic spacing for OR sinter model
T ..... Temperature
t ..... Time
$T_{Tammann}$ ..... Tammann temperature
Units VP ..... Units of vinylpyridine monomer
V ..... deflection of cantilever
V_{AC} ..... AC voltage
V_{CPD} ..... CPD voltage
V_{DC} ..... DC voltage
x ..... Migration length of adatom
z ..... Distance in capacitor

List of Figures

List of Tables

Appendix

A Adhesion of platinum nanoparticles on further substrates

Further AFM images of the NP adhesion study with LFM can be seen in the supplementary Figure A.1.

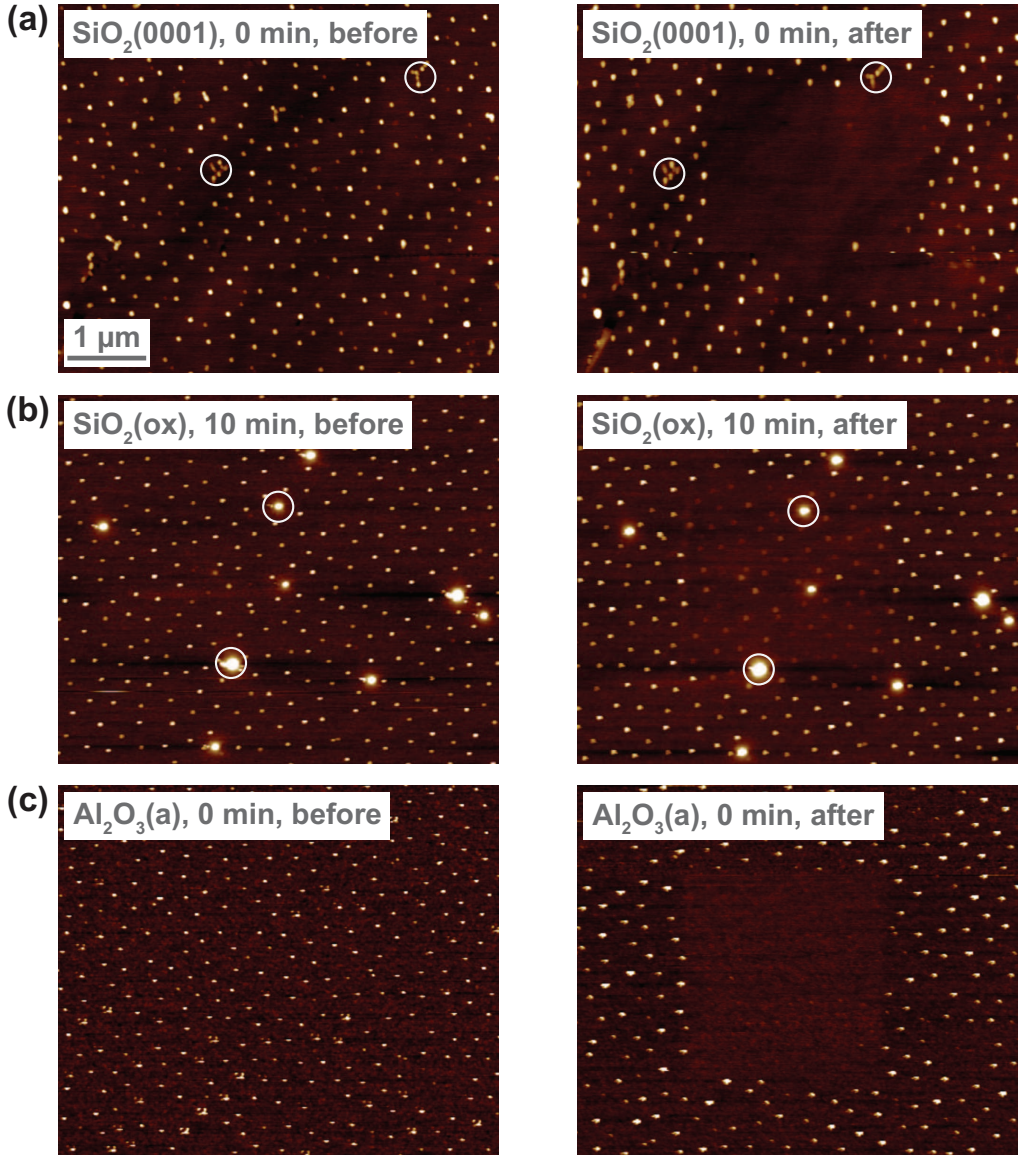

Figure A.1: AFM images of NPs on (a) crystalline $SiO_2(0001)$ without heat treatment, on (b) thermally oxidized amorphous $SiO_2(ox)$ after 10 min at 750°C and on (c) amorphous $Al_2O_3(a)$ without heat treatment, each measured with reduced F_N (before) and after applying a higher F_N (after) to remove the NPs.

Though all small NPs could be scraped off of the SiO_2(ox)-sample surface, some larger sintered particles that had formed during the 10 min oven treatment could not be removed with the AFM.

B Control sinter study on dual-structured substrates

Supplementary Figure B.1 shows control samples for observing the sintering behavior of Pt NPs on dual-structured surfaces.

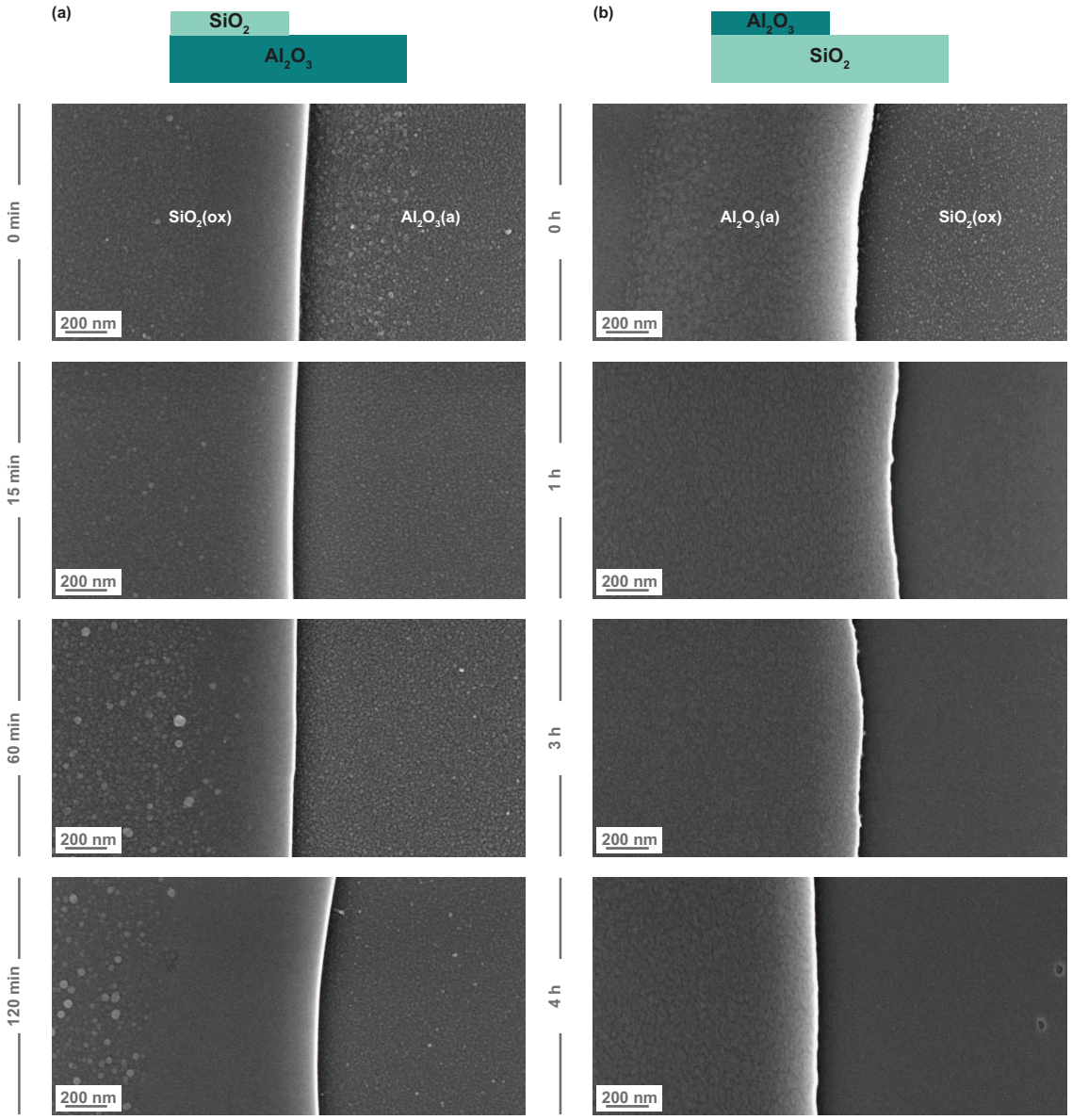

Figure B.1: Control samples of dual-structured substrates composed of a silica- and an alumina-side without Pt NPs during heat treatment at 750°C (compare with Figure 4.12). No interfering phenomena which could alter the sintering behavior of Pt NPs on these supports could be detected.

For these samples, amorphous silica-alumina-substrates were fabricated, as described in Figure 2.12 without depositing Pt NPs onto them. Afterwards, they underwent the same heat treatment at 750°C as the surfaces in Figure 4.12. These references exhibit no morphological changes that could interfere with the sintering behavior of Pt NPs on the supports, neither for the dual-structured surfaces with amorphous silica on alumina (Figure B.1a) nor with amorphous alumina on silica (Figure B.1b). During a sinter study over the time period of 120 min in the first case and 4 h in the second case, no migrating bright spots and no platinum could be detected anywhere. Additionally, both the diffusion of aluminum ions into silica, as well as the diffusion of silicon ions into alumina could be ruled out by EDX measurements.

C Cross sections of isolating silica and alumina layers

TEM cross sections of annealed alumina samples with immobilized Pt NPs and a separating SiO_2- or Al_2O_3-layer at 750°C for 2 h are displayed in Figure C.1 and Figure C.2 respectively. In both cases, the Pt NPs are detected as dark spots without an increase in nanoparticle size on the amorphous alumina-substrate during the heat treatment. Additionally, the thin layers composed of colloidal silica particles (Figure C.1a and b) and colloidal alumina particles (Figure C.2a and b) appear as a lighter band on the alumina and around the nanoparticles without showing coverage of these ones. So, it can be concluded that neither the silica nor the alumina layer changes significantly in height during the sinter process, thus leaving the nanoparticles uncovered and hence the catalytically active sites free.

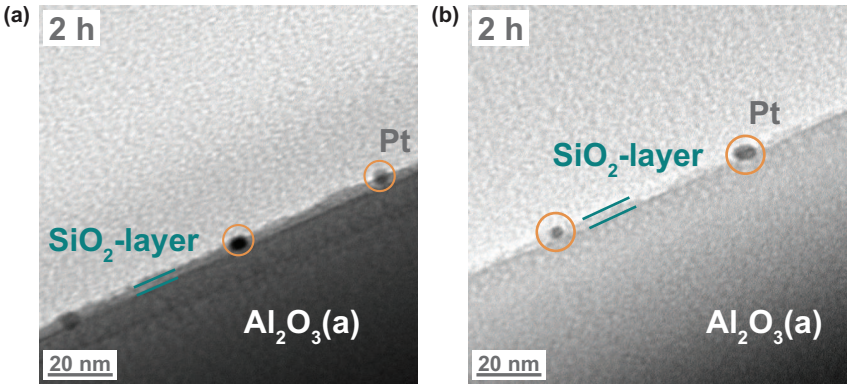

Figure C.1: (a) and (b) Cross sections of isolated Pt NPs with a silica layer after a 2 h-heat treatment at 750°C in TEM.

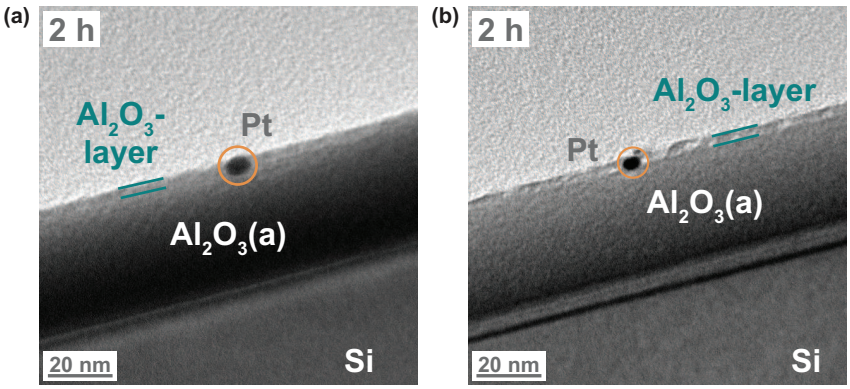

Figure C.2: (a) and (b) Cross sections of isolated Pt NPs with an alumina layer after a 2 h-heat treatment at 750°C in TEM.

D Catalytic activity of isolated platinum nanoparticles

The catalytic activity of platinum nanoparticles can be tested by the hydrogenation of methyl red as a model reaction [43]. In the presence of hydrogen, Pt NPs break the $N = N$ bond of methyl red, as it can be seen in Figure D.1. Hereby, a loss of the initial red color is triggered, which can be monitored by UV-vis spectroscopy.

The goal of these experiments was to analyze the catalytic activity of platinum nanoparticles with isolating silica and alumina layers from chapter 6. When testing the Pt NPs without layers surrounding them, the resulting absorption spectra are shown in Figure D.2a. As references, a silicon-wafer (light green curve), one with a 100 nm amorphous alumina layer, Al_2O_3(a), and exposed to hydrogen (dark green curve), as well as a silicon wafer plus alumina layer with Pt NPs (light orange curve) were used. In these cases, the absorption spectra revealed no color change of the methyl red solution and therefore, no catalytic activity was indicated. Afterwards, the methyl red solution was bubbled with hydrogen in the presence of Pt NPs on amorphous alumina (dark orange curve). Yet, no differences in absorption through the conversion of methyl red could be detected either. ICP-OES measurements revealed a very low platinum loading on the samples which attributes to the unaltered UV-vis spectra for methyl red. Following, the absorption spectra of methyl red with a sample of tenfold Pt NPs amount was monitored by UV-vis (Figure D.2b). Here, a slight drop in absorbance was observed for the sample with platinum particles compared to a reference sample without the particles (Si-wafer curve). However, this decrease cannot be taken as a significant reduction caused by the conversion of the azo dye since it could also be triggered by interfering environmental influences and measurement inaccurancies. Thus, the catalytic activity of isolated Pt NPs could not be tested with this described method.

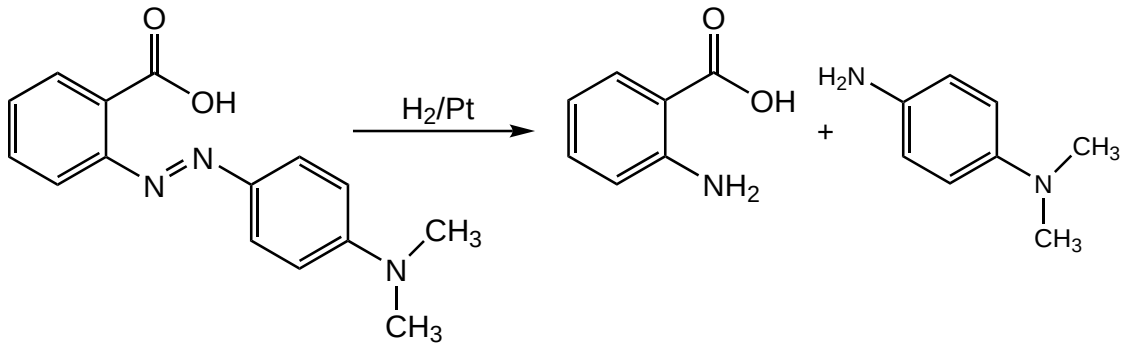

Figure D.1: Hydrogenation of methyl red as a model reaction to test the catalytic activity of Pt NPs [43].

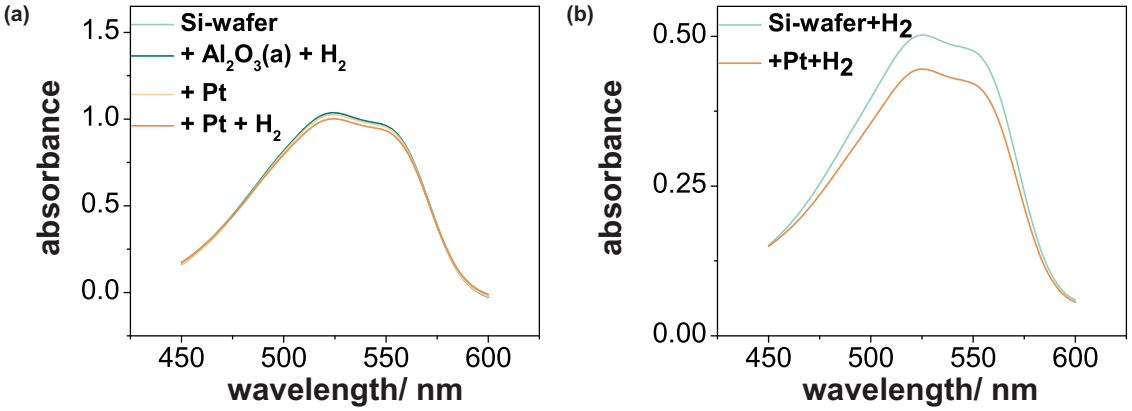

Figure D.2: UV-vis spectra of methyl red solution (a) on a silicon wafer (Si-wafer/ light green curve) plus the 100 nm amorphous alumina-layer (+ Al_2O_3(a)/ dark green curve)) plus 1x spin coated Pt NPs (+ Pt/ light orange curve) as references before hydrogenation reaction. Additionally, the spectrum of Pt NPs with H_2 (+ Pt + H_2/ dark orange curve) is graphed after the unsuccessful hydrogenation reaction of methyl red. Then (b), the amount of Pt NPs was increased ten-fold and the resulting UV-vis spectra of methyl red on Si-wafer with H_2 (light green curve) as a reference and Pt NPs with H_2 (dark orange curve) are displayed.

Afterwards, another model reaction, the conversion of the yellow *p*-nitrophenol (4-NP) to the colorless *p*-aminophenol (4-AP) by sodium borohydride $NaBH_4$ via the intermediate 4-nitrophenolate ion (4-NPI) (Figure D.3a) was analyzed for determining the catalytic activity of Pt NPs [161]. The absorbance spectra for a reference sample of Si-wafer and for one with a tenfold concentration of Pt NPs (+ Pt) were recorded and are presented in Figure D.3b. Again, no color change was detected and therefore, no 4-NP was successfully transformed to 4-AP. This is also caused by the limited concentration of platinum on the samples.

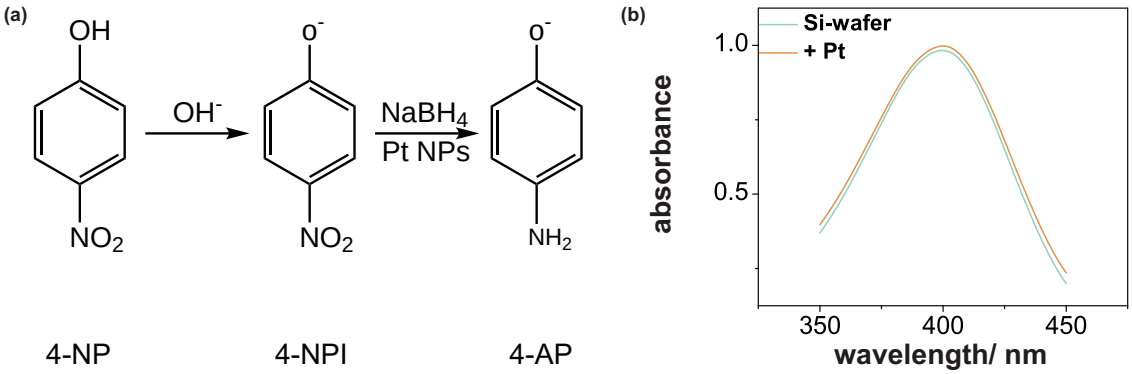

Figure D.3: (a) Conversion from p-nitrophenol (4-NP) to p-aminophenol (4-AP) as a model reaction to test the catalytic activity of Pt NPs [161]. (b) UV-vis spectra of 4-NP solution before (Si-wafer/ light green curve) and after conversion reaction with Pt NPs (+ Pt/ dark green curve).

Summarizing, the catalytic activity of isolated Pt NPs could not be proven by these two model reactions involving methyl red and *p*-nitrophenol due to a very small platinum concentration.

Eidesstattliche Versicherung gemäß § 8 der Promotionsordnung der Naturwissenschaftlich-Mathematischen Gesamtfakultät der Universität Heidelberg

1. Bei der eingereichten Dissertation zu dem Thema

_____

_____

_____

handelt es sich um meine eigenständig erbrachte Leistung.

2. Ich habe nur die angegebenen Quellen und Hilfsmittel benutzt und mich keiner unzulässigen Hilfe Dritter bedient. Insbesondere habe ich wörtlich oder sinngemäß aus anderen Werken übernommene Inhalte als solche kenntlich gemacht.

3. Die Arbeit oder Teile davon habe ich wie folgt/bislang nicht[1)] an einer Hochschule des In- oder Auslands als Bestandteil einer Prüfungs- oder Qualifikationsleistung vorgelegt.

Titel der Arbeit:_____

_____

Hochschule und Jahr:_____

Art der Prüfungs- oder Qualifikationsleistung:_____

4. Die Richtigkeit der vorstehenden Erklärungen bestätige ich.

5. Die Bedeutung der eidesstattlichen Versicherung und die strafrechtlichen Folgen einer unrichtigen oder unvollständigen eidesstattlichen Versicherung sind mir bekannt.

Ich versichere an Eides statt, dass ich nach bestem Wissen die reine Wahrheit erklärt und nichts verschwiegen habe.

_____ _____

Ort und Datum Unterschrift

[1)] Nicht Zutreffendes streichen. Bei Bejahung sind anzugeben: der Titel der andernorts vorgelegten Arbeit, die Hochschule, das Jahr der Vorlage und die Art der Prüfungs- oder Qualifikationsleistung.